Nuclear speckle rejuvenation alleviates proteinopathies at the expense of YAP1.

William Dion[1, #], Yuren Tao[2, #], Maci Chambers[1], Shanshan Zhao[2], Riley K. Arbuckle[3,4], Michelle Sun[1], Syeda Kubra[1], Yuhang Nie[2], Megan Ye[1], Mads B. Larsen[1], Daniel Camarco[1], Eleanor Ickes[1], Claire DuPont[1], Haokun Wang[1], Bingjie Wang[3], Silvia Liu[5,6], Shaohua Pi[3], Bill B Chen[1,7], Yuanyuan Chen [3,8] *, Xu Chen[2] *, and Bokai Zhu[1,5,9] *

[1] Aging Institute of UPMC, University of Pittsburgh School of Medicine, Pittsburgh, PA, U.S.A.
[2] Department of Neuroscience, School of Medicine, University of California, San Diego, CA, U.S.A.
[3] Department of Ophthalmology, University of Pittsburgh School of Medicine, PA, U.S.A.
[4] Department of Human Genetics, University of Pittsburgh Graduate School of Public Health, Pittsburgh, PA, USA.
[5] Pittsburgh Liver Research Center, University of Pittsburgh, Pittsburgh, PA, U.S.A.
[6] Department of Pathology, University of Pittsburgh School of Medicine, Pittsburgh, PA, U.S.A.
[7] Division of Pulmonary, Allergy and Critical Care Medicine, Department of Medicine, University of Pittsburgh School of Medicine, Pittsburgh, PA, U.S.A.
[8] Department of Pharmacology and Chemical Biology, University of Pittsburgh School of Medicine, PA, U.S.A.
[9] Division of Endocrinology and Metabolism, Department of Medicine, University of Pittsburgh School of Medicine, Pittsburgh, PA, U.S.A.

# These authors contribute equally.

Corresponding authors*:

Yuanyuan Chen: cheny1@pitt.edu

Xu Chen: x1chen@health.ucsd.edu

Bokai Zhu: bzhu@pitt.edu

Abstract

Current treatments targeting individual protein quality control have limited efficacy in alleviating proteinopathies, highlighting the prerequisite for a common upstream druggable target capable of global proteostasis modulation. Building on our prior research establishing nuclear speckles as pivotal organelles responsible for global proteostasis transcriptional control, we aim to alleviate proteinopathies through nuclear speckle rejuvenation. We identified pyrvinium pamoate as a small-molecule nuclear speckle rejuvenator that enhances protein quality control while suppressing YAP1 signaling via decreasing the surface tension of nuclear speckle condensates through interaction with the intrinsically disordered region of nuclear speckle scaffold protein SON. In pre-clinical models, pyrvinium pamoate reduced tauopathy and alleviated retina degeneration by promoting autophagy and ubiquitin-proteasome system. Aberrant nuclear speckle morphology, reduced protein quality control and increased YAP1 activity were also observed in human tauopathies. Our study uncovers novel therapeutic targets for tackling protein misfolding disorders within an expanded proteostasis framework encompassing nuclear speckles and YAP1.

Introduction:

Proteinopathies are diseases associated with the accumulation of misfolded proteins, which often arise from a decline in proteostasis pathways, including the ubiquitin-proteasome system (UPS), the ER-Golgi protein secretory pathways, and autophagy lysosomal pathway (ALP) [1,2]. However, therapies targeting singular pathways have limited efficacy, indicating an incomplete understanding of disease mechanisms.

We recently discovered that under physiological conditions, the network of proteostasis pathways manifests as cell-autonomous 12-hour (12h) ultradian rhythms, regulated by a dedicated 12h oscillator, independent from the 24h circadian clock and the cell cycle [3-13]. By studying this 12h oscillator, we uncovered an unexpected role of nuclear speckles in global proteostasis control [9]. Nuclear speckles are membrane-less organelles important for mRNA processing and gene regulation[14-18], and their liquid-liquid phase separation (LLPS) dynamics dictate the global transcriptional capacity of proteostasis genes [9]. Moderate overexpression of the nuclear speckle scaffolding protein SON is sufficient to decrease nuclear speckle sphericity, increase the recruitment of nuclear speckles to chromatin, amplify proteostasis gene expression, and reduce protein aggregation [9]. Conversely, reducing SON level leads to much more spherical and stagnant speckles, sequesters nuclear speckles away from chromatin, blunts proteostasis gene expression and subsequently elevates intracellular protein aggregates [19]. Since SON expression decreases with age in various tissues in mice, in human lung, and in brain tissues of human subjects with Alzheimer's disease (**Extended Data Fig 1a-g**) [9,20], we hypothesize that genetically or pharmacologically boosting SON expression and/or function (a term we herein coin as “nuclear speckles rejuvenation”) could augment the entire proteostasis network and thus potentially delay or even reverse the progression of both aging-related and inherited proteinopathies.

In this study, we initially characterized the comprehensive transcriptome changes resulting from SON-mediated nuclear speckle rejuvenation and unexpectedly discovered a broader proteostasis framework that incorporates SON-mediated nuclear speckles LLPS enhancement, unfolded protein response (UPR) transcription factors (TF)-mediated proteostasis gene activation and YAP1-mediated transcriptional repression. Via a high-throughput drug screen, we identified pyrvinium pamoate (PP) as a small molecule nuclear speckle rejuvenator that recapitulates the entire transcriptome changes elicited by SON overexpression. Mechanistically, via a cell-free

nuclear speckle reconstitution system, we demonstrated that PP exerts transcriptional reprogramming via reducing the surface/interfacial tension of nuclear speckle condensates and promoting their wetting of genomic DNA via targeting the intrinsically disordered domain (IRD) of SON. In preclinical models, PP exhibited strong efficacy in protecting against both tauopathy and retinal degeneration at nanomolar concentration. We further demonstrated that the previously known anti-YAP/WNT activity of PP [21-23] could be explained by the expanded proteostasis framework and is also required for its ability to ameliorate proteinopathies. Lastly, we showed that both the reduction of proteostasis gene expression and increase of YAP1 transcriptional activity is associated with retinal degeneration in mice and tauopathy in humans.

Result:

Genetic rejuvenation of nuclear speckle transcriptionally reprograms global proteostasis and YAP1 activity in an opposing manner.

To determine the extent by which SON transcriptionally reprograms gene expression under both basal and proteotoxic stress conditions, we performed bulk mRNA-Seq on immortalized mouse embryonic fibroblasts (MEFs) with either SON knockdown (KD) by siRNA or overexpression (OE) via CRISPRa[24], in the absence or presence of the ER stress inducer tunicamycin (Tu) as previously described (**Extended Data Table1**) [9]. Principal component analysis (PCA) on total mRNA level indicated that while SON manipulation has little effects on global gene expression under basal condition, SON OE and KD significantly amplified and dampened the global transcriptional response to ER stress, respectively (**Fig. 1a**). These include 461 genes that are normally induced, and 901 genes repressed by Tu under normal SON expression condition (**Fig. 1b-c, Extended Data Fig. 2a**). For both groups of genes, we further observed a strong correlation between the relative fold induction or repression for each gene under SON OE and KD conditions (**Extended Data Fig. 2b**), further demonstrating the robustness of bidirectional control on proteostasis gene expression by SON.

As expected, gene ontology (GO) analysis revealed that those ER stress-induced 461 genes are strongly enriched in protein quality control pathways, including protein folding (such as *Pdia3*, *Dnajb11* and *Manf*), ER/Golgi quality control (such as *Sec23b*, *Hyou1* and *Hspa5*), tRNA aminoacylation (such as *Gars*, *Iars* and *Eprs*), ER-associated protein degradation (ERAD) (such as *Edem1*, *Syvn1*, *Sel1l* and *Ube2g2*), and autophagy (such as *Sqstm1* and *Atg13*) (**Extended Data Fig. 2a**). To shed light on the mechanisms by which SON transcriptionally amplifies gene activation in response to ER stress, we performed both Landscape In Silico deletion Analysis (LISA) [25] and motif analysis to infer the transcriptional regulators that may recruit nuclear speckles to chromatin. Both analyses revealed basic leucine zipper (bZIP) transcription factors (TFs), including ATF6, XBP1, ATF4 and CREB1 as the top candidates (**Fig. 1e and Extended Data Fig. 2c**). ChIP-qPCR further showed increased recruitment of nuclear speckles to the 3' regions of selective proteostasis genes in response to SON OE under both basal and ER stress conditions, concomitant with increased XBP1s recruitment to the promoter regions of the same genes (**Extended Data Fig. 2d, e**). To corroborate our *in vitro* findings, we further examined a recently published murine *in vivo* hepatic XBP1s interactome dataset [10], and found proteins involved in mRNA splicing and processing are very strongly enriched in the XBP1s interactome at CT8, a time when hepatic SON expression peaks [9], with PRPF8, SNRNP200 and DHX9 being the top three most abundant proteins detected in the entire XBP1s interactome at CT8 (**Fig. 1f, g**). By contrast, at CT0 when SON expression is the lowest, the amount of splicing proteins that XBP1s interacts with is markedly reduced (**Fig. 1g**). The observed decreased recruitment of splicing

proteins to XBP1s at CT0 is not due to reduced XBP1s level itself, as the hepatic XBP1s expression at CT0 is in fact higher compared to CT8 [3,26]. These results thus reinforce the notion that nuclear speckles rejuvenation by SON OE is sufficient to amplify the global proteostasis transcriptional activation, likely via facilitating physical interactions between nuclear speckles and UPR TF like XBP1s.

Compared to induced genes, much less is known about the gene programs that are repressed under ER stress. GO analysis indicate that those 901 repressed genes are strongly enriched in Hippo-YAP1 signaling that regulates the diverse biological processes of angiogenesis, axon guidance, epithelial to mesenchymal transition (EMT), wound healing, cell adhesion, cell migration, and extra cellular matrix organization, with examples of canonical YAP1 target genes *Bmp4*, *Tuba1a*, *Fzd2*, *Tgfb3* and *Yap1* itself and its transcriptional partner *Tead2* [27-29] (**Fig. 1b-d and Extended Data Fig. 2a**). YAP1 and TEAD2 were further predicted to be transcriptional regulators of these 901 genes via both LISA and motif analysis (**Fig. 1h and Extended Data Fig. 2c**) and nuclear YAP1 level was significantly reduced in response to either Tu or SON OE and further decreased upon the combination of the two (**Fig. 1i, j**). Scratch assays further confirmed that both SON OE and Tu significantly reduced cell migration in MEFs, with the lowest observed in SON OE cells under ER stress (**Fig. 1k, l**). To rule out the possibility that the global repression of YAP1 transcriptional output during ER stress is specific to MEFs or Tu, we further analyzed a recent transcriptome dataset in the human astrocytoma-derived LN-308 cell line in response to both Tu and thapsigargin (Thap) (another ER stress inducer) treatments [30], and observed a strong downregulation of genes involved in YAP1 signaling under both treatments that progressed with time (**Extended Data Fig. 3a-c**). Together, our data indicates that the downregulation of YAP1 transcriptional output is an integral component of the global transcriptional response to proteotoxic stress, and it is also under nuclear speckles control.

Given the established roles of nuclear speckles in mRNA processing [31-33], we next investigated whether SON also regulates mRNA splicing dynamics. While SON manipulation has no effects on the overall transcriptional state of mature mRNA under basal DMSO condition (**Extended Data Fig. 4a bottom**) (consistent with total mRNA shown in **Fig. 1a**), it exerted profound effects on the pre-mRNA level (**Extended Data Fig. 4a top**), indicating a change in splicing dynamics. By either estimating the relative splicing rates among different groups under basal condition using a simple first-order kinetic model of transcription (see Materials and Methods) or quantifying global intron retention events using the iRead algorithm [34], we found that SON increases the splicing rates and improves the splicing fidelity of genes involved in proteostasis and RNA metabolism, and negatively regulates those involved in YAP1-related processes of cell migration, axon guidance, cell adhesion and EMT (**Extended Data Figs. 4b-e, 5a-d and 6a-d**). The significant enrichment in mRNA processing genes themselves under SON control is consistent with known potent autoregulation of splicing factors [35,36]. Furthermore, we also found that SON can activate and repress the mature mRNA expression of a select set of proteostasis (albeit very modestly) and YAP1 target genes, respectively, under basal DMSO conditions (**Extended Data Fig. 7a-c**). Finally, we observed that SON can also activate an anti-viral response gene signature under basal DMSO condition (**Extended Data Fig. 7b**), suggesting a potential broader implication of nuclear speckle rejuvenation in boosting innate immunity. Collectively, our results demonstrated that genetically rejuvenating nuclear speckles reprograms global proteostasis and YAP1 transcriptional output in an opposing manner, under both basal and proteotoxic stress conditions *in vitro*.

An expanded proteostasis framework includes nuclear speckle and YAP1.

To further confirm that the opposing dynamics of proteostasis gene expression and YAP1 transcriptional output also occur *in vivo*, we examined their temporal gene expression rhythms in mouse liver. In addition to proteostasis genes, which exhibit prevalent ~12h ultradian rhythms of expression as previously reported [3,6,9], we further identified fifty-three hepatic ~12h-cycling genes involved in Hippo-YAP1 signaling, including *Yap1*, *Bmp4*, *Axin2*, and *Fzd6/7/8* (**Extended Data Fig. 8a-c**). More importantly, while proteostasis genes (including XBP1s itself) peak almost exclusively at CT2 and CT14, many Hippo-YAP1 controlled genes, including nuclear YAP1 level itself, exhibit opposite phases peaking around CT6 and CT18 (**Extended Data Fig. 8d, e**). The anti-phase relationship between proteostasis and YAP1 target genes under physiological condition *in vivo* is in line with their opposing transcriptional responses to acute ER stress *in vitro*.

Our results thus far demonstrated a tripartite network where nuclear speckle rejuvenation by SON boosts proteostasis and suppresses YAP1. Two possible topologies of the network exist. In model one, nuclear speckles can signal both proteostasis and YAP1 signaling directly (**Extended Data Fig. 9a, model 1**), while in model 2, nuclear speckles repress YAP1 downstream of increased proteostasis gene program (**Extended Data Fig. 9a, model 2**). To distinguish between the two models, we examined a recently published RNA-seq dataset in HEK293T cells treated with DMSO, Thap or a very specific XBP1s small molecule activator IXA4 [37-39]. While IXA4 can induce a robust proteostasis gene signature similar to that of Thap, it failed to repress YAP1 transcriptional output genes as Thap did (**Extended Data Fig. 9b-d**). Collectively these results support the first model where nuclear speckles can program proteostasis gene expression and YAP1 transcriptional output in parallel, likely via promoting physical interaction between nuclear speckles and XBP1s for the former, and triggering YAP1 nuclear exclusion for the latter (**Extended Data Fig. 9e**). We speculate the opposing changes in proteostasis and YAP1 signaling may reflect an energetic trade-off between proteostasis and the control of cell dynamics, which could be essential for maintaining cellular functions in the presence of a fluctuating environment (**Extended Data Fig. 9f, g**).

High-throughput screen (HTS) identified pyrvinium pamoate (PP) as a small-molecule rejuvenator of the nuclear speckle.

Having established the proof-of-principle of nuclear rejuvenation via SON OE, we next explore the feasibility of rejuvenating nuclear speckles pharmacologically, for two reasons. First, compared to the challenging implementation of SON-based gene therapy, which faces obstacles due to the considerable size (~7kb) of SON's open reading frame, using small molecules to boost nuclear speckle activity may offer superior therapeutic potential. Secondly, we wanted to utilize an orthogonal approach to further demonstrate the opposing transcriptional changes of proteostasis and YAP1 signaling following nuclear speckle rejuvenation. Since SON OE and KD reduced and increased the sphericity of nuclear speckles [19], respectively, putative nuclear speckle rejuvenators are expected to reduce the sphericity (and increase the diffuseness or irregularity) of speckles.

We started with a library of over 2500 FDA-approved drugs and ran a primary HTS on our previously described EGFP::SC35 (SRSF2) MEFs (EGFP was knocked in to the N-terminus of endogenous *Srsf2* locus, which is a well-established marker for nuclear speckles [9]) to identify compounds that could alter nuclear speckles sphericity (**Fig. 2a**). As a quality control, our primary screen successfully identified four histone deacetylase inhibitors that produced much more spherical nuclear speckles approaching and/or exceeding r=0.9 (**Extended Data Fig. 10a, b**), in alignment with a previous study [40]. In the end, we identified five compounds - the tyrosine kinase

225 inhibitors nintedanib (NB) and ponatinib (PB), the anti-microbial proflavine hemisulfate (PH) and
226 proflavine, and the anthelmintic pyrvinium pamoate (PP) – having the ability to both decrease
227 nuclear speckles sphericity and amplify *Perk*-promoter driven dGFP expression (*Perk* is a UPR
228 target and exhibits 12h rhythms of expression [3]) in a dose-dependent manner (**Fig. 2b, and**
229 **Extended Data Fig. 10c-e**). For PP, the reduced sphericity (more irregularity) is also further
230 associated with increased perimeter of nuclear speckles (**Fig. 2c**), suggestive of a large surface
231 area of nuclear speckles in the 3D space of the nucleus.

232 To determine which of these drugs are *bona fide* nuclear rejuvenators, we performed mRNA-
233 Seq on MEFs treated with NB, PB, PH or PP for 24 hours and compared the transcriptome
234 signature of each drug (**Extended Data Fig. 11a,** and **Extended Data Table2**) with those of SON
235 OE and KD under both DMSO and Tu conditions. Gene set enrichment analysis (GSEA) [41] using
236 either those 461 Tu-induced or 901 Tu-repressed genes (depicted in **Fig. 1c**) revealed PP as the
237 only drug triggering a transcriptional response with strong resemblance to SON OE cells in
238 response to ER stress (**Fig. 2d-e and Extended Data Fig. 11b**). These included both upregulated
239 genes implicated in protein quality control and downregulated genes involved in the regulation of
240 cell dynamics (**Fig. 2f, g and Extended Data Fig. 11c, d**). LISA analysis on differentially
241 expressed genes by PP revealed bZIP TFs ATF4 and YAP1 among top transcriptional regulators
242 of upregulated and downregulated genes, respectively (**Extended Data Fig. 11e**). PP increased
243 the expression of UPR and integrated stress response (ISR) TFs – XBP1s and ATF4 - at both the
244 mRNA and protein level (**Extended Data Fig. 11f, g)** and induced nuclear exclusion of YAP1
245 (**Extended Data Fig. 11h)**, while not affecting SON level (**Extended Data Fig. 11i**).

246 Our analysis so far suggested the PP induced a transcriptional signature that resembles a
247 mixture of responding to SON OE and Tu treatment. We performed additional comparative
248 transcriptome analysis to further validate this conclusion. First, when comparing the fold induction
249 or repression of gene expression by PP and Tu, the signature of PP is more similar to that of Tu
250 under SON OE compared to under SON KD condition (p= 0.00195 by Chow tests) (**Extended**
251 **Data Fig. 12a**). Secondly, similar to SON OE (**Extended Data Fig. 7b**), PP also induced
252 expression of genes involved in anti-viral response (**Extended Data Fig. 12b-f**), distinct from
253 those induced under ER stress. Thirdly, GSEA indicated a strong resemblance of gene signatures
254 repressed by PP and SON OE that are enriched in the control of cell dynamics, under basal
255 condition in the absence of ER stress (**Extended Data Fig. 13a-e**). Lastly, like SON (**Extended**
256 **Data Figs. 5d and 6d**), PP also improves the splicing fidelity of splicing genes themselves
257 (**Extended Data Fig 14a-f**), again reflecting autoregulation of splicing factors. Taken together,
258 these results indicate that PP is a bona fide nuclear speckle rejuvenator that induces a
259 transcriptional signature in MEFs highly similar to that of SON OE cells under both basal and
260 proteotoxic stress conditions.

261 **PP reduces the surface tension of nuclear speckle condensates via targeting SON IDR.**

262 To confirm that PP rejuvenates nuclear speckles in an SON-dependent manner, we knocked
263 down *Son* via siRNA in MEFs. Son knockdown leads to smaller and more spherical speckles,
264 consistent with our previous study [19] (**Fig. 2h**). Importantly, PP's ability to reduce nuclear speckle
265 sphericity is abolished in *Son* knockdown MEFs (**Fig. 2h**)**.** Subsequently, *Son* knockdown
266 impaired PP's capacity to both activate protein quality control gene expression and repress YAP1
267 transcriptional output (**Fig. 2i**). To determine whether PP can physically interact with SON in
268 MEFs, we performed cellular thermal shift assay (CETSA), which is based on ligand-induced
269 thermal stabilization of target proteins, whereas unbound proteins denature, aggregate and

precipitate at elevated temperatures, ligand-bound proteins remain soluble due to increased stability [42,43]. Using a SON-specific antibody (**Extended Data Fig. 15a**), we found that PP induced a thermal shift of SON with a direction consistent with stabilization (**Fig. 3a**). As negative controls, we found that PP does not stabilize SRSF2 (SC35), another nuclear speckle protein, or the ISR/UPR TF ATF4, whose expression is nonetheless significantly increased by PP (**Fig. 3b and Extended Data Fig. 15b**).

SON is the central scaffold protein of nuclear speckles [44-46], and its ~12h rhythmic concentration fluctuation drives ~12h rhythmic nuclear speckles LLPS dynamics and chromatin binding alternating between either a diffuse and chromatin-associated state or a punctate and chromatin-dissociated state [9]. By contrast, SRSF2(SC35) is one of the critical subunits of the spliceosomes, which have a broader spatial distribution also occupying the periphery of nuclear speckles, particularly at the interface between nuclear speckles and the nucleoplasm or chromatin and is not essential for speckle formation [47,48]. In MEFs, PP generated a more diffuse and irregular (less spherical) nuclear speckles with larger surface area (**Fig. 2b, c**), suggesting that PP could influence nuclear speckle LLPS dynamics, likely via reducing the surface tension of speckle condensates (surface tension is the tendency of liquid droplets to minimize the total surface area, therefore an increased surface area is suggestive of reduced surface tension[49]). Given the CETSA data indicating PP can bind to SON directly, we next tested whether PP can directly impact the condensates formation of two nuclear speckle protein, SRSF2 and SON, using an *in vitro* droplet formation assay [50]. Using different computational algorithms to search for intrinsically disordered domain (IDR) [51-53], we identified two IDRs at the N and C terminals of mouse SON, and long stretches of IDRs spanning two-thirds of mouse SRSF2 (**Fig. 3c and Extended Data Fig. 15c**). We separately cloned the regions encoding both SON IDRs and the full-length SRSF2 into the C-terminal of mCherry and purified recombinant proteins from *E. coli* (**Extended Data Fig. 15d**). Purified recombinant proteins were added to buffers containing 10% crowding reagents PEG-8000 as previously described [50]. Confocal fluorescence microscopy of the different protein solutions revealed mCherry positive, micron-sized spherical droplets freely moving in solution and wetting the surface of the glass coverslip (**Extended Data Movies 1-3**). All proteins droplets were highly spherical, exhibited fusion/coalescence behaviors (**Extended Data Movies 1-3**), and scaled in size and number positively with increasing concentration of proteins and negatively with increasing salt concentration (**Extended Data Fig. 15e, f**), all properties expected for liquid-like droplets [50].

Due to surface tension, small droplets will eventually morph into a fewer number of large droplets, resulting in a net decrease of surface area, either via coalescence or Ostwald ripening [54] (**Fig. 3d**), which was seen for all protein droplets after 20 minutes of time lapse imaging (**Fig. 3e, f, and Extended Data Fig. 15g**). Addition of PP to SON IDR2, but not SON IDR1 and SRSF2 protein solutions, significantly reduced the kinetics of this process in a dose-dependent manner, resulting in a negligible decrease of relative surface area after 20 minutes (**Fig. 3d-f, and Extended Data Fig. 15g, h**). The significance of SON IDR2 is reinforced by the substantial evolutionary conservation of its sequences across seven distinct species spanning wide phylogenetic distances from zebra fish to humans (**Extended Data Fig. 15i**).

To better recapitulate the complex compositions of nuclear speckles, we further supplemented recombinant mCherry-SON IDR2 with nuclear extract (NE) from Hela cells that include all active components of transcription and splicing factors (**Extended Data Fig. 16a**) [50]. Mass spectrometry confirmed that Hela NE-supplemented mCherry-SON IDR2 condensates preferentially

compartmentalized splicing factors (including SRSF2), but not other nuclear proteins like proteasome subunits, DNA repair factors or general transcription factors (**Extended Data Fig. 16b, c**). These condensates further exhibited less spherical morphology, had increased number and total size (**Extended Data Fig. 16d, e**), features expected from nuclear speckle-like condensates with inhomogeneous viscoelastic properties [55]. Importantly, addition of PP reduced both the sphericity and surface tension of Hela NE-supplemented SON IDR2 condensates in a dose-dependent manner (**Fig. 3g-i**), consistent with the effects of PP on nuclear speckle morphology in cells. Together, these data suggest that PP can reduce the surface tension to stabilize both homotypic and heterotypical NE-supplemented SON condensates in a cell-free system, via interacting with SON C-terminal IDR2.

To investigate whether PP may affect the relative spatial distribution of SON and SRSF2 within nuclear speckles, we further supplemented recombinant mCherry-SON IDR2 with NE from GFP::SRSF2-expressing MEFs (**Fig. 3j**). The resulting nuclear speckle-like condensates recapitulated the anticipated spatial distribution of SON and SRSF2 proteins, with the former located at the center, and the latter exhibiting a broader distribution with its highest concentration often observed at 350nm away from the SON IDR2 center (**Extended Data Fig. 16f and Extended Data Movie 4**). While PP does not alter the relative spatial distribution of SON IDR2 and SRSF2, it reduced their sphericity, and markedly increased SRSF2 content at the periphery of nuclear speckle-like condensates (**Fig. 3k-m**). To determine whether PP may also influence the wetting of genomic DNA by nuclear speckles [56], we further added mouse genomic DNA into the droplet solution. In accordance with observations in intact cells, nuclear speckle condensates largely don't mix with, but can wet the DNA (**Extended Data Fig. 16g**). Interestingly, the addition of PP more than doubled the wetting of genomic DNA by the reconstituted nuclear speckles (**Fig. 3n, o**).

To validate that PP can alter the nuclear speckle LLPS properties *in vitro* in the context of intact cells, we further performed 1,6 hexanediol sensitivity assay [57] using the same EGFP::SRSF2 MEFs [9]. A short term 1,6 hexanediol treatment preferentially dissolves liquid but not solid condensates, thus a change in the sensitivity to 1,6 hexanediol reflects an alteration in the LLPS property of a given condensates [57]. As demonstrated in **Extended Data Fig. 17a, b**, PP desensitized SRSF2 to increasing concentrations of 1,6 hexanediol. This effect was not observed on two other biomolecular condensates, the nuclear MED1 [50] and cytosolic GW182 present in P-bodies [58] (**Extended Data Fig. 17c, d**). Taken together, these results suggest a mechanism where PP can reduce the surface/interfacial tension of nuclear speckles via targeting SON IDR, leading to larger surface areas with increased SRSF2 content at the periphery, increased wetting of genomic DNA and subsequently a higher portion of spliceosomes stably engaging in active RNA processing and transcription elongation of proteostasis genes. Since no active transcription occurs in the *in vitro* droplet formation assay, these results demonstrate that PP-mediated nuclear speckle LLPS change is a cause, rather than a consequence of or response to, global transcriptional reprogramming.

PP reduces both pathological Tau and rhodopsin levels by boosting ALP and UPS, at the expense of YAP1 signaling.

Since PP treatment leads to a global increase of protein quality control gene expression, we went on to determine the effects of PP on global protein synthesis, and degradation via ALP and UPS in MEFs. Using puromycin incorporation assay [59], we found that in spite of increased expression of many mRNAs involved in ribosome biogenesis and translation (**Fig. 2g**), PP elicited a

repression of global protein synthesis (**Fig. 4a, b**), an observation consist with the activation of the ISR [60]. To quantify the UPS activity, we treated MEFs with PP alone or in combination with the proteasome inhibitor MG132 and blotted for high molecular weight poly-ubiquitinated proteins. PP led to a significant reduction of poly-ubiquitinated protein levels (**Fig. 4c, d**), and co-treatment with MG132 caused a one-fold increase of their level, while under vehicle condition, only a very small (statistically not significant) increase was observed (**Fig. 4c, d**). These data collectively indicated that PP increases UPS-mediated degradation of poly-ubiquitinated protein. To measure autophagic flux, we blocked autophagy at the late stage autophagosome-lysosome fusion step using Bafilomycin A1 (BafA) [61], and quantified the level of LC3I and LC3II with or without PP. PP treatment resulted in an increased ratio of LC3II/I and reduced level of LC3II, both of which were significantly increased by BafA co-treatment to a level similar or higher than what was observed under DMSO condition (**Fig. 4e, f**). These results indicate that PP also augments autophagic flux. In sum, these results revealed that PP represses global protein synthesis while promoting both ALP and UPS.

Decline of both ALP and UPS are associated with proteinopathies such as Alzheimer's disease (AD), frontotemporal dementia (FTD), Parkinson's disease (PD) and a subtype of Retinitis pigmentosa (RP) with *RHODOPSIN* (*RHO*) mutations [62]. To determine whether PP can protect against proteinopathies via boosting UPS and/or ALP, we focused on two different diseases, a genetic form of RP with a mutant RHO, and tauopathy common in both AD and FTD. RP causes blindness via the primary loss of rods and secondary loss of cones. Proline to histidine at codon 23 (P23H) is the most common mutation in RHO protein, resulting in autosomal dominant RP in humans [63]. The heterozygous $Rho^{P23H/+}$ knock-in mouse develops progressive retinal degeneration that resembles the RP phenotype in patients [64,65]. Recently, several studies suggested that boosting ERAD can protect against mouse models of RP by increased elimination of the mutant RHO^{P23H} protein [64,66-68]. To determine if PP can also reduce RHO^{P23H} level, we used a NIH3T3 cell line ectopically expressing RHO^{P23H} protein [69]. Treating this cell line with 0.1 μM of PP for 24 hours led to a reduction of both monomer and dimer forms of RHO^{P23H} protein in an SON-dependent manner (**Fig. 4g, h, and Extended Data Fig. 18a**). Blocking the UPS, and to a lesser degree autophagy, abolished the effect of PP on reducing RHO^{P23H} protein level (**Fig. 4i, j, and Extended Data Fig. 18b**), suggesting that increased ERAD/UPS is likely mainly responsible for the increased elimination of RHO^{P23H} by PP.

Both UPS and ALP are involved in the degradation of tau protein in tauopathies [70-73]. To test the effect of PP on tau proteostasis in mouse primary neuronal cultures, we overexpressed human Tau carrying P301S mutation - an FTD-causing mutation in the human *MAPT* gene (Tau) [74]. After treatment with increasing concentrations of PP for 24 hours, a decline in both total and phosphorylated Tau (Ser396/404) was observed in a dose-dependent manner, with approximately 50% and 65% reduction in total and p-Tau, respectively, detected at 100nM PP (**Fig. 4k**). It is noteworthy that these reductions in Tau level occurred without any observable signs of cellular toxicity (**Extended Data Fig. 18c**). PP also promoted autophagic flux in neurons, as demonstrated by an increase of LC3 II/I ratio, decreased level of p62/SQSTM1 and increased autolysosome formation assayed with a duo-fluorescent autophagy reporter (**Fig. 4k and Extended Data Fig. 18d-f**) [75]. Blocking autophagic flux with BafA dampened the effects of PP on reducing cellular Tau level (**Fig. 4l, m**). As observed in fibroblasts, PP also promoted UPS activity in neurons; however, inhibiting proteasome activity with MG132 has minimal effects on PP's ability to reduce Tau level (**Extended Data Fig. 18g, h**). Consistent with PP's ability to boost UPS and ALP, PP increased the expression of genes involved in both pathways in P301S hTau-expressing

neurons (**Fig. 4n**). Collectively, these results indicate that increased autophagy flux largely underlies PP's effect in reducing Tau burden in neurons.

Nuclear speckle rejuvenation by SON OE or PP increases global protein quality control at the cost of reduced YAP1 signaling in both MEFs (**Fig. 2i**) and neurons (**Fig. 4n**), raising an interesting question of whether the downregulation of YAP1 signaling also contributed to PP's efficacy in alleviating proteinopathy. To address this question, we restored YAP1 signaling with previously published YAP1 activators XMU-MP-1 and/or TRULI [76,77,78]. We found that while XMU-MP-1 antagonized the downregulation of YAP1 target genes by PP as expected, it also potently dampened the upregulation of proteostasis genes (**Fig. 4o**). In addition, XMU-MP-1 negated PP's effect on reducing RHO^{P23H} level in NIH3T3 cells (**Extended Data Fig. 18i, j**). Similarly, TRULI also dampens PP's effect on reducing Tau level in primary neurons (**Extended Data Fig. 18k, l**). These results suggest that for nuclear speckle rejuvenation to achieve the maximum effectiveness in alleviating proteinopathy, it is essential to simultaneously uphold heightened protein quality control and reduced YAP1 activity.

PP protects against mouse retina degeneration *ex vivo* and alleviates tauopathy in *Drosophila*.

Next, we assessed the effectiveness of PP in ameliorating proteinopathies by utilizing animal models of RP and tauopathy. To determine whether PP has the potential to restore gene expression changes in the retina of $Rho^{P23H/+}$ mice, we performed RNA-seq in the retina of one and three months old wild-type and $Rho^{P23H/+}$ mice and compared the gene signatures of $Rho^{P23H/+}$ retina with that of PP (**Fig. 5a-e**). In the retina of one month-old $Rho^{P23H/+}$ mice, we observed a significant downregulation of protein transport and autophagy gene expression that showed large convergence with those upregulated by PP (**Fig. 5a, b**). This includes *Reep6* gene, which regulates protein trafficking in the ER and its loss-of-function mutation causes autosomal-recessive RP in both humans and mice (**Fig. 5e**) [79]. By three months, the downregulation of proteostasis gene expression persists in $Rho^{P23H/+}$ mice retina, concomitant with a significant increase of YAP1-mediated cell dynamics gene expression that also overlaps with PP-downregulated genes (**Fig. 5c-e**). To directly tested the efficacy of PP in protecting against RP, we treated retina explants isolated from $Rho^{P23H/+}$ mice with nanomolar range of PP for 10 days, and visible light optical coherence tomography (vis-OCT) imaging revealed a remarkable efficacy of PP in safeguarding the mouse $Rho^{P23H/+}$ retina explants from degeneration. Notably, the cell counts in the outer nuclear layer closely resembled that of the WT retina explant control (**Fig. 5f-j**), indicating the protective potential of PP against degenerative processes. Moreover, no noticeable indications of toxicity were observed throughout the entire duration of the experiment, further highlighting the safety profile of PP as a promising therapeutic candidate.

Pan-neuronal expression of wildtype human *MAPT* gene in *Drosophila* recapitulates essential features of tauopathies, including hyperphosphorylated and misfolded tau, age-dependent neuron loss, and reduced life span [80], and SON IDR2 is also conserved in flies (**Extended Data Fig 15i**). Thus, we next tested the efficacy of PP in ameliorating tauopathy in flies that express 2N4R isoform of human Tau (*MAPT*) pan-neuronally [$elav^{c155}$-Gal4: UAS-hTau1.13 (C155>UAS-hTau1.13)] as well as in control $elav^{c155}$-Gal4 (C155) flies [81]. Both C155>UAS-hTau1.13 and C155 flies were fed with either standard diet or diet supplemented with 25μM PP, which did not affect the normal development and growth of flies despite its effect in attenuating WNT and YAP1 signaling [82]. We quantified disease progression at different stages of fly development with both larval crawling and adult fly climbing assay at 14 and 21 days of age. PP feeding preserved motor

function in C155>UAS-hTau1.13 third instar larvae and adult flies, with their locomotor performance restored to a level similar to or even slightly higher than control C155 flies fed with a standard diet (**Fig. 5k, l**). Notably, PP also enhanced the motor function of adult wild-type control (C155) flies at 21 days of age (**Fig. 5l**). This improvement is likely linked to PP's ability to promote overall proteostasis, particularly protein turnover rates, a process known to prolong health and lifespan in flies [83]. Consistent with the overall phenotypes, PP significantly reduced the level of p-Tau and to a lesser extent total Tau in the brains of C155>UAS-hTau1.13 flies (**Fig. 5m**). Since p-Tau are prone to misfolding and aggregation, it supports the notion that PP is increasing the overall capacity of protein quality control to remove misfolded and aggregated proteins, while having negligible effects on normal protein functions.

PP has the potential for treating tauopathy in humans.

To determine the potential of PP for treating tauopathy in humans, we studied whether gene expression signatures that are opposite of PP can be observed in brain regions of human subjects with AD. We initially performed a post-hoc analysis of a total of nineteen bulk RNA-seq datasets encompassing hippocampus, entorhinal cortex, temporal cortex and frontal cortex regions in control and AD human subjects [84], and found that genes repressed by PP have increased expression in all four brain regions of human subjects with AD (such as *YAP1, TEAD1 and AMOT*) (**Extended Data Figs. 19 and 20a**). By contrast, genes that were upregulated by PP displayed significantly decreased expression in temporal cortex (such as genes involved in ERAD: *EDEM1, SEL1L*, autophagy: *ATG13*, protein folding: *HYOU1*, and tRNA aminoacylation: *GARS*, *IARS*) (**Extended Data Figs. 19 and 20a**). To validate these findings, we further analyzed an independent single-nucleus RNA-seq (snRNA-Seq) dataset in the prefrontal cortex regions of human individuals with varying degrees of AD pathology (**Extended Data Fig. 20b**) [85]. We found that proteostasis genes upregulated by PP are consistently downregulated in all cell types with strong prominence in neurons and oligodendrocytes in both early and late-stage human AD subjects (**Extended Data Fig. 20c, d**). Genes that are downregulated by PP (those enriched in regulation of cell dynamics by YAP1) are initially downregulated in all cell types in the early stage but significantly upregulated during the late stage of AD in all cell types but inhibitory neurons (**Extended Data Fig. 20e, f**). This early to late AD progression is concomitant with strong increase of tauopathy, but not amyloid burden in these individuals (**Extended Data Fig. 20b**). Consistent with *in vivo* data, we also observed a significant decrease of proteostasis gene expression as well as an increase of YAP1-TEAD2 target gene expression in human induced pluripotent stem cells (iPSC)-derived neurons that express the P301S 4R-Tau when compared to wild-type 4R-Tau control cells (**Fig. 6a-c**) [73]. These upregulated YAP1-TEAD2 target genes also overlap with those repressed by PP (**Fig. 6b**).

Finally, to directly test the efficacy of PP in reducing tauopathy in human, we utilized human iPSC-neurons harboring homozygous FTD-causing MAPT V337M mutation (herein referred to as V337M) and isogenic wild-type control cells [86] and treated both cell lines with nanomolar range of PP for 12 hours. Immunofluorescence against nuclear speckles marker SRRM2 revealed that compared to controls, V337M iPSC-neurons exhibited aberrant nuclear speckle morphology characterized by smaller size and more spherical shape, and PP treatment fully restored nuclear speckle morphology to normal size and diffuseness (**Fig. 6d, e**). Consequently, PP markedly reduced the level of p-V337M Tau via boosting the autophagic flux (**Fig. 6d-h**). Together, these findings indicate that PP treatment has great potential to normalize gene expression patterns and reduce Tau burden in AD/ADRD-affected humans with severe tauopathy. Further, these results

provide strong support for the decline of nuclear speckles LLPS dynamics (becoming smaller and more spherical) as a driver of tauopathy.

PP is a HORMINAM.

Taken together, our results indicate that the effects of PP are two-pronged. First, PP can induce modest stress to cells (**Fig. 6i**), likely due to its reported ability to trigger mitochondrial stress by increasing ROS levels and impeding mitochondrial functions [87-89]. Mitochondria stress can activate the ISR and ATF4 activation [90,91], which likely explains the strong induction of ATF4 protein level by PP. Secondly, our new data showed that by directly binding to SON and reducing the surface/interfacial tension of nuclear speckles and promoting their wetting of DNA, PP is a bona fide nuclear speckle rejuvenator capable of amplifying the stress response at the transcriptional level, entailing both the upregulation of global protein quality control gene expression and downregulation of YAP1-mediated genes underlying cellular dynamics (**Fig. 6i**). In light of the dual effects of PP, we tentatively name it as a Hormesis Initiator and Amplifier (HORMINAM), a new class of compounds capable of both initiating and amplifying the hormetic response. A key characteristic of HORMINAM is its capacity to trigger a significantly stronger stress response relative to the actual stress it exerts, similar to the effect of SON OE in the presence of Tu (**Fig. 6j**). Our reclassification of PP as a HORMINAM thus reconciles the two previously known effects of PP: inducing mitochondrial stress and inhibiting YAP/WNT signaling [21,23]. Intriguingly, a recent study using unbiased whole genome CRISPR screen to identify pyrvinium-genetic interactions revealed that knocking out spliceosome genes sensitized cells to pyrvinium-induced cell death [88]. Although the underlying mechanism for this observation was not addressed [88], our study herein provides a scientifically sound rationale for this observation: knocking out spliceosome genes abolishes the stress response-amplifying effect of pyrvinium without affecting its stress-inducing ability. The absence of a robust stress response following exposure to stress is anticipated to render cells more susceptible to cell death. It is important to recognize that while pyrvinium acts as both a nuclear rejuvenator and HORMINAM, these concepts are independent of each other. It is conceivable that novel compounds could function solely as a HORMINAM without affecting nuclear speckle LLPS, or vice versa.

Discussion

Several recent studies indicate that both the decline of nuclear speckle functions and dysregulated mRNA splicing are associated with proteinopathies in humans, including both tauopathy and RP. For example, two studies showed that elevated Tau aggregates have the capability to relocate to the nucleus, thereby directly modifying the characteristics of nuclear speckles [92,93]. In agreement with this study, a recently published Tau interactome in human iPSC neurons [94] also revealed strong enrichment of Tau-interacting proteins involved in regulating RNA splicing and RNA stability. Additionally, it was previously shown that cryptic splicing errors is associated with neurofibrillary tangle burden in human AD subjects [95]. In humans, among the 12 autosomal dominant RP genes identified, four encode ubiquitously expressed proteins involved in pre-mRNA splicing (including *PRPF31*, *PRPF8*, *PRPF3* and *RP9*), demonstrating the important roles of RNA processing in the pathogenesis of retinal degeneration [96]. These studies thus provide the rationale for nuclear speckle rejuvenation as a strategy for counteracting various proteinpathies.

Exploring the therapeutic potential of targeting biomolecule condensates represents an exciting avenue for research and drug development [97,98]. Our study serves as a proof-of-principle

540 showing that nuclear speckle LLPS can also be therapeutically targeted. Manipulating nuclear
541 speckle LLPS through SON overexpression is a conceptually viable approach. However, the
542 practical implementation of this strategy presents significant challenges due to the large size of
543 the human SON open reading frame, making it technically difficult to design gene therapy
544 targeting SON. That said, we cannot rule out the possibility that overexpression of specific
545 truncated SON domains, such as SON IDR2, may be sufficient to rejuvenate nuclear speckles,
546 and future efforts will be directed toward exploring such possibilities.

547 Through a high-throughput drug screen, we identified PP as a small nuclear speckle
548 rejuvenator by directly interacting with SON and modulating nuclear speckle LLPS dynamics.
549 Interestingly, pyrvinium is enriched with cationic amines and aromatic motifs, chemical features
550 that were predicted to partition into various nuclear condensates [99]. PP was originally developed
551 as an anthelmintic drug effective for treating pinworm infections [100]. Moreover, it has gained strong
552 recent interest as an anti-cancer reagent due to its ability to inhibit WNT signaling [100]. Our current
553 study further expands its therapeutic values to proteinopathies, including both reducing tauopathy
554 in neurons and flies and protecting against retina degeneration in an *ex vivo* mouse RP model.
555 Future efforts should be directed toward testing the toxicity and efficacy of this drug in mouse
556 models of neurodegenerative diseases. The possibility for the latter is made even more tantalizing
557 due to its ability to cross blood brain barriers in mice.

558 While we don't yet know the full detailed mechanisms by which PP modulates nuclear
559 speckles dynamics and boost proteostasis gene transcription, several lines of evidence suggest
560 that it does so in part by reducing the surface tension and consequently increasing the surface
561 areas of nuclear speckles via an SON-dependent manner. Our in vitro reconstitution system
562 further showed that reduced nuclear speckles surface tension by PP further facilitates nuclear
563 speckles wetting of chromatin [49]. Thus, since spliceosomes reside at the interfacial boundary
564 between nuclear speckles and nucleoplasm/chromatin[47], larger surface areas also entails a
565 higher probability of spliceosome stably engaging in mRNA processing and transcription
566 elongation. The mechanism by which PP reduces the surface tension of nuclear speckles is not
567 yet fully understood. While the straightforward explanation would be that PP acts as a surfactant,
568 this seems unlikely due to its lack of hydrophilic moieties. Alternatively, it is plausible that by
569 interacting with SON, PP weakens the intermolecular attractive interactions among different SON
570 proteins, and/or SON and IDRs of other nuclear speckle proteins due to screening effects, leading
571 to an overall reduction of surface tension of nuclear speckles, similar to what is previously
572 described for the effect of increasing salt concentration on reducing surface tension for protein
573 condensates [101,102]. The positive charge carried by pyrvinium adds to the allure of this hypothesis.
574 Further research is needed to elucidate the precise mechanisms by which PP influences the
575 surface tension of nuclear speckles.

576 Genetic and pharmacological rejuvenation of nuclear speckles by SON and pyrvinium share
577 similar transcriptome signatures, including upregulation of extensive protein quality control gene
578 expression, and intriguingly, downregulation of YAP1-regulated genes involved in cell migration,
579 cell proliferation, would healing, and extracellular matrix organization. The contrasting changes in
580 proteostasis and YAP1-mediated cell dynamics gene expression are observed in various cell lines
581 under proteostatic stress. Consequently, both SON overexpression and ER stress impeded cell
582 migration. Additionally, the expressions of these genes follow anti-phasic ~12h ultradian rhythms
583 in mouse liver under normal physiological conditions. These findings demonstrate that YAP1
584 signaling is an inherent component of global transcriptional control of proteostasis. One possible

585 explanation for this phenomenon is that cells need to allocate their energy towards enhancing
586 overall proteostasis, which may come at the cost of cell proliferation, migration, and extracellular
587 matrix organization. Therefore, an energetic trade-off between proteostasis and cell dynamics
588 control could be crucial for maintaining cellular functions when faced with fluctuating
589 environments, such as proteotoxic and ER stress.

590 Nuclear speckles play a vital role in coordinating the opposing changes observed in
591 proteostasis and cell dynamics regulation. Elevated SON expression facilitates increased
592 physical interactions between nuclear speckles and XBP1s, leading to augmented transcription
593 of proteostasis genes. Since the number of proteostasis genes under the control of SON
594 surpasses those directly regulated by XBP1s, we postulate that nuclear speckles can be recruited
595 to additional proteostasis bZIP TFs upon rejuvenation, possibly via increased wetting between
596 nuclear speckle and TF-mediated condensates [49]. Future work with unbiased profiling of nuclear
597 speckle composition (via proximity labeling for example) can unveil the detailed molecular
598 mechanisms through which nuclear speckle rejuvenation globally activates the proteostasis gene
599 program. On the other hand, much less is clear on how nuclear speckle rejuvenation represses
600 YAP1 transcription activity. Upon SON overexpression and pyrvinium treatment, we found
601 significantly reduced level of nuclear YAP1 protein and a lower nucleus/cytosol ratio, indicating
602 an active nuclear exclusion of YAP1 protein. Like nuclear speckles, YAP1 can also form
603 biomolecular condensates, and a recent study reported that YAP1 nuclear condensates and the
604 nuclear speckles showed limited nuclear co-localization [103], suggesting a low level of wetting of
605 these two condensates under normal physiological conditions. Pending further investigation, we
606 speculate herein that nuclear speckle rejuvenation may further reduce the wetting of these two
607 condensates, resulting in the alteration of YAP condensate composition, and ultimately its nuclear
608 exclusion.

609 While both proteostasis and YAP1 signaling are downstream of nuclear speckles, direct
610 antagonistic reciprocal interactions between these two are likely to be present as well. A recent
611 study reported that in *Drosophila*, the proteostasis output gene Bip can sequester the fly YAP1
612 ortholog Yorkie, in the cytoplasm to restrict Yorkie transcription output [104]. Conversely, in
613 undifferentiated pleomorphic sarcoma, YAP1 can suppress PERK and ATF6-mediated UPR
614 target expression, and treatment with the YAP1 inhibitor Verteporfin upregulated the UPR and
615 autophagy [105]. The latter is further consistent with our findings showing that restoring YAP1 activity
616 dampened the efficacy of PP on activating protein quality control gene expression and reducing
617 proteinopathies. These findings indicate that in order to maximize the effectiveness of nuclear
618 speckle rejuvenation, it is crucial to maintain elevated levels of protein quality control while
619 simultaneously reducing YAP1 activity. Thus, a delicate balance between protein quality control
620 and YAP1 activity appears essential for effective nuclear speckle rejuvenation. This observation
621 may also explain why therapies merely aimed at activating protein quality control pathways often
622 have limited efficacies. Supporting this notion, while reduced expression of genes involved in
623 ERAD and autophagy are observed in the brains of individuals with AD, these subjects also exhibit
624 elevated gene expression of *YAP1*, *TEAD1,* and other YAP1 target genes, consistent with
625 previous studies [84,106]. Increased YAP1 target gene expression was further observed in human
626 iPSC tauopathy model as well as in the retina of Rho $^{P23H/+}$ mice. These results collectively
627 highlight the importance of suppressing YAP1 signaling as a potential strategy for managing both
628 AD and RP.

In conclusion, our study makes substantial conceptual contributions to the broader proteostasis framework by incorporating nuclear speckle LLPS and YAP1 signaling as critical components. From a translational perspective, our research unveils the promising therapeutic potential of nuclear speckle rejuvenation in tackling proteinopathies, achieved by simultaneous activation of protein quality control and inhibition of YAP1 activity. Additionally, our findings underscore the significance of harnessing the 12-hour oscillator to unveil hidden principles of proteostasis control.

Materials and methods

Mice

For retinal explant studies, wildtype C57BL/6J and Rho$^{P23H/+}$ knock-in mice (Jackson Laboratory Strain #017628) were euthanized by CO2 and retinae were isolated for culture. The animal studies were carried out in accordance with the National Institutes of Health guidelines and were granted formal approval by the University of Pittsburgh's Institutional Animal Care and Use Committee (approval numbers IS00013119 and IS00023112).

Larva crawling assay

PP solubilized in DMSO were diluted directly into the fly medium at the final concentration of 25 μM and vortexed extensively to obtain homogeneous culture. Crawling assays were performed on 1.5% agarose plates made with a 2.3:1 combination of grape juice and water. A sample size of 10 to 15 larvae were selected for each genotype and assays were done using larvae in the third instar state. The larvae were first removed from vials and gently placed into a petri dish containing deionized water to allow for residual food to be washed off the body. After 15 seconds, the larvae were transferred to a petri dish containing the 1.5% agarose mixture and were given one minute to rest. They were then transferred to a second dish filled with the 1.5% agarose mixture and timed immediately for one minute, during which their crawling performance was measured. A transparent plastic lid was placed on top of the plates and the crawling path of the larvae were traced. Observations of the crawling activity were done under a light microscope. The brightness and distance of the light source above the plates were kept constant across all trials and genotypes. The crawling paths of the larvae were measured using FIJI ImageJ and the average distance traveled was taken for each genotype.

Adult fly climbing assay

Male adult Drosophila melanogaster flies at 14 and 21 days of age fed with a normal diet or diet supplemented with 25 μM PP were used for assessing climbing ability. Flies were grouped into cohorts of the same sex, pre-mated, and age-matched, with a maximum of 20 individuals per vial (usually 5-15). All flies used in each trial were hatched within a 3-day window. The evening prior to each assay, flies were gently transferred to fresh tubes to allow for grooming and access to food. To ensure consistent conditions, assays were conducted at approximately the same time of day with a consistent ambient light setting. A custom climbing vial was employed, divided into six compartments, each labeled with a number (1 to 6) to denote climbing speed. The vial was positioned against a white background to enhance visibility during photography. Flies were transferred from their housing vial to the climbing vial, which was covered with a plastic plate on top. To initiate the assay, the flies were gently tapped to the bottom of the vial and allowed 10 seconds to climb. A cell phone camera was used to capture a photograph of the vial. Care was taken to ensure the camera was level with the vial, all flies were visible, and the background was

free from stains or spots. The number of flies in each compartment of the climbing vial was counted at each time point and recorded on a dedicated worksheet. Each cohort of flies underwent five consecutive trials, with approximately 1 minute of rest between each trial. The average score of each cohort was determined by dividing the total score by the total number of flies.

Fibroblast cell culture and drug treatment

MEFs and NIH 3T3 cells were cultured at 37°C and 5% CO_2 in Dulbecco's Modified Eagle's Medium (DMEM, glucose 4.5 g/L with phenol red) and supplemented with 10% fetal bovine serum (FBS), 1 mM sodium pyruvate (Gibco), and penicillin (100 U/mL)-streptomycin (100 µg/mL) (Gibco). Methods for the manipulation of *Son* (transient knockdown or constitutive overexpression) and validation of changes to protein (SON) levels with regards to the mRNA-Seq data are previously described in [9]. For Tu treatment, 100 ng/mL Tu (in DMSO) for six hours was used unless otherwise noted. NB (HY-50904), PB (HY-12047), PH (HY-B0883), PP (HY-A0293), MG-132 (HY-13259), and XMU-MP-1 (HY-100526) were purchased through MedChemExpress and BafA (1334) was purchased from Tocris. All drugs were handled per manufacturer instruction.

Primary neuron cell culture and P301S-Tau virus infection

The cerebral cortices of 3-4 neonate mice (P0) were dissected on ice, the meninges were removed, and placed in the cold dissection medium (DM), consisting of 6 mM MgCl2 (Sigma M1028-100 ml), 0.25 mM CaCl2 (Sigma C7902), 10 mM HEPEs (100X), 0.9% Glucose, 20 µM D-AP5 (Cayman, NC1368401), and 5 µM NBQX (Tocris Bioscience, 10-441-0). After dissection, the brain tissues were washed with DM 1~2 times and incubated with 13mL of DM containing papain (Worthington, LK003176) in 37°C water bath for 20 min. The suspension was shaken every 5 min. 10mL media containing 18 ml DM + 2 ml low OVO + 133 ul DNase I (dilute 10X low OVO and 150x DNase I to DM) were added into the suspension to stop the digestion in 37°C water bath for 5 min. The solution was taken off and 10 ml fresh solution was added in. Then the tissues were triturated until there were no visible chunks, and the solution was filtered through the 70 µm cell strainer. The cell solution was then centrifuged at 1000 rpm for 10 min and the supernatant was discarded. The cell pellet was gently resuspended in 20 ml B27/NBM/High glucose media, and the suspension was centrifuged at 850 rpm for 5 min. After that, the supernatant was taken off and B27/NBM (1 ml/mouse brain) was added to resuspend the cells until single cell solution. The cells were counted and plated onto the coverslips at 250k in 24-well plates for imaging or 800k in 12-well plates for qRT-PCR or Western blots. AAV-P301S hTau (Viro-vek) were infected at DIV1 at 100 MOI.

Human iPSC-derived neurons culture

Human iPSC-derived neurons were pre-differentiated and differentiated as described [86]. Briefly, iPSCs were pre-differentiated in Matrigel-coated plates or dishes in N2 Pre-Differentiation Medium containing the following: KnockOut DMEM/F12 as the base, 1× MEM non-essential amino acids, 1× N2 Supplement (Gibco/Thermo Fisher Scientific, cat. no. 17502-048), 10 ng/ml of NT-3 (PeproTech, cat. no. 450-03), 10 ng/ml of BDNF (PeproTech, cat. no. 450-02), 1 µg/ml of mouse laminin (Thermo Fisher Scientific, cat. no. 23017-015), 10 nM ROCK inhibitor and 2 µg /mlof doxycycline to induce expression of mNGN2. After 3 d, on the day referred to hereafter as Day 0, pre-differentiated cells were re-plated into BioCoat poly-D-lysine-coated plates or dishes (Corning, assorted cat. no.) in regular neuronal medium, which we refer to as +AO neuronal medium, containing the following: half DMEM/F12 (Gibco/Thermo Fisher Scientific, cat. no. 11320-033) and half neurobasal-A (Gibco/Thermo Fisher Scientific, cat. no. 10888-022) as the

base, 1× MEM non-essential amino acids, 0.5× GlutaMAX Supplement (Gibco/Thermo Fisher Scientific, cat. no. 35050-061), 0.5× N2 Supplement, 0.5× B27 Supplement (Gibco/Thermo Fisher Scientific, cat. no. 17504-044), 10 ng/ml of NT-3, 10 ng/ml of BDNF and 1 μg/ml of mouse laminin. Neuronal medium was half-replaced every week.

Efficacy test of PP in Retina explant culture

Wild type and *Rho*$^{P23H/+}$ mice were euthanized at P15 and retina explants were isolated and cultured as previously described[107,108]. Briefly, eyeballs were enucleated and incubated in Ames solution containing 0.22 mM L-cysteine (Sigma-Aldrich) and 20 U papain (Worthington, Freehold NJ, USA) at 37 ºC for 30 min. The digestion was stopped by transferring the eyes to Dulbecco's modified Eagle's medium (DMEM; Gibco) containing 10% fetal calf serum (FCS; Gibco) and penicillin &streptomycin antibiotics (1x, GenClone) at 4 ºC for 5 min. The eye cup was made by gently removing the cornea, iris and lens. Each eye cup was flattened by four radio cuts and the sclera was then carefully peeled off from the retina:RPE complex. The retina:RPE explant was transferred to a trans well insert with 0.4-micron pore polycarbonate membrane (ThermoFisher) sitting on the surface of 1.5 mL of neurobasal-A plus medium (Gibco) containing 2% B27 supplement (Gibco) in a 6-well cell culture plate, and the RPE layer was facing down the transwell membrane. The retinal explants were cultured at 37 ºC with 5% CO_2.The medium was replaced with fresh medium containing 0.5 μM PP after 24 h, which was replaced again every 2 days until 10 days in culture (DIV). A visible light optical coherence tomography (vis-OCT) prototype [109] was utilized to monitor the explants noninvasively at day 0 and day 10. Retinal layers were segmented automatically using a deep learning method and then manually corrected by a customized software to calculate the retinal thickness. Retina explants were collected at 10 DIV and processed for fixation, dehydration, paraffin embedding, cross-sections, dewaxing, rehydration and hematoxylin and eosin (H&E) staining[110]. H&E stained slides were imaged by regular light microscopy with a color camera, and the number of nuclei in the outer nuclear layer (ONL) was calculated manually.

Autophagy reporter assay

To express the LC3 reporter in the neurons, the primary mouse neuronal cultures were infected with the homemade lentivirus-mCherry-GFP-LC3 for 7 days. The florescent signal from the vacuoles at different stages were acquired by confocal imaging. The mCherry-GFP-LC3 fluorescence images were acquired with a Leica TCS SP8 confocal system using 63x oil-immersion objective. 488 nm and 568 nm laser were used to excite the GFP and mCherry, respectively. Images were taken with the same confocal settings. Minor image adjustment (brightness and/or contrast) was performed in ImageJ. The GFP and mCherry signal collected were merged into one image to quantify the red, green, and yellow vacuoles for quantification of different types of vacuoles. The different colored fluorescent signal was manually counted in each cell, and each point represents the average number of the specific vacuole for one cultured cell.

Scratch assay

Cells were grown until 100% confluent, ER stress was induced as previously described, and then a single scratch was performed with a pipette tip per well. Cells were imaged immediately after scratching (0hr) and then after 23hr. The Cell Profiler [111] "Wound Healing" pipeline (https://cellprofiler.org/examples) was used to measure the "Percentage of Gap Filled".

Immunoblot

759 Different cells were harvested and fractionated to produce cytosolic and nuclear lysates using the
760 NE-PER kit (Thermo Fisher Scientific). For whole cell lysates, cells were lysed in RIPA buffer.
761 Both protease and phosphatase inhibitors were included in the respective lysis buffer. ~47 µg of
762 protein was separated on a 4%-15% gradient SDS-polyacrylamide gel (Bio-Rad) which were
763 transferred to nitrocellulose membranes, stained with Ponceau S stain, washed, blocked with 5%
764 non-fat milk, and incubated overnight at 4°C with the following primary antibodies: anti-α-Tubulin
765 (Cell Signaling Technology (C.S.T.) #2144), anti-Lamin A/C (C.S.T. #4777), anti-SON (Abcam
766 #121033 and LSBio LS-C803664), anti-YAP1 (C.S.T. #12395), anti-GFP (C.S.T. #2956), anti-Tau
767 (Sigma-Aldrich, #A0024), anti-p-Tau (a gift from Dr. Peters Davies), anti-β-actin (C.S.T. #4970),
768 anti-puromycin (BioLegend 381502), anti-ubiquitin (C.S.T. #58395), anti-LC3-I/II (C.S.T. #2775),
769 anti-p62 (C.S.T. #23214), anti-ATF4 (C.S.T. #11815), anti-ATF6 (Novus 70B1413.1), and anti-
770 XBP1s (BioLegend 658802). Membranes were treated with the appropriate secondary antibody
771 conjugated to horseradish peroxidase the following day and then ECL Prime Western Blotting
772 Detection Reagent (Cytiva) was applied. A Bio-Rad ChemiDoc MP Imaging System was used to
773 visualize the signal, and signal intensities were determined with ImageJ [112].

774 **Cellular thermal shift assay (CETSA)**

775 EGFP::SC35 MEFs with EGFP knocked into the N-terminal of mouse *Srsf2* locus (previously
776 described in [9]) were treated with either DMSO or 3µM PP for 50 minutes at 37°C. Cells were then
777 trypsinized and resuspended in PBS with either DMSO or 3µM PP and 100 µL of the suspensions
778 were distributed to PCR tubes for the thermal shift assay (three minutes at a range of
779 temperatures). The temperatures used were: 42.0°C, 42.5°C, 43.9°C, 46.2°C, 49.3°C, 53.3°C,
780 57.9°C, 62.1°C, 65.2°C, 67.8°C, 69.2°C, and 70.0°C. After the samples were heated, they sat at
781 20°C for three minutes, were snap frozen in liquid nitrogen and thawed for three cycles to lyse
782 the cells, and then spun at 20,000 x g for 20 minutes at 4°C. The supernatant was then removed,
783 and immunoblotting was performed using anti-GFP (C.S.T. #2956), anti-ATF4 (C.S.T. #11815),
784 and anti-SON (Lifespan Biosciences #LS-C803664-100), followed by appropriate secondary
785 antibody. Band intensity on the blots were relative to the intensity of the 42°C band and were
786 normalized so that this band's (42°C) intensity was set equal to 1.

787 **Protein purification and *in vitro* droplet formation assay**

788 Regions of SON and the entire SRSF2 protein were fused to mCherry. cDNA encoding the SON-
789 IDR N terminal (region 1), SON-IDR C-terminal (region 2), and SRSF2 were each cloned into the
790 expression vector pET21a (+)-Histag-mCherry (Addgene plasmid # 70719) (Niederholtmeyer et
791 al., 2015). The plasmids obtained were transformed into C3013 *E. Coli* (NEB C3013I). Fresh
792 bacterial colonies were inoculated into LB media containing ampicillin and grown overnight at
793 37°C. Overnight cultures were diluted in 500mL of LB broth with ampicillin and grown at 37°C until
794 reaching OD 0.6. IPTG was then added to 2mM, and growth continued for 3h at 37°C. The cells
795 were pelleted and stored frozen at -80°C. Bacterial pellets were resuspended in 15mL of Buffer
796 A (50 mM Tris-HCl, 500 mM NaCl) containing protease inhibitors (Pierce, A32965) and 10mM
797 imidazole. The suspension was sonicated on ice for 15 cycles of 30 sec on, 30 sec off. The lysate
798 was centrifuged for 40 minutes at 15,000 RPM at 4°C to clear debris, then added to 2mL of
799 preequilibrated Ni-NTA agarose beads (Qiagen cat no. 30210). The agarose lysate slurry
800 incubated for 1.5hrs at 4°C with rocking, then allowed to flow through the column. The packed
801 agarose was washed with 15mL of Buffer A with 10mM imidazole. Protein was eluted with 5mL
802 of Buffer A containing 15mM imidazole, 10mL Buffer A containing 100mM imidazole, then 10mL
803 Buffer A containing 200mM imidazole. All elutions were collected in 1mL fractions. Aliquots of the

804 collected fractions were run on an SDS-PAGE gel and stained with Imperial Protein Stain to verify
805 amount and purity of the protein. Fractions containing protein were combined and dialyzed against
806 Dialysis Buffer (50mM Tris-HCl, 500mM NaCl, 10% glycerol, 1mM DTT). Recombinant mCherry
807 fusion proteins were concentrated and desalted to 200uM protein concentration and 125mM NaCl
808 using Amicon Ultra centrifugal filters (MilliporeSigma cat no. UFC801024) following
809 manufacturer's instructions. 20uM of recombinant protein was added to Droplet Buffer (50mM
810 Tris-HCl, 10% glycerol. 1mM DTT, 10% PEG) containing indicated final salt and pyrvinium
811 concentrations. For droplet formation assay with Hela nuclear extract supplementation, NE was
812 added to different concentration of SON IDR2 at the final concentration of 1.5mg/ml in Droplet
813 buffer (20mM HEPES, pH 7.9, 20% glycerol, 125mM KCl, 0.2mM EDTA, 0.5mM DTT, 10% DEG).
814 For droplet formation assay with GFP::SRSF2 MEF nuclear extract supplementation, NE was
815 added to 10uM SON IDR2 at the final concentration of 0.6mg/ml in Droplet buffer. A custom
816 imaging chamber was created by placing strips of tape on a glass coverslip, forming a square.
817 The protein solution was immediately loaded onto the center of the square and covered with a
818 second glass coverslip. Slides were then imaged with a Leica confocal microscope with a 63x oil
819 objective. Image series were taken over a 20-minute time span with 1 image every 30 seconds.

820 **Mass spectrometry to profile condensates composition**

821 Hela nuclear extract samples were thawed at room temperature, vortexed for 10 minutes, bath
822 sonicated for 5 minutes and centrifuged at 13000g for 10 minutes at room temperature prior to
823 quantification of total protein by a Pierce 660 Protein Assay (Thermo Scientific #22660).
824 Condensates were obtained by centrifuging at 10,000xg for 10 minutes and resuspended in
825 5%SDS in 50 mM TEAB prior to total protein quantification. Protein digestion was carried out on
826 10 µg of protein from each sample on S-trap micro columns (Protifi) according to the
827 manufacturer's protocol. Following digestion, peptide samples were then dried in a speedvac and
828 resuspended in a solution of 3% acetonitrile and 0.1% TFA and desalted using Pierce Peptide
829 Desalting Spin Columns (Thermo Scientific # 89851). Eluants were dried in a speedvac and
830 resusupended in a solution of 3% acetonitrile and 0.1% formic acid to a final concentration of 0.5
831 µg/µL. Mass spectrometry analysis was conducted on a Thermo Fisher QE-HFX coupled to a
832 Vanquish Neo UHPLC. Approximately 1 □g of each sample was loaded onto an EASY-Spray
833 PepMap RSLC C18 column (2 □m, 100A, 75□m x 50 cm) and eluted at 300 nl/min over a 120-
834 minute gradient. MS1 spectra were collected at 120,000 resolution with a full scan range of 350
835 – 1400 m/z, a maximum injection time of 50ms and the automatic gain control (AGC) set to 3e6.
836 The precursor selection window was 1.4 m/z and fragmentation were carried out with HCD at
837 28% NCE. MS2 were collected with a resolution of 30,000, a maximum injection time of 50ms
838 and the AGC set to 1e5 and the dynamic exclusion time set to 90s. The collected MS data were
839 analyzed using MSFragger V4.0[1] and searched against the human SwissProt database. The
840 search parameters were set as follows: strict trypsin digestion, missing cleavage up to 2,
841 carbamidomethylation of cysteine as static modification, oxidization of methionine and protein N-
842 terminal acetylation as variable modification, a maximal mass tolerance of 20 ppm for the
843 precursor ions and 20ppm for the fragment ions, and false detection rate (FDR) was set to be 1%.

844 **1,6-hexanediol treatment to examine effects of PP on LLPS**

845 A 10% (w/v) 1,6-hexanediol (1,6-HD, MilliporeSigma) solution was prepared in Dulbecco's
846 Modified Eagle's Medium (DMEM, glucose 4.5 g/L with phenol red) supplemented with 10% fetal
847 bovine serum (FBS), 1 mM sodium pyruvate (Gibco), and penicillin (100 U/mL)-streptomycin (100
848 µg/mL) (Gibco). To examine NS LLPS dynamics, EGFP::SC35 MEFs (previously described in [9])

were treated with DMSO or 1 μM PP for 30 minutes and then treated with 0, 1, 2, or 10% 1,6-HD for 20 minutes. Cells were fixed in 2% paraformaldehyde, stained with bisBenzimide H 33258 (Hoechst), and then imaged. Image analysis was completed in Cell Profiler; briefly, the process was to image the cells in the 405 (Hoescht), 488 (GFP), and 555 (high intensity to image whole cells) and then use the 405 channel to determine the nuclei boundaries, 488 to determine EGFP::SC35, and 555 to determine the area of the whole cells. We differentiated nuclear and cytosolic areas by subtracting the 405 signals from the 555 signals. 488 signal was then quantified in the aforementioned nuclear area and cytosolic area and compared. 20+ cells were measured for each condition. The average Manders coefficient was determine with ImageJ [112] by averaging the tM1 and tM2 values.

This same process was used to examine the effects of PP on GW182 and MED1 except in wildtype MEFs. The signal was identified by immunofluorescence (IF). Briefly, IF was performed by fixing cells with 4% paraformaldehyde in PBS, permeabilizing with 0.2% Triton X-100 in PBS, blocked with 2% bovine serum albumin in PBS, and then incubated with primary antibody (GW182 (ab156173, Abcam) or MED1 (ab60950, Abcam)) diluted per manufacturer's recommendation overnight at 4°C. Cells were then treated with the appropriate 1:1000 secondary antibody overnight at 4°C, stained with Hoechst the following day, and then mounted with ProLong Gold Antifade (Invitrogen). Signal (either IF or endogenous GFP) sphericity was determined as previously described in [9]. 20+ cells were measured for each condition.

Reverse transcription quantitative polymerase chain reaction (RT-qPCR)

For Reverse transcription-quantitative polymerase chain reaction (RT-qPCR), cDNA was produced using the Superscript III (Thermo Fisher) kit and qPCR was completed using the SYBR Green system (Thermo Fisher) in a CFX384 Real-Time System (Bio-Rad). Endogenous *β-actin* levels were used as controls. The qPCR primer sequences were as follows:

β-actin forward: AAGGCCAACCGTGAAAAGAT
β-actin reverse: GTGGTACGACCAGAGGCATAC
Amot forward: CTGGAAGCAGATATGACCAAGT
Amot reverse: GGTGTTAGGAGAGTGGCTAATG
Atf4 forward: CCACTCCAGAGCATTCCTTTAG
Atf4 reverse: CTCCTTTACACATGGAGGGATTAG
Atg4c forward: GTGCGGAATGAGGCTTATCA
Atg4c reverse: CCAGACTTCTTCCCAAACTCTATC
Bmp4 forward: AACGTAGTCCCAAGCATCAC
Bmp4 reverse: CGTCACTGAAGTCCACGTATAG
Ern1 forward: TCCTAACAACCTGCCCAAAC
Ern1 reverse: TCTCCTCCACATCCTGAGATAC
Fdz1 forward: GAGATCCACCTTCCAGCTTTAT
Fzd1 reverse: CACTCCCTCTGAACAACTTAGG
Hyou1 forward: GAGGCGAAACCCATTTTAGA
Hyou1 reverse: GCTCTTCCTGTTCAGGTCCA
Manf forward: GACAGCCAGATCTGTGAACTAAAA
Manf reverse: TTTCACCCGGAGCTTCTTC
Rnf166 forward: GAAGACACACTCCCGCTTTA
Rnf166 reverse: CTGAGACCAACTCTCCTTGTG
Sirt2 forward: CATAGCCTCTAACCACCATAGC

894 *Sirt2* reverse: GTAGCCTGTTGTCTGGGAATAA
895 *Sqstm1* forward: AACAGATGGAGTCGGGAAAC
896 *Sqstm1* reverse: AGACTGGAGTTCACCTGTAGA
897 *Tgfb3* forward: CCACGAACCTAAGGGTTACTATG
898 *Tgfb3* reverse: CTGGGTTCAGGGTGTTGTATAG
899 *Ube2q2* forward: TTCCTAAGCACCTGGATGTTG
900 *Ube2q2* reverse: CTCCTCCTCTTCCTCTTCTTCT
901 *Xbp1* forward: GGGTCTGCTGAGTCC
902 *Xbp1* reverse: CAGACTCAGAATCTGAAGAGG
903 Cul5 forward: GAACACAGGCACCCTCATATT
904 Cul5 reverse: AGTTACACTCTCGTCGTGTTTC
905 Psmg1 forward: CCAGTGGTTGGAGAAGGTTT
906 Psgm1 reverse: GGGTCTTGTAGTCTGTGATGTG
907 Atg14 forward: CATTCCCTGGATGGGCTAAA
908 Atg14 reverse: CCTCAGGAACAAGAAGGAAGAG
909 Yap1 forward: CCAATAGTTCCGATCCCTTTCT
910 Yap1 reverse: TGGTGTCTCCTGTATCCATTTC

911 **Chromatin Immunoprecipitation (ChIP)**

912 ChIP for SC35 was performed using anti-SC35 antibody (ab11826, Abcam) as previously
913 described [113]. Briefly, mouse liver samples were submerged in PBS + 1% formaldehyde, cut into
914 small (~1 mm3) pieces with a razor blade and incubated at room temperature for 15 minutes.
915 Fixation was stopped by the addition of 0.125 M glycine (final concentration). The tissue pieces
916 were then treated with a TissueTearer and finally spun down and washed twice in PBS. Chromatin
917 was isolated by the addition of lysis buffer, followed by disruption with a Dounce homogenizer.
918 The chromatin was enzymatically digested with MNase. Genomic DNA (Input) was prepared by
919 treating aliquots of chromatin with RNase, Proteinase K and heated for reverse-crosslinking,
920 followed by ethanol precipitation. Pellets were resuspended and the resulting DNA was quantified
921 on a NanoDrop spectrophotometer. An aliquot of chromatin (10 µg) was precleared with protein
922 A agarose beads (Invitrogen). Genomic DNA regions of interest were isolated using 4 µg of
923 antibody. Complexes were washed, eluted from the beads with SDS buffer, and subjected to
924 RNase and proteinase K treatment. Crosslinking was reversed by incubation overnight at 65 °C,
925 and ChIP DNA was purified by phenol-chloroform extraction and ethanol precipitation. ChIP-
926 qPCR for MEFs were essentially performed the same way as previously described with anti-SC35
927 (ab11826, Abcam) and anti-XBP1s antibody (Biolegend 658802), except that the MEFs were
928 directly fixed with 1% formaldehyde before subject to nuclei isolation and chromatin
929 immunoprecipitation. The primers used for ChIP-qPCR are as follows:

930 Gene desert forward primer: GCAACAACAACAGCAACAATAAC
931 Gene desert reverse primer: CATGGCACCTAGAGTTGGATAA
932 *Xbp1* promoter region forward primer: GGCCACGACCCTAGAAAG
933 *Xbp1* promoter region reverse primer: GGCTGGCCAGATAAGAGTAG
934 *Xbp1* gene body region forward primer: CTTTCTCCACTCTCTGCTTCC
935 *Xbp1* gene body region reverse primer: ACACTAGCAAGAAGATCCATCAA
936 *Manf* promoter region forward primer: ACAGCAGCAGCCAATGA
937 *Manf* promoter region reverse primer: CAGAAACCTGAGCTTCCCAT
938 *Manf* gene body region forward primer: CAACCTGCCACTAGATTGAAGA

Manf gene body region reverse primer: AGGCATCCTTGTGTGTCTATTT
Hyou1 promoter region forward primer: GACTTCGCAATCCACGAGAG
Hyou1 promoter region reverse primer: GACTTCTGCCAGCATCGG
Hyou1 gene body region forward primer: TGGAAGAGAAAGGTGGCTAAAG
Hyou1 gene body region reverse primer: TCCCAAGTGCTGGGATTAAAG

HTS of FDA-approved drugs and quantitative imaging analysis

EGFP::SC35 MEFs were seeded in black 384 well plate with glass bottom (Cellvis). The FDA-approved compound library (100nL per drug) was stamped to 384-well tissue culture plates using CyBio Well vario (Analytik Jena). Compound solutions were then added to the cell plate at the final concentrations of 10 μM using a BRAVO liquid handler. After 18 hours of treatment, culture media was removed, and cells were fixed with 4% PFA followed by DAPI staining. Cells were imaged using a GE INCELL 2200 with 60x lens. Maximum intensity projection images were captured, and nuclear speckles sphericity was quantified with CellProfiler as previously described in [9]. Briefly, for speckle i the sphericity is defined as equation 1:

$$\text{Sphericity } i = 2\sqrt{\pi} * \sqrt{\text{area}}\, i \div \text{circumference } i \quad (1)$$

So that a perfect circle will have a sphericity of 1, and a line will have a sphericity of 0. To calculate the average sphericity of a given image that has k total speckles, we calculated the area-weighted average as described in equation 2.

$$Average\ sphericity/image = \sum_1^k Sphericity\ i \times area\ i\ /\ \sum_1^k area\ i \quad (2)$$

For the secondary screening to determine if compounds affected nuclear speckles morphology in a dose-dependent manner, specific compounds were selected using a TTP Mosquito X1 followed by serial dilutions of compounds that were prepared using a Bravo automated liquid handling platform (Agilent). Cells were treated, imaged, and analyzed according to the same protocol described above. For the tertiary screen we used MEFs with a *Perk* promoter-driven dGFP as previously described [114]. Cells were treated with drugs of interest and either DMSO or Tu at the same time as described above and both GFP/cell and cell number were determined with CellProfiler as previously described [3]. For both dose-response and *Perk* promoter-driven dGFP experiments, eight biological replicates were performed per drug per dose.

mRNA-seq and transcriptome analysis

For all mRNA-seq or RT-qPCR, total mRNA was isolated and purified from MEFs using the PureLink RNA Mini Kit (Thermo Fisher). For mRNA-seq, samples were submitted to the UPMC Genome Center for quality control, mRNA library preparation (Truseq Stranded mRNA (poly-A pulldown), and sequencing (paired-end 101 bp reads and ~40 million reads per sample). Sequencing was performed on a NextSeq 2000 sequencer.

For the *Son* overexpression or knockdown (OE/KD) sequencing data, the raw RNA-seq FASTQ files were analyzed by FastQC for quality control. Adaptors and low-quality reads were filtered by Trimmomatic [115]. Then the processed reads were aligned by HISAT2 [116] against mouse reference mm10. For gene-level intron/exon quantification, bedtools software [117] was used to collect and count reads that aligned to any intron/exon of the given gene. If one read spans across multiple exons of the same gene, it will only be counted once. If one read spans intron/exon junction, it will only be counted as intron. The intron/exon count were normalized by gene length and total reads for FPKM normalization.

The analysis of drug-treated samples was done using Galaxy [118]: Trim Galore was used for quality control and trimming [119] and Salmon [120] was used to normalize the paired-end reads (TPM method). The online 3D RNA-Seq [121] pipeline was used to determine upregulated and downregulated genes, in addition to generating the PCA plot.

For RNA-seq of *Rho*$^{P23H/+}$ and wild-type mice, total RNA was isolated from retinae isolated from mice at 1, 3, and 6 months of age using TRIzol organic extraction. RNA-seq was performed by QuickBiology Inc. RNA integrity was checked by Agilent Bioanalyzer. Libraries for RNA-seq were prepared with KAPA Stranded mRNA-Seq poly(A) selected kit (KAPA Biosystems, Wilmington, MA) using 250 ng toal RNAs for each sample. Paired end sequencing was performed on Illumina HighSeq 4000 (Illumina Inc., San Diego, CA).

The reads were first mapped to the latest UCSC transcript set using Bowtie2 version 2.1.0[122] and the gene expression level was estimated using RSEM v1.2.15[123]. TMM (trimmed mean of M-values) was used to normalize the gene expression. Differentially expressed genes were identified using the edgeR program[124]. Genes showing altered expression with $p < 0.05$ and more than 1.5-fold changes were considered differentially expressed. Goseq was uesd to perform the GO enrichment analysis and Kobas was used to perform the pathway analysis.

mRNA splicing rates analysis

The mRNA processing rate was estimated by the simple kinetic model (equation 3) where pre-mRNA was converted to mature mRNA with the mRNA processing rate *Kp* and the mature mRNA is subject to decay with a constant decay rate *Kd*.

$$Pre - mRNA \xrightarrow{Kp} mature\ mRNA \xrightarrow{Kd} \tag{3}$$

Under basal condition (DMSO), we assume a steady state of mature mRNA expression whose level does not change over time; thus, we have:

$$\frac{d\ C(mature\ mRNA)}{dt} = Kp \times\ C(pre - mRNA) - C(mature\ mRNA) \times Kd = 0$$

$$Kp = \frac{C\ (mature\ mRNA) \times Kd}{C\ (pre - mRNA)} \tag{4}$$

Under *Son* overexpression or knocking down condition (condition 2), if we assume the mature mRNA degradation rate does not change with *Son* OE/KD (*K1*d=*K2*d), then the ratio of splicing rates between basal condition 1 and *Son* OE/KD condition 2 is given by:

$$\frac{Kp1}{Kp2} = \frac{C1\ (mature\ mRNA) \times C2(pre - mRNA)}{C1\ (pre - mRNA) \times C2\ (mature\ mRNA)} \tag{5}$$

Gene set enrichment analysis (GSEA)

GSEA was performed with software version 4.1.0. TPM quantification of transcriptome under different drugs or DMSO control was used as input for gene expression. Parameters used for the analysis: 1000 permutations, permutation type: gene set.

Intron retention detection

Intron retention events were detected by iREAD [34]. Intron retention events are selected with default settings T>=20, J>=1, FPKM>=2.

1017 **Gene ontology analysis**

1018 DAVID (Version 2021) [125] (https://david.ncifcrf.gov) was used to perform Gene Ontology analyses.
1019 Briefly, gene names were first converted to DAVID-recognizable IDs using Gene Accession
1020 Conversion Tool. The updated gene list was then subject to GO analysis using all Homo Sapiens
1021 as background and with Functional Annotation Chart function. GO_BP_DIRECT,
1022 KEGG_PATHWAY or UP_KW_BIOLOGICAL_PROCESS was used as GO categories. Only GO
1023 terms with a p value less than 0.05 were included for further analysis.

1024 **Motif analysis**

1025 Motif analysis was performed with the SeqPos motif tool (version 0.590) [126] embedded in Galaxy
1026 Cistrome using all motifs within the homo sapiens reference genome hg19 as background. LISA
1027 analysis was performed using webtool (http://lisa.cistrome.org/).

1028 **Statistical Analysis**

1029 Data were analyzed and presented with GraphPad Prism software. Plots show individual data
1030 points and bars at the mean and ± the standard error of the mean (SEM). One-tailed t-tests were
1031 used to compare means between groups, with significance set at $p < 0.05$. In instances where
1032 the p value is not shown, *, **, ***, and **** represent $p < 0.05$, 0.01, 0.001, and 0.0001,
1033 respectively.

1034 **Author contributions**

1035 Conceptualization, Y.C., X.C., and B.Z.; Methodology, W.D., B.B.C., S.L., S.P., Y.C., X.C., and
1036 B.Z.; Investigation, W.D., Y.T., S.K., S.Z., M.C., R.K.A., M.S., Y.N., M.Y., M.B.L., D.C., E.I., C.D.,
1037 H.W., S.L., S.P., B.B.C., Y.C., X.,C, and B.Z.; Writing – Original Draft, W.D., Y.C., X.C., and B.Z.;
1038 Writing – Review & Editing, all authors; Funding Acquisition, W.D., B.B.C., Y.C., X.C., and B.Z.;
1039 Resources, B.B.C. S.P., Y.C., X.C. and B.Z; Supervision, Y.C., X.C., and B.Z.

1040 **Acknowledgements**

1041 We would like to thank Drs. Yvonne Eisele, Yuan Liu and Toren Finkel (University of Pittsburgh
1042 School of Medicine, Pittsburgh, PA, U.S.A.) for their technical assistance and/or comments on
1043 the manuscript. W.D. was supported by grant T32 HL082610 through the National Institutes of
1044 Health (NIH), the Diana Jacobs Kalman/AFAR Scholarship for Research in the Biology of Aging
1045 through the American Federation for Aging Research, and fellowship F31 AG080998. B.B.C. was
1046 supported by grant 1R35HL139860 through the NIH. Y.C was supported by the R01 EY030991.
1047 X.C. was supported by National Institutes of Health grants R01AG074273 and R01AG078185. B.
1048 Zhu was supported by grants 1DP2GM140924 and 1R21AG071893 through the NIH, and a grant
1049 from Richard King Mellon foundation. This research was supported in part by the University of
1050 Pittsburgh Center for Research Computing through the resources provided. Specifically, this work
1051 used the HTC cluster, which is supported by NIH award number S10OD028483. This research
1052 project was supported in part by the Pittsburgh Liver Research Centre supported by NIH/NIDDK
1053 Digestive Disease Research Core Center grant P30DK120531, the Ophthalmology and Visual
1054 Sciences Research Center core grant P30 EY08098, the Eye and Ear Foundation of Pittsburgh
1055 and an unrestricted grant from Research to Prevent Blindness.

1056 **Declaration of interests**

B.B.C. is Co-founder of Koutif Therapeutic Inc., Co-founder and VP of Drug Discovery for Generian Pharmaceuticals, and Co-founder and C.S.O. of Coloma Therapeutics Inc..

Data availability

All raw and processed sequencing data generated in this study have been submitted to the NCBI Gene Expression Omnibus (GEO; http://www.ncbi.nlm.nih.gov/geo/) under accession numbers GSE224275. The mass spectrometry proteomics data have been deposited to the ProteomeXchange Consortium via the PRIDE partner repository with the dataset identifier PXD050371. All data needed to evaluate the conclusions in the paper are present in the paper and/or the Supplementary Materials.

References and Notes

1. Gestwicki, J.E. & Garza, D. Protein quality control in neurodegenerative disease. *Prog Mol Biol Transl Sci* **107**, 327-53 (2012).

2. Golde, T.E., Borchelt, D.R., Giasson, B.I. & Lewis, J. Thinking laterally about neurodegenerative proteinopathies. *J Clin Invest* **123**, 1847-55 (2013).

3. Zhu, B. et al. A Cell-Autonomous Mammalian 12 hr Clock Coordinates Metabolic and Stress Rhythms. *Cell Metab* **25**, 1305-1319 e9 (2017).

4. Zhu, B., Dacso, C.C. & O'Malley, B.W. Unveiling "Musica Universalis" of the Cell: A Brief History of Biological 12-Hour Rhythms. *J Endocr Soc* **2**, 727-752 (2018).

5. Meng, H. et al. XBP1 links the 12-hour clock to NAFLD and regulation of membrane fluidity and lipid homeostasis. *Nature Communications* **11**, 6215 (2020).

6. Pan, Y. et al. 12-h clock regulation of genetic information flow by XBP1s. *PLOS Biology* **18**, e3000580 (2020).

7. Ballance, H. & Zhu, B. Revealing the hidden reality of the mammalian 12-h ultradian rhythms. *Cellular and Molecular Life Sciences* (2021).

8. Asher, G. & Zhu, B. Beyond circadian rhythms: Emerging roles of ultradian rhythms in control of liver functions. *Hepatology* **n/a**(2022).

9. Dion, W. et al. Four-dimensional nuclear speckle phase separation dynamics regulate proteostasis. *Science Advances* **8**, eabl4150 (2022).

10. Meng, H. et al. Defining the mammalian coactivation of hepatic 12-h clock and lipid metabolism. *Cell Reports* **38**, 110491 (2022).

11. Scott, M.R. et al. Twelve-hour rhythms in transcript expression within the human dorsolateral prefrontal cortex are altered in schizophrenia. *PLOS Biology* **21**, e3001688 (2023).

12. Zhu, B. et al. Evidence for conservation of a primordial 12-hour ultradian gene program in humans. *bioRxiv*, 2023.05.02.539021 (2023).

1092 13. Zhu, B. & Liu, S. Preservation of ~12-h ultradian rhythms of gene expression of mRNA
1093 and protein metabolism in the absence of canonical circadian clock. *Frontiers in*
1094 *Physiology* **14**(2023).

1095 14. Spector, D.L. & Lamond, A.I. Nuclear speckles. *Cold Spring Harb Perspect Biol* **3**(2011).

1096 15. Hasenson, S.E. & Shav-Tal, Y. Speculating on the Roles of Nuclear Speckles: How
1097 RNA-Protein Nuclear Assemblies Affect Gene Expression. *Bioessays* **42**, e2000104
1098 (2020).

1099 16. Liao, S.E. & Regev, O. Splicing at the phase-separated nuclear speckle interface: a
1100 model. *Nucleic Acids Research* **49**, 636-645 (2020).

1101 17. Alexander, K.A. et al. Nuclear speckles regulate HIF-2α programs and correlate with
1102 patient survival in kidney cancer. *bioRxiv*, 2023.09.14.557228 (2023).

1103 18. Alexander, K.A. et al. p53 mediates target gene association with nuclear speckles for
1104 amplified RNA expression. *Mol Cell* **81**, 1666-1681 e6 (2021).

1105 19. Dion, W. et al. Four-dimensional nuclear speckle phase separation dynamics regulate
1106 proteostasis. *Science Advances* **8**, eabl4150 (2022).

1107 20. Jia, M. et al. Transcriptional changes of the aging lung. *Aging Cell* **22**, e13969 (2023).

1108 21. Schultz, C.W. & Nevler, A. Pyrvinium Pamoate: Past, Present, and Future as an Anti-
1109 Cancer Drug. *Biomedicines* **10**(2022).

1110 22. Zhang, C., Zhang, Z., Zhang, S., Wang, W. & Hu, P. Targeting of Wnt/β-Catenin by
1111 Anthelmintic Drug Pyrvinium Enhances Sensitivity of Ovarian Cancer Cells to
1112 Chemotherapy. *Med Sci Monit* **23**, 266-275 (2017).

1113 23. Thorne, C.A. et al. Small-molecule inhibition of Wnt signaling through activation of
1114 casein kinase 1α. *Nat Chem Biol* **6**, 829-36 (2010).

1115 24. Chavez, A. et al. Comparison of Cas9 activators in multiple species. *Nature methods* **13**,
1116 563-567 (2016).

1117 25. Qin, Q. et al. Lisa: inferring transcriptional regulators through integrative modeling of
1118 public chromatin accessibility and ChIP-seq data. *Genome Biology* **21**, 32 (2020).

1119 26. Cretenet, G., Le Clech, M. & Gachon, F. Circadian clock-coordinated 12 Hr period
1120 rhythmic activation of the IRE1alpha pathway controls lipid metabolism in mouse liver.
1121 *Cell Metab* **11**, 47-57 (2010).

1122 27. Pocaterra, A., Romani, P. & Dupont, S. YAP/TAZ functions and their regulation at a
1123 glance. *Journal of Cell Science* **133**, jcs230425 (2020).

1124 28. Panciera, T., Azzolin, L., Cordenonsi, M. & Piccolo, S. Mechanobiology of YAP and TAZ
1125 in physiology and disease. *Nature Reviews Molecular Cell Biology* **18**, 758-770 (2017).

1126 29. Piccolo, S., Dupont, S. & Cordenonsi, M. The Biology of YAP/TAZ: Hippo Signaling and
1127 Beyond. *Physiological Reviews* **94**, 1287-1312 (2014).

1128 30. Reich, S. et al. A multi-omics analysis reveals the unfolded protein response regulon and
1129 stress-induced resistance to folate-based antimetabolites. *Nature Communications* **11**,
1130 2936 (2020).

1131 31. Lu, X., Ng, H.-H. & Bubulya, P.A. The role of SON in splicing, development, and
1132 disease. *Wiley interdisciplinary reviews. RNA* **5**, 637-646 (2014).

1133 32. Ahn, E.Y. et al. SON controls cell-cycle progression by coordinated regulation of RNA
1134 splicing. *Mol Cell* **42**, 185-98 (2011).

1135 33. Kim, J.-H. et al. SON drives oncogenic RNA splicing in glioblastoma by regulating
1136 PTBP1/PTBP2 switching and RBFOX2 activity. *Nature Communications* **12**, 5551
1137 (2021).

1138 34. Li, H.-D., Funk, C.C. & Price, N.D. iREAD: a tool for intron retention detection from RNA-
1139 seq data. *BMC Genomics* **21**, 128 (2020).

1140 35. Sureau, A., Gattoni, R., Dooghe, Y., Stévenin, J. & Soret, J. SC35 autoregulates its
1141 expression by promoting splicing events that destabilize its mRNAs. *Embo j* **20**, 1785-96
1142 (2001).

1143 36. Ding, F., Su, C.J., Edmonds, K.K., Liang, G. & Elowitz, M.B. Dynamics and functional
1144 roles of splicing factor autoregulation. *Cell Rep* **39**, 110985 (2022).

1145 37. Grandjean, J.M.D. et al. Pharmacologic IRE1/XBP1s activation confers targeted ER
1146 proteostasis reprogramming. *Nat Chem Biol* **16**, 1052-1061 (2020).

1147 38. Madhavan, A. et al. Pharmacologic IRE1/XBP1s activation promotes systemic adaptive
1148 remodeling in obesity. *Nature Communications* **13**, 608 (2022).

1149 39. Grandjean, J.M.D. & Wiseman, R.L. Small molecule strategies to harness the unfolded
1150 protein response: where do we go from here? *Journal of Biological Chemistry* **295**,
1151 15692-15711 (2020).

1152 40. Schor, I.E. et al. Perturbation of chromatin structure globally affects localization and
1153 recruitment of splicing factors. *PloS one* **7**, e48084 (2012).

1154 41. Subramanian, A. et al. Gene set enrichment analysis: A knowledge-based approach for
1155 interpreting genome-wide expression profiles. *Proceedings of the National Academy of*
1156 *Sciences* **102**, 15545-15550 (2005).

1157 42. Molina, D.M. et al. Monitoring Drug Target Engagement in Cells and Tissues Using the
1158 Cellular Thermal Shift Assay. *Science* **341**, 84-87 (2013).

1159 43. Jafari, R. et al. The cellular thermal shift assay for evaluating drug target interactions in
1160 cells. *Nature Protocols* **9**, 2100-2122 (2014).

1161 44. Ilik, İ.A. et al. SON and SRRM2 are essential for nuclear speckle formation. *eLife* **9**,
1162 e60579 (2020).

1163 45. Fei, J. et al. Quantitative analysis of multilayer organization of proteins and RNA in
1164 nuclear speckles at super resolution. *Journal of Cell Science* **130**, 4180-4192 (2017).

1165 46. Sharma, A., Takata, H., Shibahara, K., Bubulya, A. & Bubulya, P.A. Son is essential for
1166 nuclear speckle organization and cell cycle progression. *Mol Biol Cell* **21**, 650-63 (2010).

1167 47. Liao, S.E. & Regev, O. Splicing at the phase-separated nuclear speckle interface: a
1168 model. *Nucleic Acids Res* **49**, 636-645 (2021).

1169 48. Xu, S. et al. SRRM2 organizes splicing condensates to regulate alternative splicing.
1170 *Nucleic Acids Res* **50**, 8599-8614 (2022).

1171 49. Gouveia, B. et al. Capillary forces generated by biomolecular condensates. *Nature* **609**,
1172 255-264 (2022).

1173 50. Sabari, B.R. et al. Coactivator condensation at super-enhancers links phase separation
1174 and gene control. *Science* **361**, eaar3958 (2018).

1175 51. Chen, Z. et al. Screening membraneless organelle participants with machine-learning
1176 models that integrate multimodal features. *Proceedings of the National Academy of*
1177 *Sciences* **119**, e2115369119 (2022).

1178 52. Romero, Obradovic & Dunker, K. Sequence Data Analysis for Long Disordered Regions
1179 Prediction in the Calcineurin Family. *Genome Inform Ser Workshop Genome Inform* **8**,
1180 110-124 (1997).

1181 53. Walsh, I., Martin, A.J.M., Di Domenico, T. & Tosatto, S.C.E. ESpritz: accurate and fast
1182 prediction of protein disorder. *Bioinformatics* **28**, 503-509 (2011).

1183 54. Santos, J., Calero, N., Trujillo-Cayado, L.A., Garcia, M.C. & Muñoz, J. Assessing
1184 differences between Ostwald ripening and coalescence by rheology, laser diffraction and
1185 multiple light scattering. *Colloids and Surfaces B: Biointerfaces* **159**, 405-411 (2017).

1186 55. Riback, J.A. et al. Viscoelasticity and advective flow of RNA underlies nucleolar form and
1187 function. *Molecular Cell* **83**, 3095-3107.e9 (2023).

1188 56. Pancholi, A. et al. RNA polymerase II clusters form in line with liquid phase wetting of
1189 chromatin. *bioRxiv*, 2021.02.03.429626 (2021).

1190 57. Liu, X. et al. Time-dependent effect of 1,6-hexanediol on biomolecular condensates and
1191 3D chromatin organization. *Genome Biology* **22**, 230 (2021).

1192 58. Liu, J. et al. A role for the P-body component GW182 in microRNA function. *Nat Cell Biol*
1193 **7**, 1261-6 (2005).

1194 59. Ravi, V., Jain, A., Mishra, S. & Sundaresan, N.R. Measuring Protein Synthesis in
1195 Cultured Cells and Mouse Tissues Using the Non-radioactive SUnSET Assay. *Curr*
1196 *Protoc Mol Biol* **133**, e127 (2020).

1197 60. Pakos-Zebrucka, K. et al. The integrated stress response. *EMBO Rep* **17**, 1374-1395
1198 (2016).

1199 61. Mauvezin, C. & Neufeld, T.P. Bafilomycin A1 disrupts autophagic flux by inhibiting both
1200 V-ATPase-dependent acidification and Ca-P60A/SERCA-dependent autophagosome-
1201 lysosome fusion. *Autophagy* **11**, 1437-8 (2015).

1202 62. Bayer, T.A. Proteinopathies, a core concept for understanding and ultimately treating
1203 degenerative disorders? *Eur Neuropsychopharmacol* **25**, 713-24 (2015).

1204 63. Hartong, D.T., Berson, E.L. & Dryja, T.P. Retinitis pigmentosa. *Lancet* **368**, 1795-809
1205 (2006).

1206 64. Lee, E.-J. et al. ATF6 is required for efficient rhodopsin clearance and retinal
1207 homeostasis in the P23H rho retinitis pigmentosa mouse model. *Scientific Reports* **11**,
1208 16356 (2021).

1209 65. Vats, A. et al. Nonretinoid chaperones improve rhodopsin homeostasis in a mouse
1210 model of retinitis pigmentosa. *JCI Insight* **7**(2022).

1211 66. Chiang, W.-C. et al. Robust Endoplasmic Reticulum-Associated Degradation of
1212 Rhodopsin Precedes Retinal Degeneration. *Molecular Neurobiology* **52**, 679-695 (2015).

1213 67. Chiang, W.-C., Hiramatsu, N., Messah, C., Kroeger, H. & Lin, J.H. Selective Activation of
1214 ATF6 and PERK Endoplasmic Reticulum Stress Signaling Pathways Prevent Mutant
1215 Rhodopsin Accumulation. *Investigative Ophthalmology & Visual Science* **53**, 7159-7166
1216 (2012).

1217 68. Lobanova, E.S. et al. Increased proteasomal activity supports photoreceptor survival in
1218 inherited retinal degeneration. *Nat Commun* **9**, 1738 (2018).

1219 69. Liu, X. et al. Pharmacological clearance of misfolded rhodopsin for the treatment of
1220 RHO-associated retinitis pigmentosa. *The FASEB Journal* **34**, 10146-10167 (2020).

1221 70. Lee, M.J., Lee, J.H. & Rubinsztein, D.C. Tau degradation: The ubiquitin–proteasome
1222 system versus the autophagy-lysosome system. *Progress in Neurobiology* **105**, 49-59
1223 (2013).

1224 71. Limanaqi, F. et al. Promiscuous Roles of Autophagy and Proteasome in
1225 Neurodegenerative Proteinopathies. *Int J Mol Sci* **21**(2020).

1226 72. Samelson, A.J. et al. CRISPR screens in iPSC-derived neurons reveal principles of tau
1227 proteostasis. *bioRxiv*, 2023.06.16.545386 (2023).

1228 73. Bravo, C.P. et al. Human iPSC 4R tauopathy model uncovers modifiers of tau
1229 propagation. *bioRxiv*, 2023.06.19.544278 (2023).

1230 74. Bugiani, O. et al. Frontotemporal dementia and corticobasal degeneration in a family
1231 with a P301S mutation in tau. *Journal of neuropathology and experimental neurology* **58**,
1232 667-677 (1999).

1233 75. Chen, X. et al. Promoting tau secretion and propagation by hyperactive p300/CBP via
1234 autophagy-lysosomal pathway in tauopathy. *Molecular Neurodegeneration* **15**, 2 (2020).

1235 76. Triastuti, E. et al. Pharmacological inhibition of Hippo pathway, with the novel kinase
1236 inhibitor XMU-MP-1, protects the heart against adverse effects during pressure overload.
1237 *Br J Pharmacol* **176**, 3956-3971 (2019).

1238 77. Hao, X. et al. XMU-MP-1 attenuates osteoarthritis via inhibiting cartilage degradation
1239 and chondrocyte apoptosis. *Frontiers in Bioengineering and Biotechnology* **10**(2022).

1240 78. Kastan, N. et al. Small-molecule inhibition of Lats kinases may promote Yap-dependent
1241 proliferation in postmitotic mammalian tissues. *Nature Communications* **12**, 3100 (2021).

1242 79. Arno, G. et al. Mutations in REEP6 Cause Autosomal-Recessive Retinitis Pigmentosa.
1243 *Am J Hum Genet* **99**, 1305-1315 (2016).

1244 80. Wittmann, C.W. et al. Tauopathy in Drosophila: Neurodegeneration Without
1245 Neurofibrillary Tangles. *Science* **293**, 711-714 (2001).

1246 81. Berger, C., Renner, S., Lüer, K. & Technau, G.M. The commonly used marker ELAV is
1247 transiently expressed in neuroblasts and glial cells in the Drosophila embryonic CNS.
1248 *Developmental Dynamics* **236**, 3562-3568 (2007).

1249 82. Hirabayashi, S., Baranski, T.J. & Cagan, R.L. Transformed Drosophila cells evade diet-
1250 mediated insulin resistance through wingless signaling. *Cell* **154**, 664-75 (2013).

1251 83. Wang, L. et al. JNK modifies neuronal metabolism to promote proteostasis and
1252 longevity. *Aging Cell* **18**, e12849 (2019).

1253 84. Xu, M. et al. A systematic integrated analysis of brain expression profiles reveals YAP1
1254 and other prioritized hub genes as important upstream regulators in Alzheimer's disease.
1255 *Alzheimers Dement* **14**, 215-229 (2018).

1256 85. Mathys, H. et al. Single-cell transcriptomic analysis of Alzheimer’s disease. *Nature* **570**,
1257 332-337 (2019).

1258 86. Wang, C. et al. Scalable Production of iPSC-Derived Human Neurons to Identify Tau-
1259 Lowering Compounds by High-Content Screening. *Stem Cell Reports* **9**, 1221-1233
1260 (2017).

1261 87. Ishii, I., Harada, Y. & Kasahara, T. Reprofiling a classical anthelmintic, pyrvinium
1262 pamoate, as an anti-cancer drug targeting mitochondrial respiration. *Frontiers in*
1263 *Oncology* **2**(2012).

1264 88. Masud, S.N. et al. Chemical genomics with pyrvinium identifies C1orf115 as a regulator
1265 of drug efflux. *Nature Chemical Biology* **18**, 1370-1379 (2022).

1266 89. Kurmi, K. et al. Metabolic modulation of mitochondrial mass during CD4+ T cell
1267 activation. *Cell Chemical Biology* (2023).

1268 90. Melber, A. & Haynes, C.M. UPRmt regulation and output: a stress response mediated by
1269 mitochondrial-nuclear communication. *Cell Research* **28**, 281-295 (2018).

1270 91. Mick, E. et al. Distinct mitochondrial defects trigger the integrated stress response
1271 depending on the metabolic state of the cell. *eLife* **9**, e49178 (2020).

1272 92. Lester, E. et al. Tau aggregates are RNA-protein assemblies that mislocalize multiple
1273 nuclear speckle components. *Neuron* **109**, 1675-1691 e9 (2021).

1274 93. McMillan, P.J. et al. Pathological tau drives ectopic nuclear speckle scaffold protein
1275 SRRM2 accumulation in neuron cytoplasm in Alzheimer's disease. *Acta*
1276 *Neuropathologica Communications* **9**, 117 (2021).

1277 94. Tracy, T.E. et al. Tau interactome maps synaptic and mitochondrial processes
1278 associated with neurodegeneration. *Cell* **185**, 712-728.e14 (2022).

1279 95. Hsieh, Y.C. et al. Tau-Mediated Disruption of the Spliceosome Triggers Cryptic RNA
1280 Splicing and Neurodegeneration in Alzheimer's Disease. *Cell Rep* **29**, 301-316 e10
1281 (2019).

1282 96. Mordes, D. et al. Pre-mRNA splicing and retinitis pigmentosa. *Mol Vis* **12**, 1259-71
1283 (2006).

1284 97. Wheeler, R.J. Therapeutics-how to treat phase separation-associated diseases. *Emerg*
1285 *Top Life Sci* **4**, 307-318 (2020).

1286 98. Conti, B.A. & Oppikofer, M. Biomolecular condensates: new opportunities for drug
1287 discovery and RNA therapeutics. *Trends in Pharmacological Sciences* **43**, 820-837
1288 (2022).

1289 99. Kilgore, H.R. et al. Distinct chemical environments in biomolecular condensates. *Nature*
1290 *Chemical Biology* (2023).

1291 100. Schultz, C.W. & Nevler, A. Pyrvinium Pamoate: Past, Present, and Future as an Anti-
1292 Cancer Drug. *Biomedicines* **10**, 3249 (2022).

1293 101. Jawerth, L.M. et al. Salt-Dependent Rheology and Surface Tension of Protein
1294 Condensates Using Optical Traps. *Physical Review Letters* **121**, 258101 (2018).

1295 102. Spruijt, E., Sprakel, J., Cohen Stuart, M.A. & van der Gucht, J. Interfacial tension
1296 between a complex coacervate phase and its coexisting aqueous phase. *Soft Matter* **6**,
1297 172-178 (2010).

1298 103. Cai, D., Sukenik, S., Feliciano, D., Gruebele, M. & Lippincott-Schwartz, J. Phase
1299 Separation of YAP Reprograms Cells for Long-term YAP Target Gene Expression.
1300 *bioRxiv*, 438416 (2018).

1301 104. Yang, S. et al. Bip-Yorkie interaction determines oncogenic and tumor-suppressive roles
1302 of Ire1/Xbp1s activation. *Proceedings of the National Academy of Sciences* **119**,
1303 e2202133119 (2022).

1304 105. Rivera-Reyes, A. et al. YAP1 enhances NF-κB-dependent and independent effects on
1305 clock-mediated unfolded protein responses and autophagy in sarcoma. *Cell Death Dis* **9**,
1306 1108 (2018).

1307 106. Min, Y. et al. Cross species systems biology discovers glial DDR2, STOM, and KANK2
1308 as therapeutic targets in progressive supranuclear palsy. *Nature Communications* **14**,
1309 6801 (2023).

1310 107. Vallazza-Deschamps, G. et al. Excessive activation of cyclic nucleotide-gated channels
1311 contributes to neuronal degeneration of photoreceptors. *Eur J Neurosci* **22**, 1013-22
1312 (2005).

1313 108. Vats, A. et al. Nonretinoid chaperones improve rhodopsin homeostasis in a mouse
1314 model of retinitis pigmentosa. *JCI Insight* **7**(2022).

1315 109. Pi, S. et al. Retinal capillary oximetry with visible light optical coherence tomography.
1316 *Proc Natl Acad Sci U S A* **117**, 11658-11666 (2020).

1317 110. Fanning, S., Selkoe, D. & Dettmer, U. Parkinson's disease: proteinopathy or lipidopathy?
1318 *NPJ Parkinsons Dis* **6**, 3 (2020).

1319 111. Stirling, D.R. et al. CellProfiler 4: improvements in speed, utility and usability. *BMC*
1320 *bioinformatics* **22**, 1-11 (2021).

1321 112. Schneider, C.A., Rasband, W.S. & Eliceiri, K.W. NIH Image to ImageJ: 25 years of
1322 image analysis. *Nature methods* **9**, 671-675 (2012).

1323 113. Zhu, B. et al. Coactivator-Dependent Oscillation of Chromatin Accessibility Dictates
1324 Circadian Gene Amplitude via REV-ERB Loading. *Mol Cell* **60**, 769-783 (2015).

1325 114. Zhu, B. et al. A Cell-Autonomous Mammalian 12 hr Clock Coordinates Metabolic and
1326 Stress Rhythms. *Cell Metabolism* **25**, 1305-1319.e9 (2017).

1327 115. Bolger, A.M., Lohse, M. & Usadel, B. Trimmomatic: a flexible trimmer for Illumina
1328 sequence data. *Bioinformatics* **30**, 2114-20 (2014).

1329 116. Kim, D., Langmead, B. & Salzberg, S.L. HISAT: a fast spliced aligner with low memory
1330 requirements. *Nat Methods* **12**, 357-60 (2015).

1331 117. Quinlan, A.R. & Hall, I.M. BEDTools: a flexible suite of utilities for comparing genomic
1332 features. *Bioinformatics* **26**, 841-2 (2010).

1333 118. Blankenberg, D. et al. Galaxy: A Web-Based Genome Analysis Tool for
1334 Experimentalists. *Current Protocols in Molecular Biology* **89**, 19.10.1-19.10.21 (2010).

1335 119. Krueger, F. Trim Galore. Vol. 2022 (2021).

1336 120. Patro, R., Duggal, G., Love, M.I., Irizarry, R.A. & Kingsford, C. Salmon provides fast and
1337 bias-aware quantification of transcript expression. *Nature methods* **14**, 417-419 (2017).

1338 121. Guo, W. et al. 3D RNA-seq: a powerful and flexible tool for rapid and accurate
1339 differential expression and alternative splicing analysis of RNA-seq data for biologists.
1340 *RNA biology* **18**, 1574-1587 (2021).

1341 122. Langmead, B. & Salzberg, S.L. Fast gapped-read alignment with Bowtie 2. *Nat Methods*
1342 **9**, 357-9 (2012).

1343 123. Li, B. & Dewey, C.N. RSEM: accurate transcript quantification from RNA-Seq data with
1344 or without a reference genome. *BMC Bioinformatics* **12**, 323 (2011).

1345 124. Robinson, M.D., McCarthy, D.J. & Smyth, G.K. edgeR: a Bioconductor package for
1346 differential expression analysis of digital gene expression data. *Bioinformatics* **26**, 139-
1347 40 (2010).

1348 125. Huang da, W., Sherman, B.T. & Lempicki, R.A. Systematic and integrative analysis of
1349 large gene lists using DAVID bioinformatics resources. *Nat Protoc* **4**, 44-57 (2009).

1350 126. He, H.H. et al. Nucleosome dynamics define transcriptional enhancers. *Nature Genetics*
1351 **42**, 343-347 (2010).

1352 127. Zhang, M.J., Pisco, A.O., Darmanis, S. & Zou, J. Mouse aging cell atlas analysis reveals
1353 global and cell type-specific aging signatures. *Elife* **10**(2021).

1354 128. A single-cell transcriptomic atlas characterizes ageing tissues in the mouse. *Nature* **583**,
1355 590-595 (2020).

1356 129. Jiang, J., Wang, C., Qi, R., Fu, H. & Ma, Q. scREAD: A Single-Cell RNA-Seq Database
1357 for Alzheimer's Disease. *iScience* **23**, 101769 (2020).

1358

1359

1360

1361

1362 **Fig. legends**

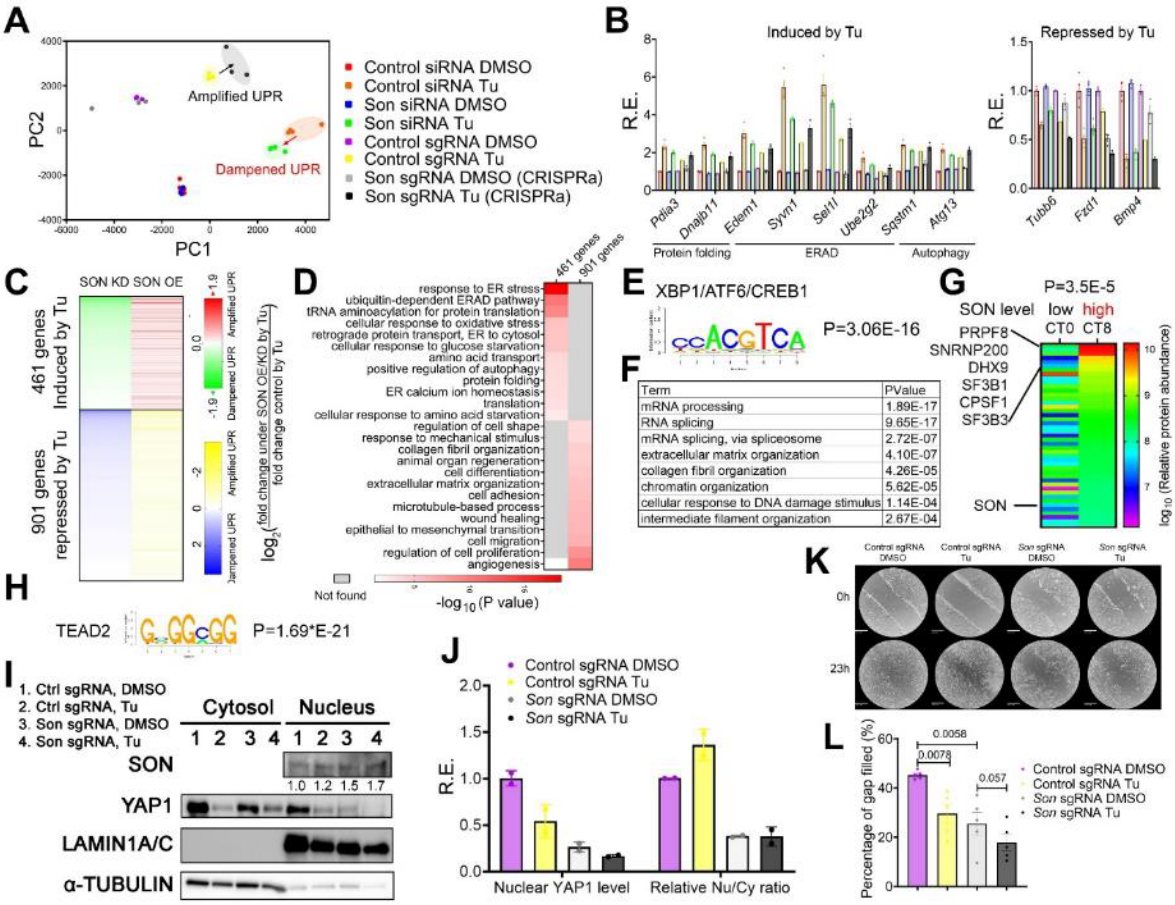

Fig. 1. Genetic rejuvenation of nuclear speckle transcriptionally reprograms global proteostasis and YAP1 signaling in an opposing manner. (**a**) PCA analysis of global transcriptional response to Tu in the presence of SON OE (via CRISPRa) or KD (via siRNA). (**b**) Relative expression (R.E.) of representative proteostasis genes (left) and YAP1 target genes (right) in response to Tu in the presence of SON OE/KD (n=4 for SON KD, and n=3 for SON OE). (**c**) Heat map of relative fold change of gene expression by Tu in SON OE/KD cells compared to control cells. Only those genes with at least 1.4-fold induction by Tu ($\log_2 > 0.5$) with a p value smaller than 0.05 in control condition are included. Among these genes are 461 genes whose induction by Tu are further amplified by SON OE (induced more) and dampened (induced less) *by* SON KD; and 901 genes whose repression by Tu are further amplified by *Son* OE (repressed further) and dampened (repressed less) by SON KD. (**d**) GO analysis of those 461 and 901 genes showing enriched KEGG pathways. (**e**) Enriched XBP1s binding motif ACGTCA on the promoters of 461 genes. (**f**) Top enriched GO terms for top 500 most abundant proteins that are detected in hepatic XBP1s interactome at CT8, as previously reported [10]. (**g**) Heatmap showing relative abundance of 45 proteins involved in mRNA splicing and processing within the XBP1s interactome at CT0 and CT8, respectively (p value of 3.5E-5 calculated by paired t-test indicating reduced abundance at CT0). (**h**) Enriched TEAD2 binding motif GGCGG on the promoters of 901 genes. Western blot (**i**) and quantification (**j**) of nuclear and cytosolic level of YAP1 in control and SON OE cells in response to Tu (n=2). Scratch assay with representative images (**k**) and quantification (**l**) of cell migration rate in control and SON OE cells in response to Tu (n=5). All data mean ± Standard error of the mean (S.E.M.).

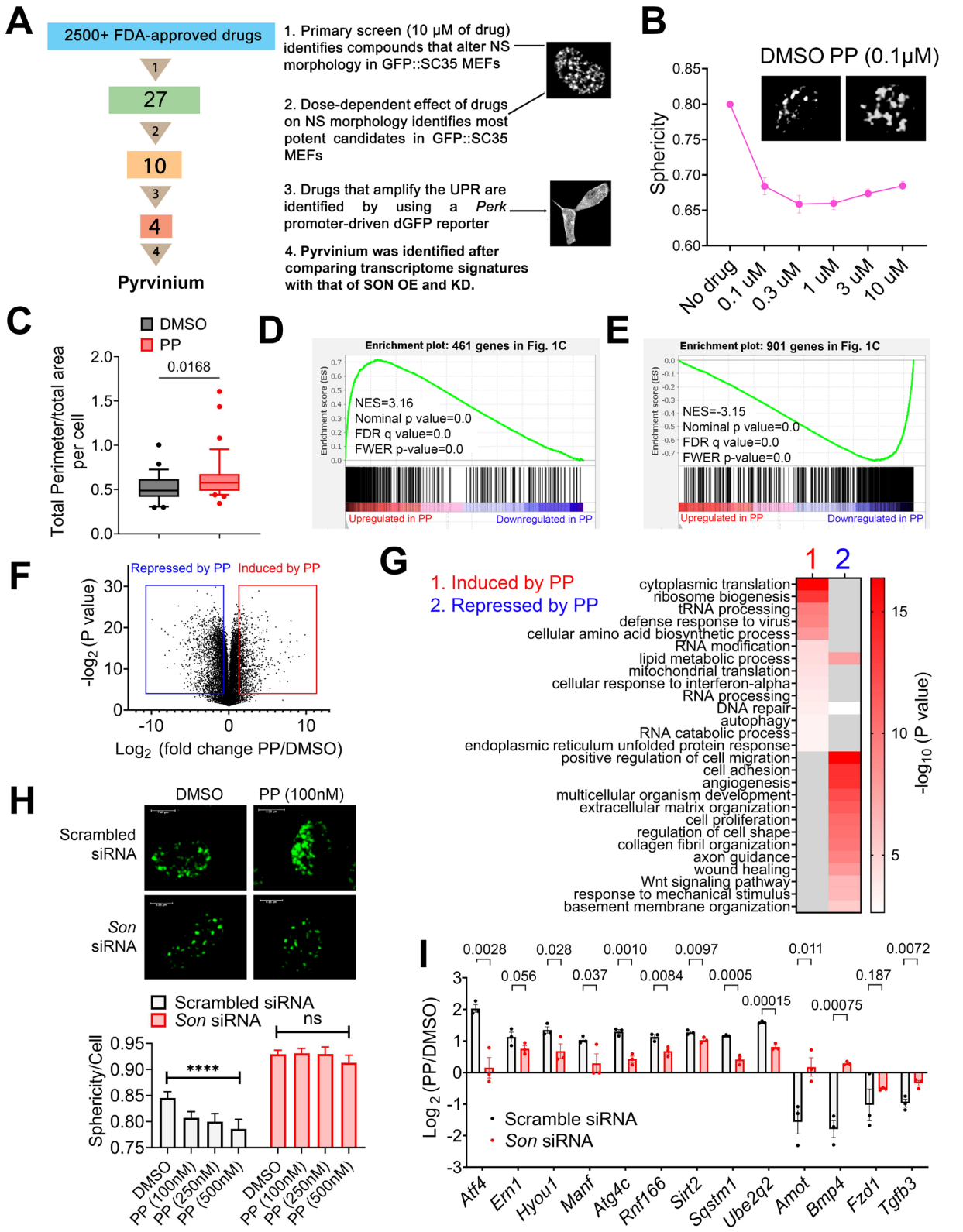

Fig. 2. HTS identifies pyrvinium as an SON-dependent nuclear speckle rejuvenator. (**a**) Workflow detailing our initial drug screen and subsequent steps to identify compounds that affect the nuclear speckle morphology in a dose-dependent manner and amplifies the UPR. (**b**) Dose-

dependent effect on nuclear speckles morphology by PP, with a representative image of nuclear speckle under 1μM of PP (n=10~16). (**c**) Quantification of total area-normalized perimeter of nuclear speckles in control and 1μM PP condition per cell (n=26 for DMSO and n=35 for PP). (**d**) GSEA analysis showing a similar transcriptome signature between PP-upregulated genes and 461 genes further amplified by SON OE during ER stress. (**e**) GSEA analysis showing a similar transcriptome signature between PP-downregulated genes and 901 genes further blunted by SON OE during ER stress. (**f**) Volcano plot showing fold change by PP versus log transformed p values. Genes induced or repressed by at least 1.41-fold with a p value smaller than 0.05 are boxed. (**g**) GO analysis of differentially expressed genes by PP. (**h**) Representative images and quantification of sphericity of GFP signal from GFP::SRSF2 MEFs with scrambled or Son siRNA treated with DMSO or increasing concentration of PP for 24 hours. (**i**) Log_2 normalized fold change in response to PP treatment (0.3 μm) for 24 hours in control and SON KD MEFs with p values shown for one tailed t-test (n=3). All data mean ± S.E.M.

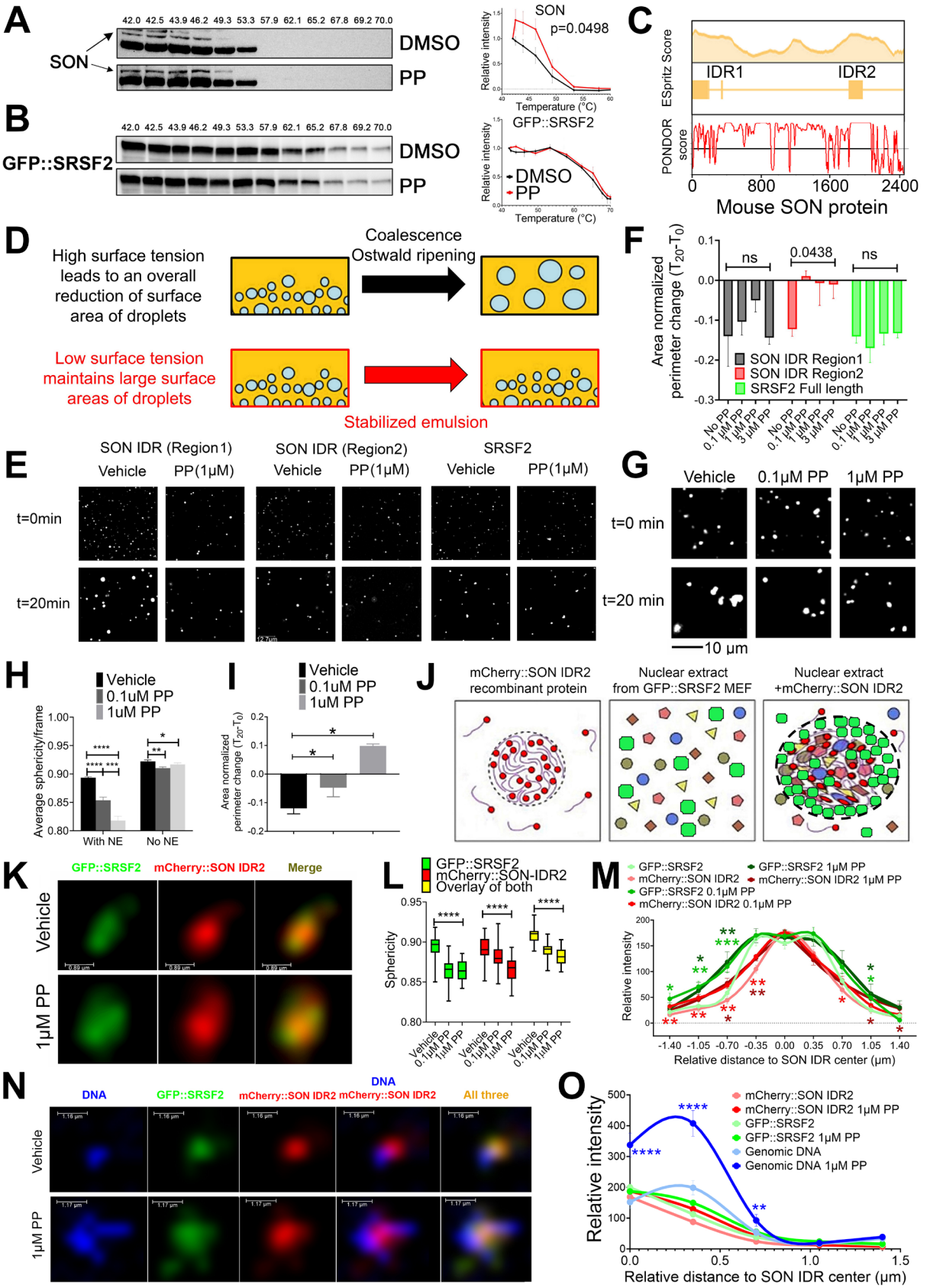
A
SON
DMSO
PP
B
GFP::SRSF2
DMSO
PP
SON
p=0.0498
GFP::SRSF2
Relative intensity
Temperature (°C)
C
EScritz Score
PONDOR score
IDR1
IDR2
Mouse SON protein
D
High surface tension leads to an overall reduction of surface area of droplets
Coalescence
Ostwald ripening
Low surface tension maintains large surface areas of droplets
Stabilized emulsion
F
Area normalized perimeter change (T20-T0)
ns
0.0438
ns
SON IDR Region1
SON IDR Region2
SRSF2 Full length
No PP
0.1 μM PP
1 μM PP
3 μM PP
E
SON IDR (Region1)
SON IDR (Region2)
SRSF2
Vehicle
PP(1μM)
t=0min
t=20min
G
Vehicle
0.1μM PP
1μM PP
t=0 min
t=20 min
10 μm
H
Vehicle
0.1uM PP
1uM PP
Average sphericity/frame
With NE
No NE
I
Vehicle
0.1uM PP
1uM PP
Area normalized perimeter change (T20-T0)
J
mCherry::SON IDR2 recombinant protein
Nuclear extract from GFP::SRSF2 MEF
Nuclear extract +mCherry::SON IDR2
K
GFP::SRSF2
mCherry::SON IDR2
Merge
Vehicle
1μM PP
L
GFP::SRSF2
mCherry::SON-IDR2
Overlay of both
Sphericity
Vehicle
0.1μM PP
1μM PP
M
GFP::SRSF2
mCherry::SON IDR2
GFP::SRSF2 0.1μM PP
mCherry::SON IDR2 0.1μM PP
GFP::SRSF2 1μM PP
mCherry::SON IDR2 1μM PP
Relative intensity
Relative distance to SON IDR center (μm)
N
DNA
GFP::SRSF2
mCherry::SON IDR2
DNA
mCherry::SON IDR2
All three
Vehicle
1μM PP
O
mCherry::SON IDR2
mCherry::SON IDR2 1μM PP
GFP::SRSF2
GFP::SRSF2 1μM PP
Genomic DNA
Genomic DNA 1μM PP
Relative intensity
Relative distance to SON IDR center (μm)

1423

1424 **Fig. 3. PP targets SON to reduce the interfacial tension of nuclear speckles.** CETSA of SON
1425 (**a**) and GFP::SRSF2 (**b**) with 3μM PP. Both representative blot and quantification from
1426 independent replicates are shown. P value is calculated by mixed-effects analysis (SON: n=6 for
1427 DMSO and n=5 for PP; GFP::SRSF2: n=3 for both DMSO and PP). (**c**) Computational prediction
1428 of IDR in mouse SON. (**d**) Diagram illustrating how surface tension influences droplets
1429 coalescence kinetics. (**e, f**) Representative images of droplet formation assay with different
1430 recombinant proteins (**e**) and quantification (**f**) of area-normalized perimeter changes in the time
1431 span of 20 minutes with 125mM NaCl (n=2~3). (**g-i**) Representative images of droplet formation
1432 with NE-supplemented SON IDR2 with increasing concentration of PP (**g**) and quantification of
1433 sphericity (n=12 for with NE and n=42 for without NE) (**h**) and area-normalized perimeter changes
1434 (n=2) (**i**) in the time span of 20 minutes. (**j-m**) Diagram of droplet formation assay where SON
1435 IDR2 is expected to compartmentalize splicing factors, including GFP::SRSF2 into the nuclear
1436 speckle-like condensates. GFP::SRSF2 is expected to exhibit a broader spatial distribution than
1437 the SON IDR2 core (**j**). Representative images (**k**) and quantification of sphericity (**l**) and spatial
1438 distribution of mCherry::SON IDR2 and GFP::SRSF2 (**m**). (**n, o**) Mouse genomic DNA was further
1439 added to the solution. Representative images (**n**) and quantification (**o**) of spatial distribution of
1440 mCherry::SON IDR2, GFP::SRSF2 and DNA. All data mean ± S.E.M.

1441

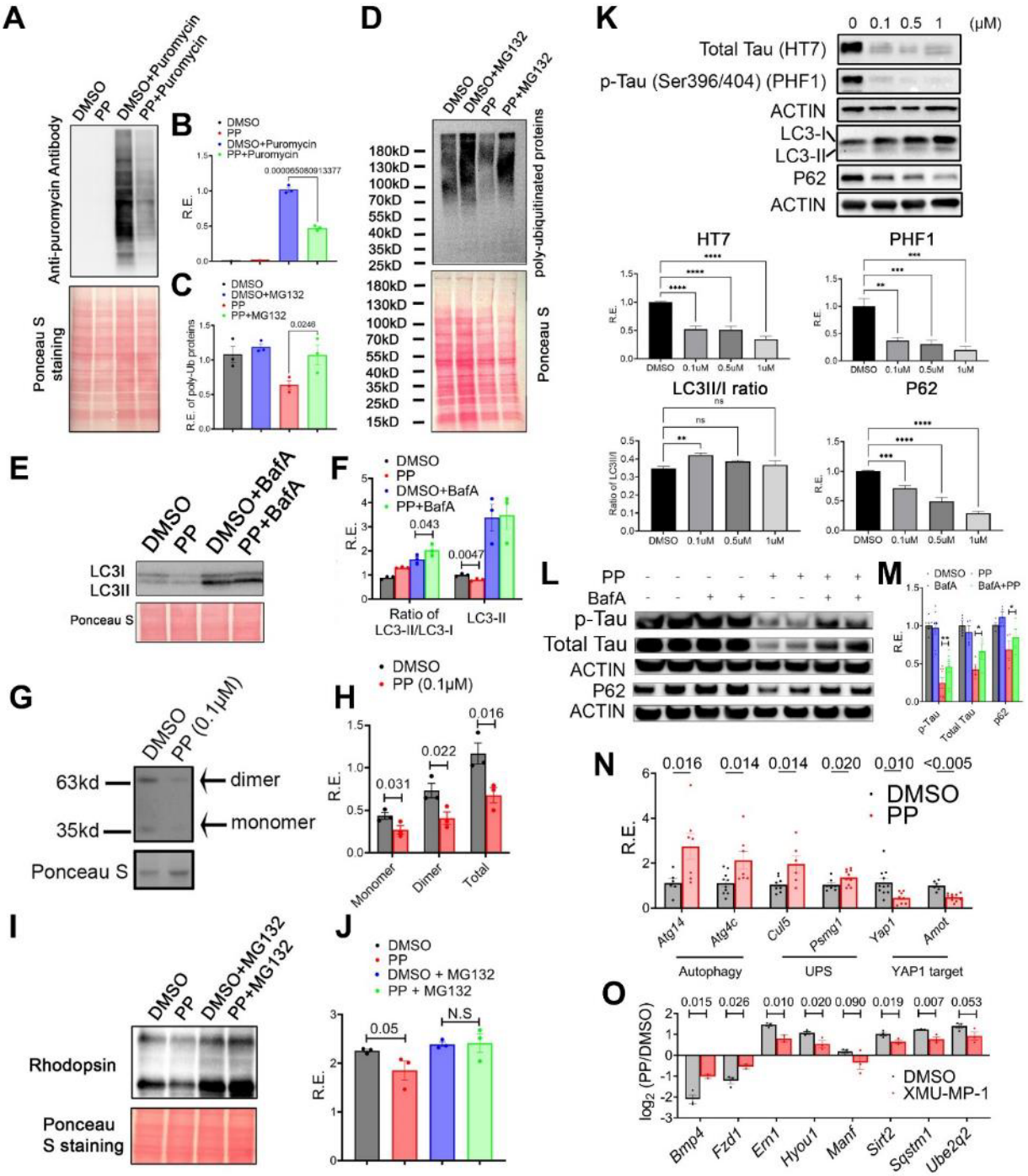

Fig. 4. PP reduces pathological Tau and Rhodopsin level by boosting autophagy and UPS activity. (**A-F**) MEFs were treated with vehicle control or 1μM PP for ~24 hours (22 hours for **E** and **F**) and then co-treated with or without puromycin (10 μg/mL for 30 minutes), MG132 (10μM for 110 minutes) or Baf A (100nM for 22 hours) (n=3 for all samples). Western blot and quantification of puromycin-incorporated proteins (**A, B**), poly-ubiquitinated protein (**C, D**) and LC3II and LC3II/LC3I ratio (**E, F**). (**G-H**) NIH3T3 RHO^{P23H} cells were treated with 0.1μM PP for 24 hours and Western blot (**G**) and quantification (**H**) of RHO^{P23H} level (n=3). (**I, J**) NIH3T3 RHO^{P23H} cells were co-treated with or without MG132 (10μM for 120 minutes). Western blot (**I**) and

1451 quantification (**J**) of RHO^{P23H} level (n=3). (**K**) qPCR of proteostasis and YAP1 target genes in
1452 P301S-expressing primary neurons treated with or without PP (0.1μM) for 12 hours. (**K-M**) Tau
1453 (P301S)-expressing primary neurons were treated with increasing concentration of PP for 24
1454 hours, and western blot and quantification of different proteins (n=4 for HT7, PHF1 and LC3, and
1455 n=6 for P62) (**K**) or treated with 0.1μM PP for 12h hours in the presence or absence of BafA
1456 (50nM) in the last hour and western blot (**L**) and quantification (n=4 for total Tau and P62 and n=8
1457 for p-Tau) (**M**) of different proteins. (**N**) Tau P301S-expressing neurons were treated with DMSO
1458 or 0.1μM PP for 12 hours and qPCR of selective proteostasis and YAP1 target genes (n=6~11).
1459 (**O**) MEFs were treated with DMSO, PP (1μM), XMU-MP-1 (1μM) or XMU-MP-1+PP for 24h hours,
1460 and qPCR of protein quality control and YAP1s output gene expression quantified as log
1461 transformed fold change under DMSO or XMU-MP-1 condition by PP (n=3). All data mean ±
1462 S.E.M.

1463

1464

1465

1466

1467

1468

1469

1470

1471

1472

1473

1474

1475

1476

1477

1478

1479

1480

1481

1482

1483

1484

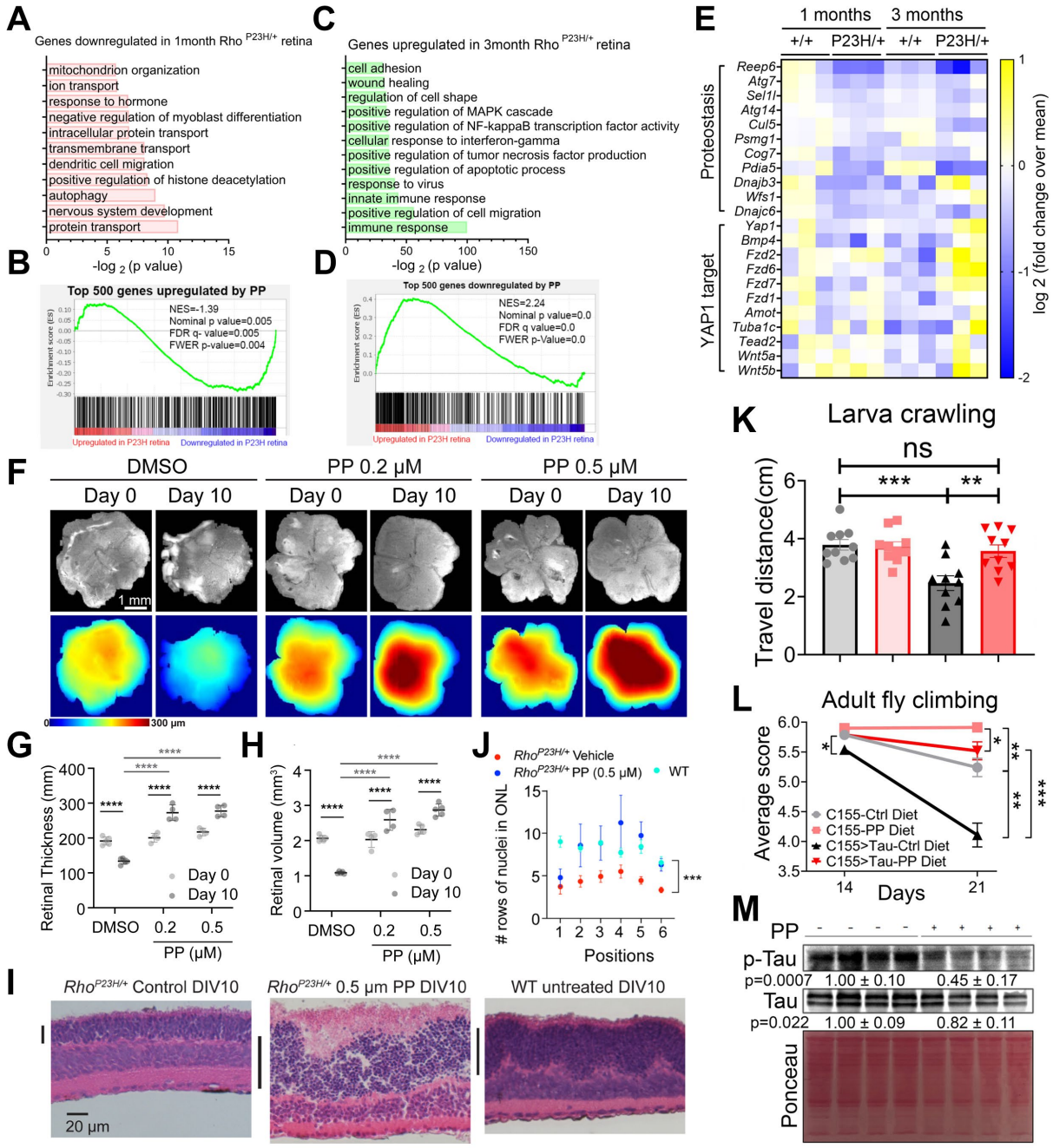

Fig. 5. PP alleviates proteinopathies in preclinical models. (**a-e**) RNA-seq was performed in the retina of 1 and 3 months-old wild-type and Rho $^{P23H/+}$ mice. GO of differentially expressed genes (DEG) (FDR<0.1) (**a, c**) and GSEA comparing these DEG with that of PP (**b, d**). Heatmap of selective genes (**e**). (**f-j**) Retina explants isolated either from *Rho*$^{P23H/+}$ mice P15 and cultured with PP or DMSO vehicle control or from wild-type mice cultured for 10 days *ex vivo*. (**f**) The morphology retinae were imaged and scanned before (Day 0) and after treatment (Day 10) by a webcam (top) and visible light optical coherence tomography (vis-OCT) with tissue thickness shown as a heatmap with a color legend indicating thickness from 0-300 µm (bottom). Scale, 1 mm. (**g**) and (**h**) are bar plots of retinal thickness and volume, respectively, measured from the

1495 vis-OCT scanning data where **** indicates *P<0.0001* by two-way ANOVA and Turkey multiple
1496 comparison. Data: Means ±SDs. N=4-5. (**i**) Representative retinal histology images of the retina
1497 explants cultured for 10 days with black bars showing the outer nuclear layer (ONL). Scale, 20
1498 µm. (**j**) The nuclei count in the outer nuclei layer (ONL) along six horizontal positions at peripheral-
1499 central-peripheral positions across each cross-section in (**i**). Data: Mean ± SD. N=3-4. ***,
1500 P<0.001 by two-way AVOVA comparing $Rho^{P23H/+}$ retinal explants treated with PP vs. vehicle
1501 control. (**k-m**) C155>UAS-hTau1.13 and C155 flies were fed with either standard diet or diet
1502 supplemented with 25µM PP. Quantification of distance travelled from larval crawling assay
1503 (n=10) (**k**), climbing index score from adult fly climbing assay at 14 days and 21 days (n=5) (**l**) of
1504 age. Western blot and quantification of p-Tau (AT8 antibody) and total Tau (DAKO antibody) level
1505 in C155>UAS-hTau1.13 flies fed with control or PP diet (**m**).

1506

1507

1508

1509

1510

1511

1512

1513

1514

1515

1516

1517

1518

1519

1520

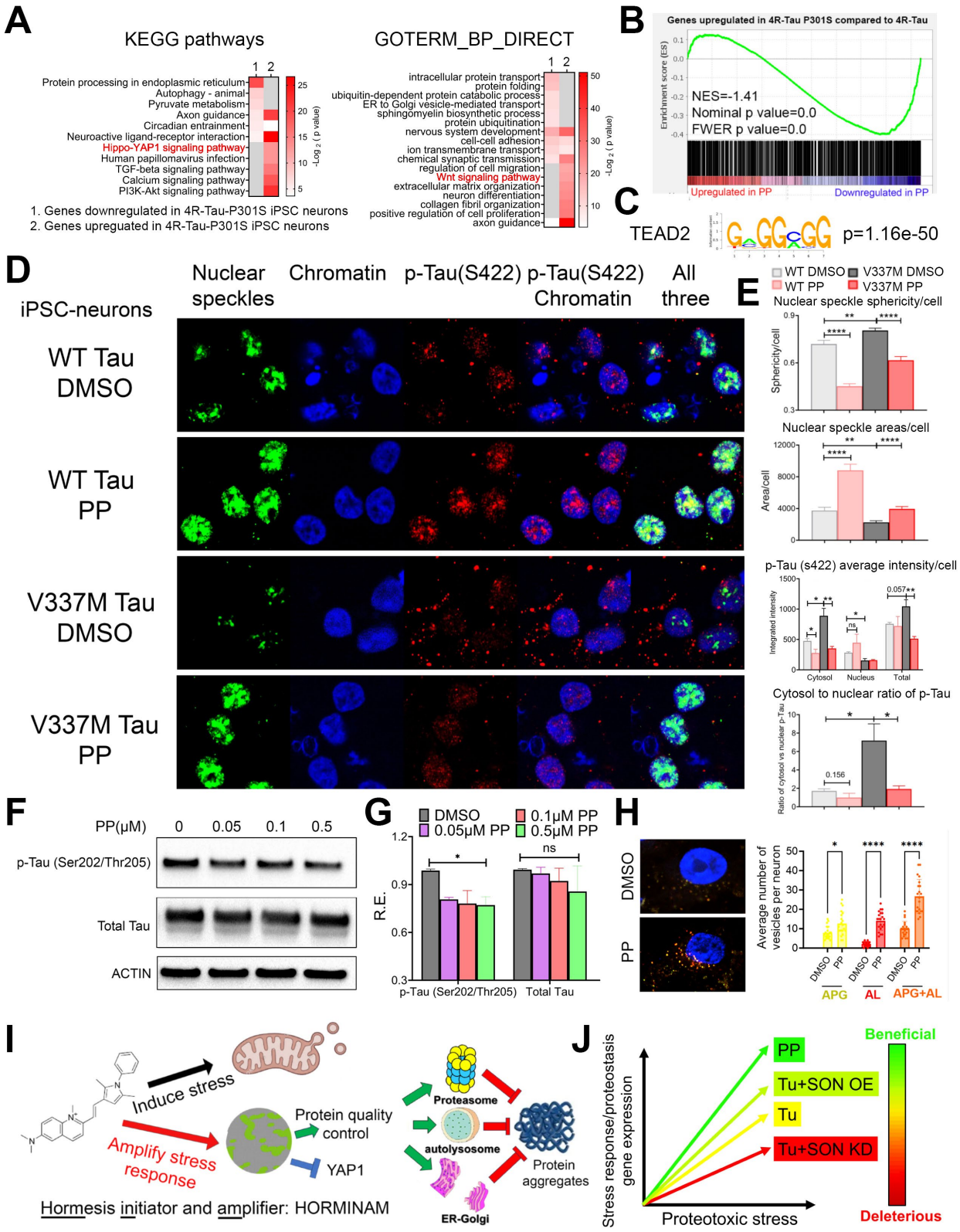

Fig. 6. PP rejuvenates nuclear speckles and alleviates tau burden in human iPSC-neurons expressing mutant Tau. (**a**) GO analysis of up and downregulated genes in 4R-Tau P301S iPSC

1524 neurons reported in [73]. (**b**) GSEA comparing genes upregulated in 4R-Tau P301S iPSC neurons
1525 with those downregulated by PP. (**c**) Motif analysis of promoters of genes upregulated in 4R-Tau
1526 P301S iPSC neurons compared to 4R-Tau (FDR<0.05) revealed top enriched motif of TEAD2.
1527 (**d, e**) Wild-type and V337M Tau-expressing iPSC-neurons were treated with DMSO or PP (10nM)
1528 for 12 hours, and IF against nuclear speckle (Ab11826 against SRRM2), p-Tau (Ser422) and
1529 chromatin (DAPI) were performed. Representative images (**d**) and quantification of nuclear
1530 speckle sphericity and area, intensity of nuclear, cytosol and total level of p-Tau (Ser422) and
1531 ratio of cytosol versus nuclear level of p-Tau (**e**). (**f, g**) V337M Tau-expressing iPSC-neurons were
1532 treated with DMSO or increasing concentrations of PP for 12 hours. Representative western blot
1533 (**f**) and quantification (**g**) of total and p-Tau (Ser202/Thr205) (n=3). (**h**) V337M Tau-expressing
1534 iPSC-neurons were treated with DMSO or 100nM PP for 12 hours, and autophagy flux was
1535 quantified by the autophagy reporter. (**i**) PP is a HORMINAM by inducing stress (via mitochondria)
1536 as well as amplifying the stress response (via SON). (**j**) Diagram showing relationship between
1537 stress and stress response under different conditions. PP can elicit the most robust stress
1538 response relative to stress. Data: Mean ± SEM.

1539

1540

1541

1542

1543

1544

1545

1546

1547

1548

1549

1550

1551

1552

1553

1554

1555

1556

1557

1558

Extended Data Figures.

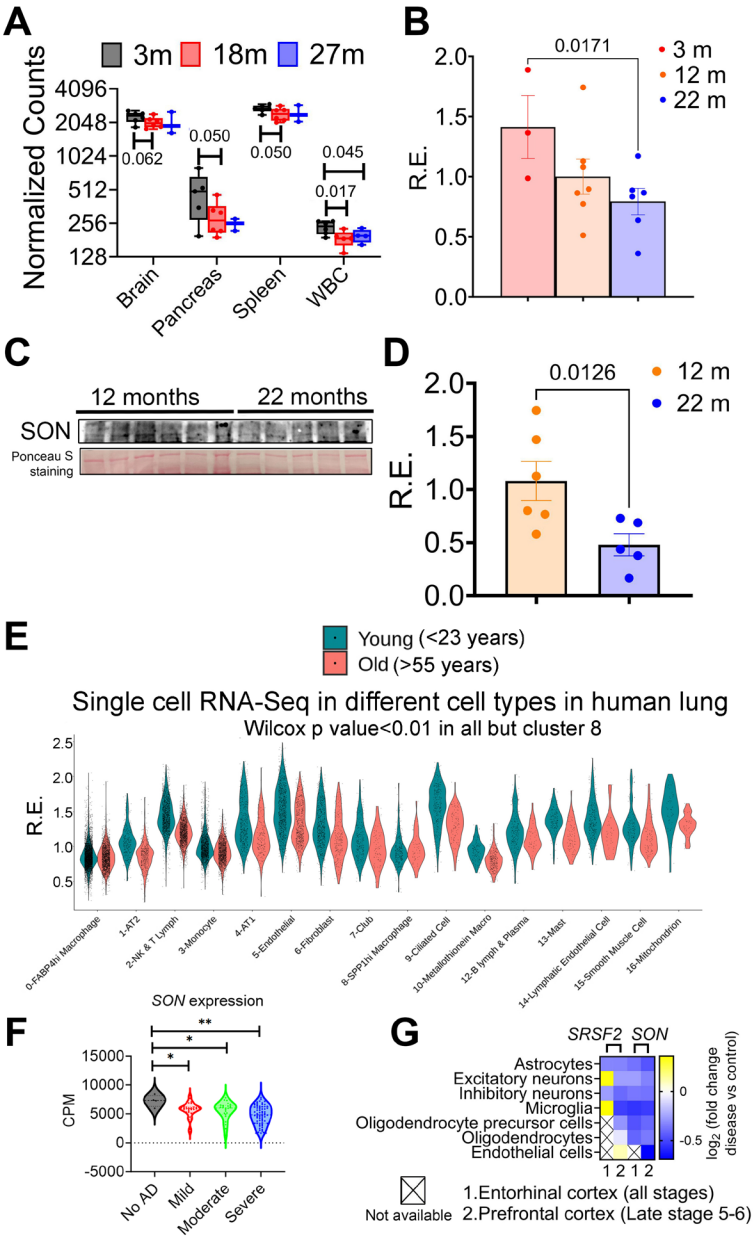

Extended Data Figure 1. SON expression is reduced during aging in mice and humans. (**a**) Normalized counts of *Son* mRNA in different mouse tissues with different ages (WBC; White blood cells) according to Tabula Muris Senis database (n=3~6) [127,128]. (**b**) qPCR of *Son* level in liver of mice with different age (n=3~7). (**c, d**) Western blot (**c**) and quantification (**d**) of SON level in liver of mice with different ages (n=5~6). (**e**) Single cell RNA-seq data of *SON* mRNA level in different cell types in lung tissues of young and aging humans, reported from [20]. (**f**) Expression of *SON* in brains of human AD compiled from RNA-seq data from the AMP-AD consortium. (**g**) Heat map showing relative expression of *SRSF2* and *SON* in different cell types in the cortex of human AD subjects [129]. Blue color indicates lower level in AD subjects compared to controls. Data: Mean ± SEM.

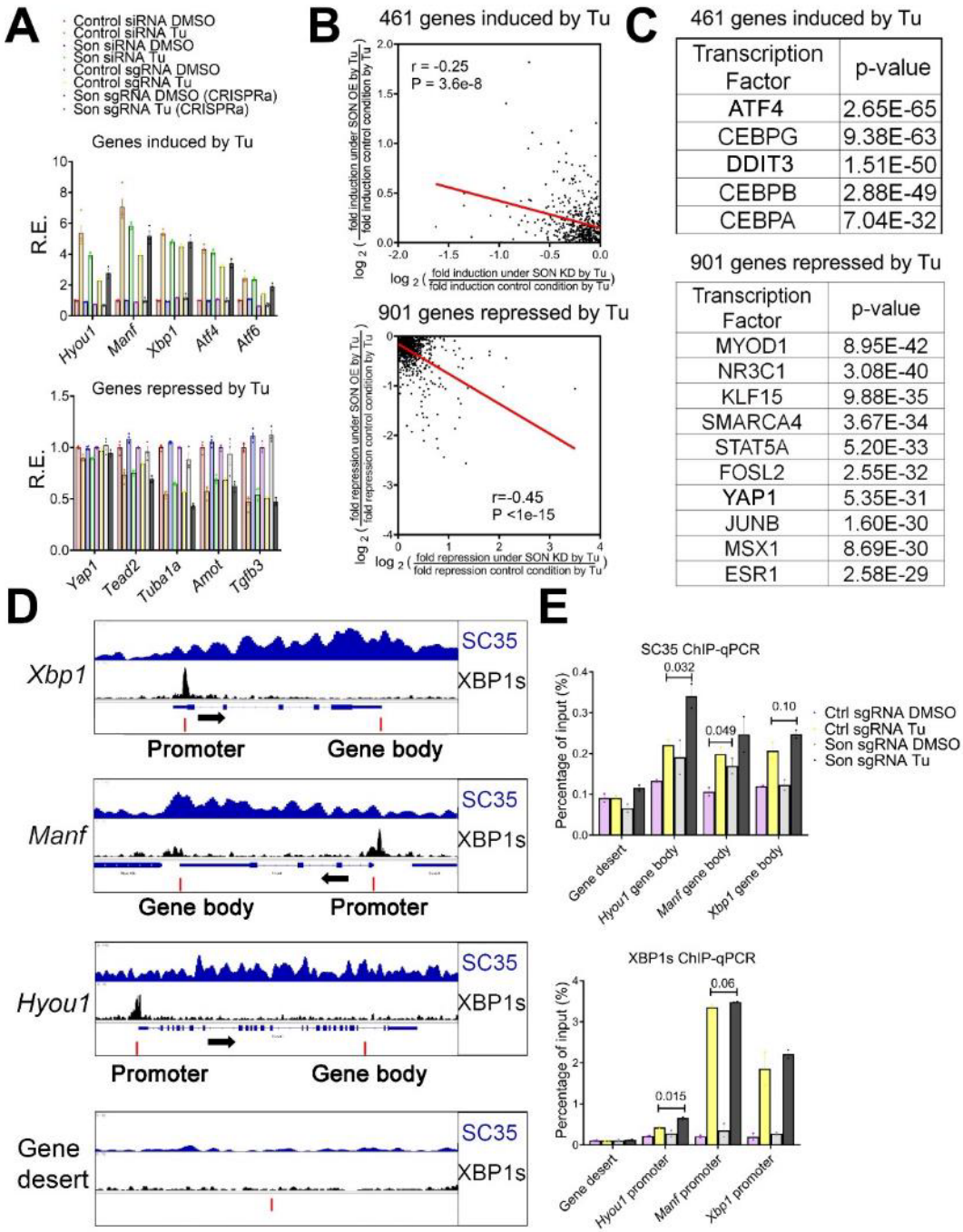

Transcription Factor	p-value
ATF4	2.65E-65
CEBPG	9.38E-63
DDIT3	1.51E-50
CEBPB	2.88E-49
CEBPA	7.04E-32

Transcription Factor	p-value
MYOD1	8.95E-42
NR3C1	3.08E-40
KLF15	9.88E-35
SMARCA4	3.67E-34
STAT5A	5.20E-33
FOSL2	2.55E-32
YAP1	5.35E-31
JUNB	1.60E-30
MSX1	8.69E-30
ESR1	2.58E-29

Extended Data Figure 2. Genetic rejuvenation of nuclear speckle by SON. (**a**) Relative expression (R.E.) of representative proteostasis genes (top) and YAP1 target genes (bottom) in response to Tu in the presence of SON OE/KD (n=4 for SON KD and n=3 for SON OE). (**b**) Scatter plot showing relative fold change by *Son* KD versus SON OE for both Tu-induced and Tu-repressed genes. (**c**) Top predicted transcription regulators of 461 and 901 genes by the LISA Cistrome DB TR ChIP-Seq models. (**d, e**) Selected genes aligned for SC35 and XBP1s ChIP-seq signal from CT12 in XBP1^{Flox} mice [6] (**d**) and ChIP-qPCR of XBP1s and SC35 on selected regions (indicated by red bars) (n=2) (**e**). Data: Mean ± SEM.

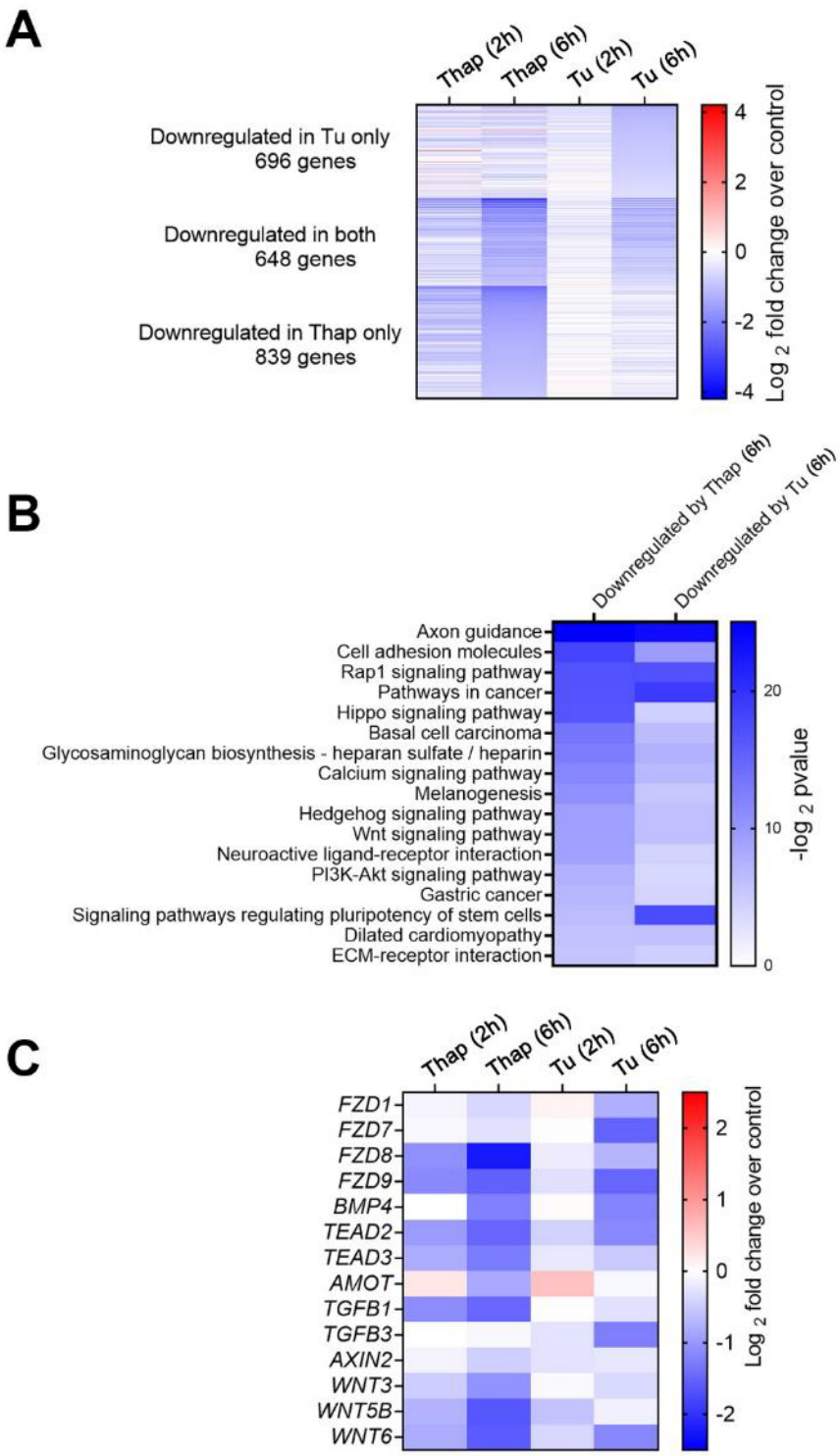

Extended Data Figure 3. YAP1 transcriptional output is repressed during ER stress in LN-308 cell. (**a**) Heatmap showing transcriptome that are significantly downregulated (log $_2$-fold change smaller than -0.5) with a p value less than 0.05) either under Tu or Thap treatment at 6h. (**b**) GO analysis of genes that are significantly downregulated either under Tu or Thap treatment at 6h. (**c**) Heatmap of representative YAP1 target genes as in **a**.

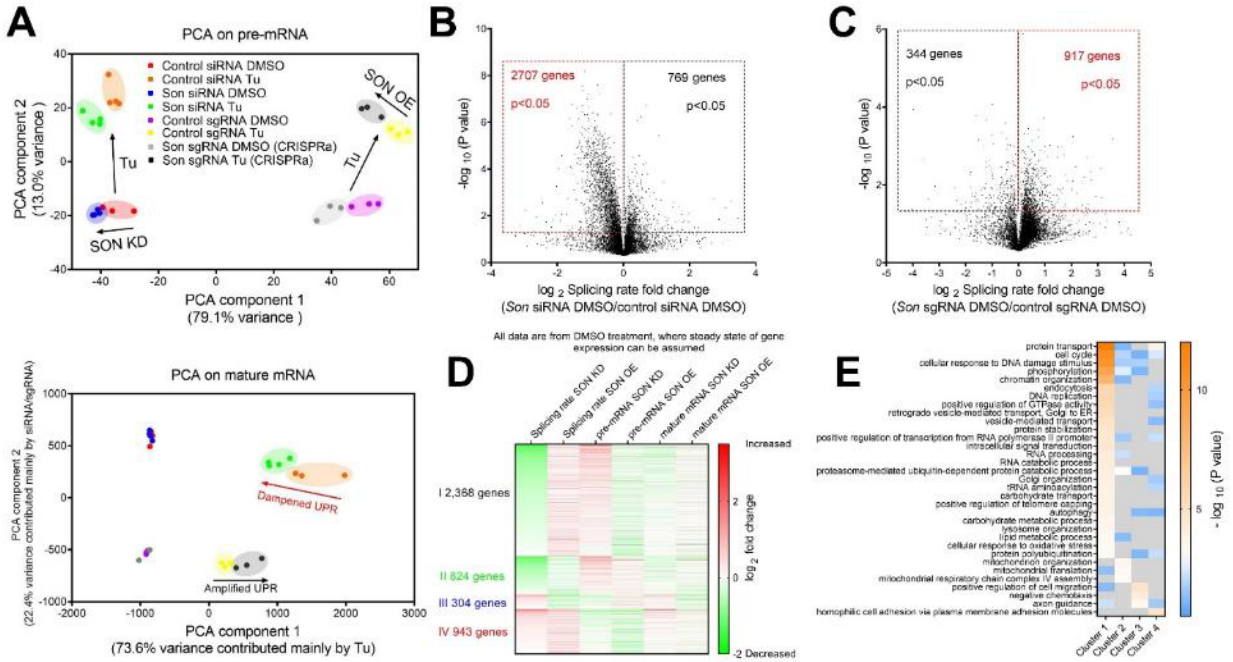

Extended Data Figure 4. SON regulates mRNA splicing rates under both basal and ER stress conditions (**a**) PCA analysis of global transcriptional response to Tu in the presence of SON OE/KD. Both pre-mRNA (top) and mature mRNA (bottom) are shown. (**b, c**) Volcano plot of mRNA splicing rates changes in SON KD (**b**) or OE (**c**) MEFs under basal condition (DMSO). (**d**) Heat map of fold change of RNA splicing rate, pre and mature mRNA level in SON OE/KD MEFs compared to control MEFs under vehicle (DMSO) condition. Four clusters of genes are shown. (**e**) GO analysis of genes in four clusters showing enriched KEGG pathways.

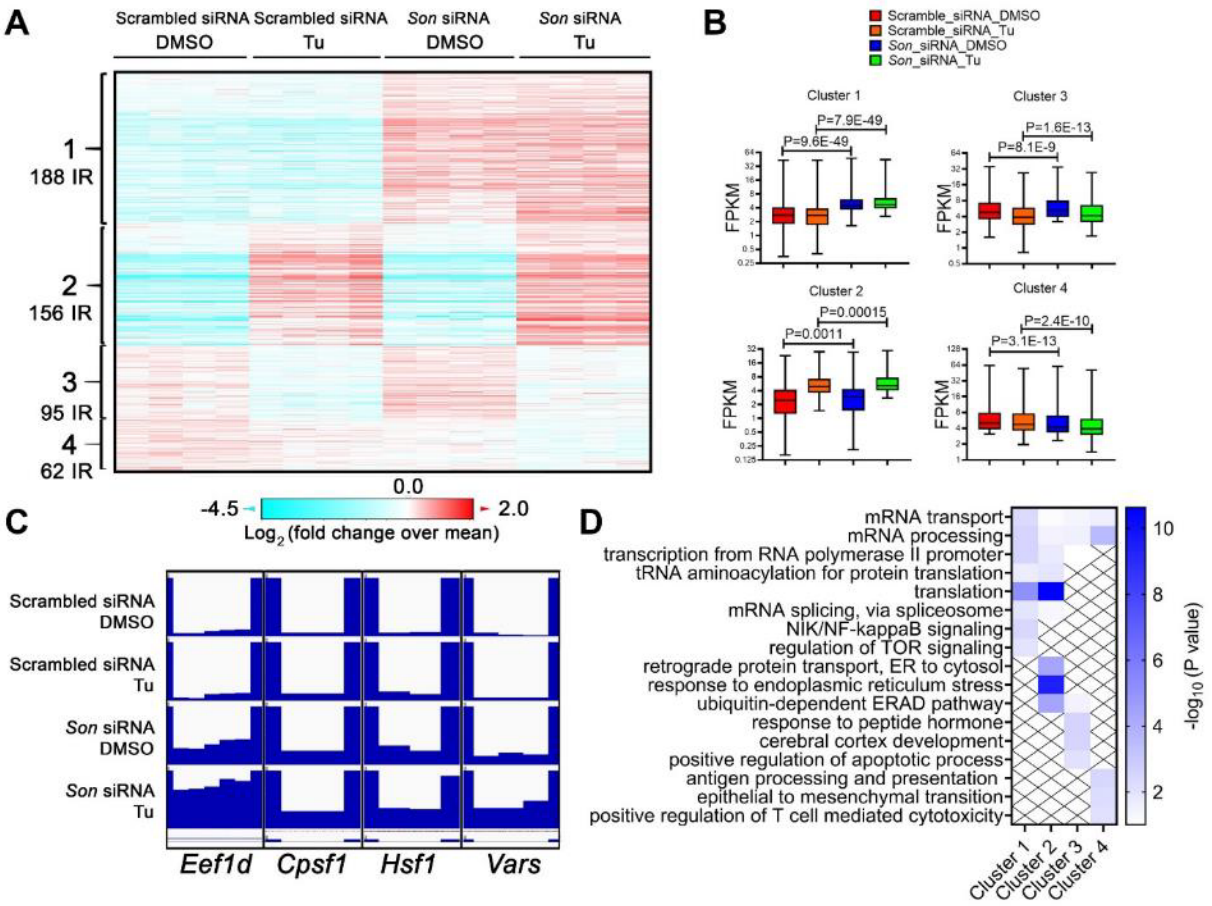

Extended Data Figure 5. SON knocking-down increases intron retention of proteostasis and mRNA metabolism genes. Heat map (**a**) and quantification (**b**) of intron retention events in MEFs with control or SON KD under basal (DMSO) and Tu conditions. Four clusters are shown. (**c**) The Integrative Genome Viewer representation of intron retention in selected genes. (**d**) GO analysis of genes in four clusters showing enriched KEGG pathways.

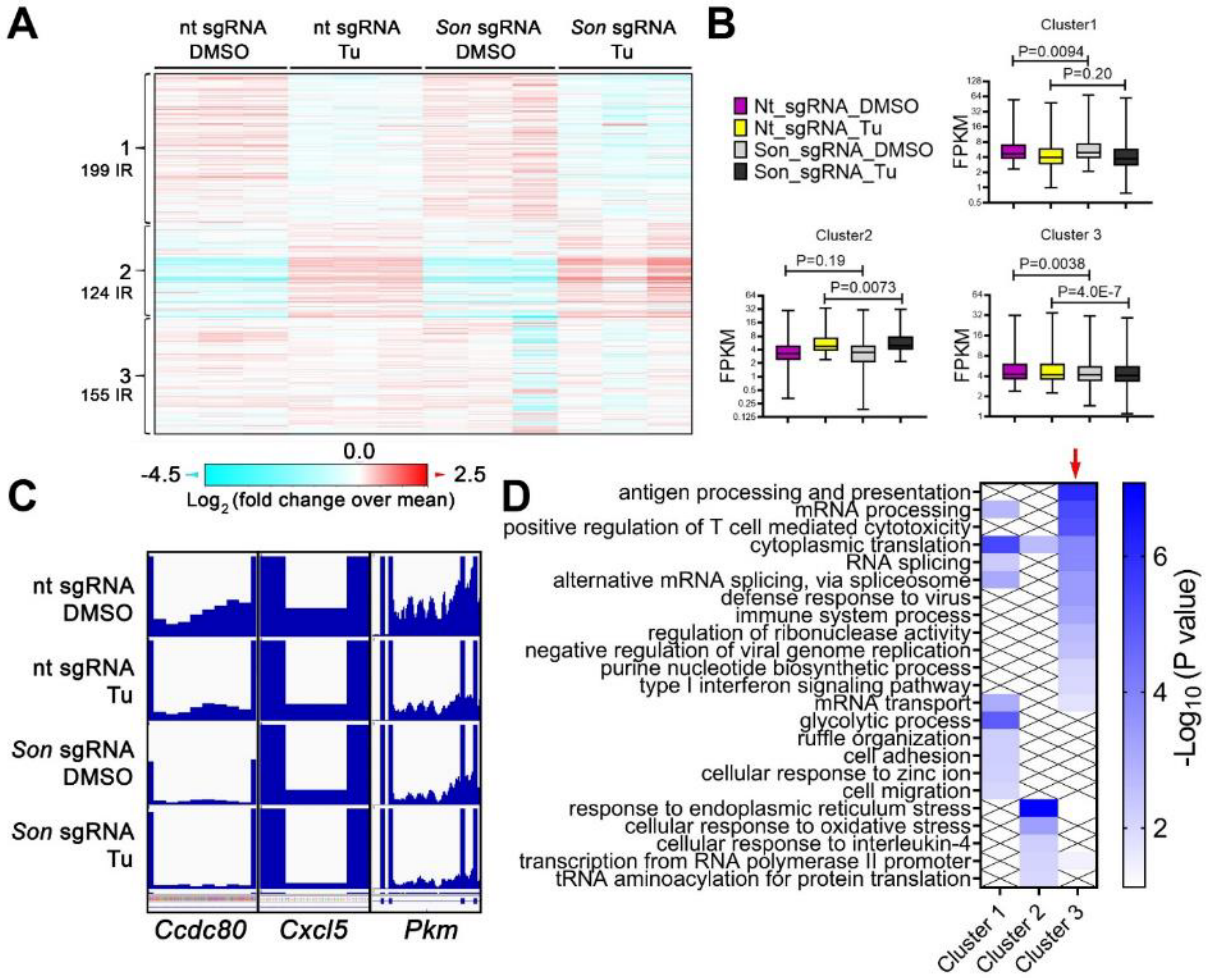

Extended Data Figure 6. SON overexpression decreases intron retention of protein processing and mRNA metabolism genes. Heat map (**a**) and quantification (**b**) of intron retention events in MEFs with control or SON overexpression under basal (DMSO) and Tu conditions. Three clusters are shown. (**c**) The Integrative Genome Viewer representation of intron retention in selected genes. (**d**) GO analysis of genes in three clusters showing enriched KEGG pathways.

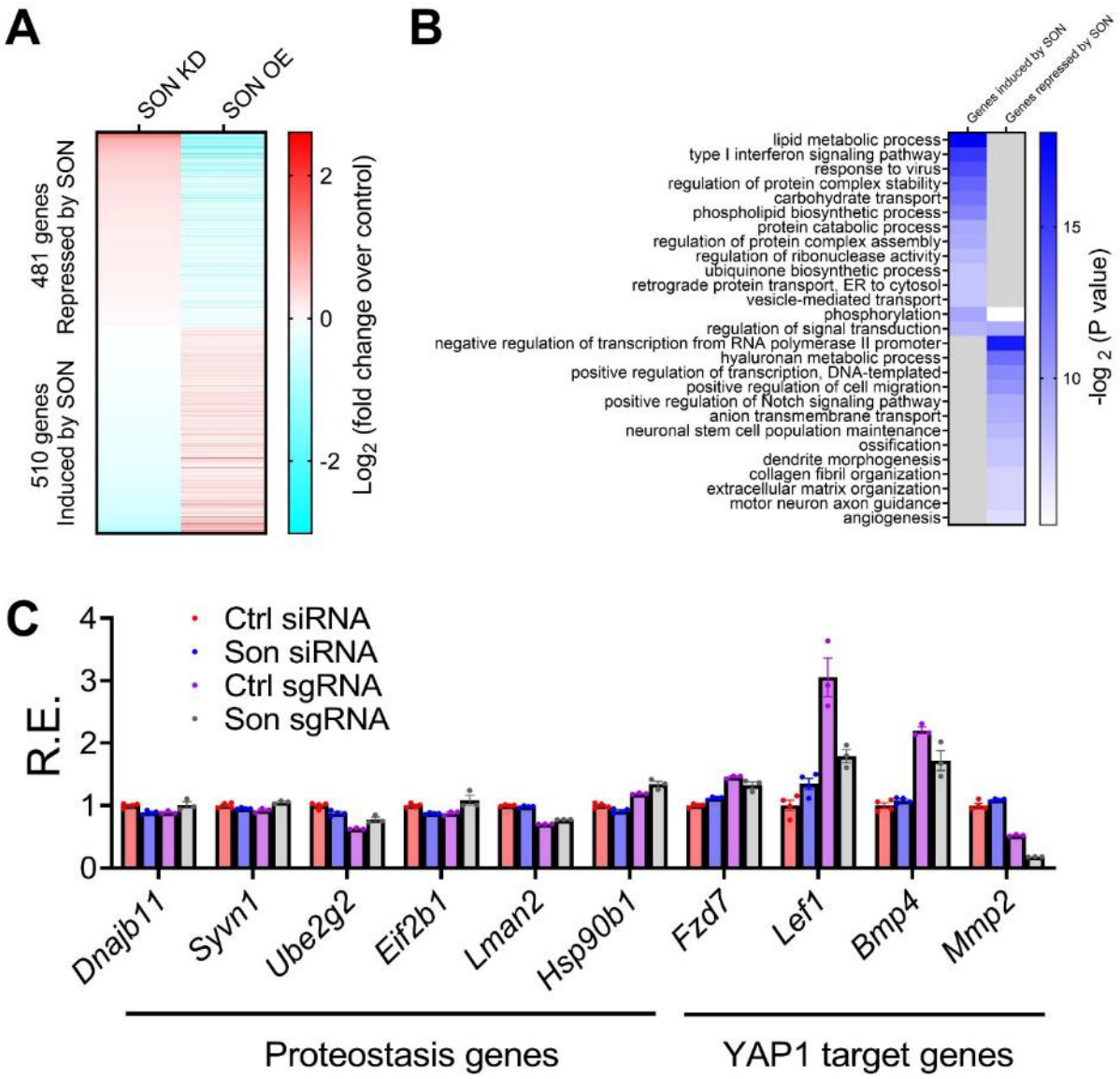

1637

1638 **Extended Data Figure 7. SON reprograms opposing proteostasis and YAP1 transcriptional**
1639 **output under basal condition.** (**a**) Heat map of fold change of mature mRNA level in *Son* OE/KD
1640 MEFs compared to control MEFs under vehicle (DMSO) condition. All mature mRNAs in this
1641 heatmap are statistically differentially expressed (P<0.05) in both SON OE/KD conditions,
1642 compared to their respective controls. (**b**) GO analysis of these 481 and 501 genes. (**c**)
1643 Representative mature mRNA expression of proteostasis and YAP1 target genes (n=4 for Ctrl
1644 and *Son* siRNA and n=3 for Ctrl and *Son* sgRNA).

1645

1646

1647

1648

A

KEGG Term	PValue
Protein processing in endoplasmic reticulum	8.11E-19
Spliceosome	2.26E-17
mRNA surveillance pathway	2.20E-08
Ribosome biogenesis in eukaryotes	3.27E-07
Protein export	4.34E-06
Nucleocytoplasmic transport	1.20E-05
Apoptosis	1.35E-05
Epstein-Barr virus infection	1.85E-05
Endocytosis	1.98E-05
Ubiquitin mediated proteolysis	2.84E-05
Hippo signaling pathway	4.49E-05

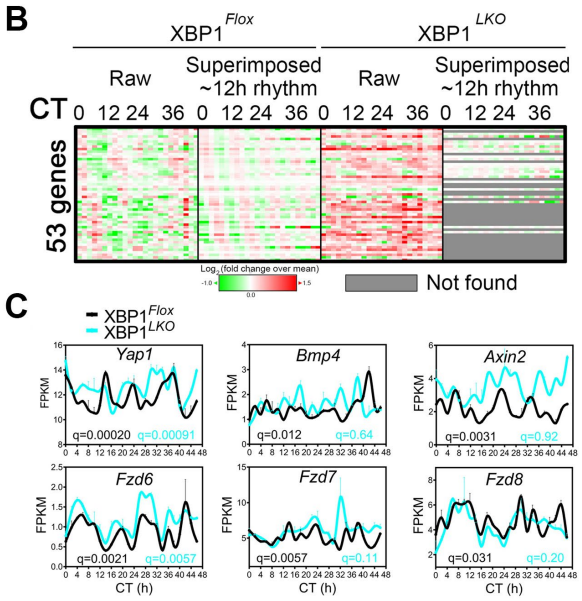

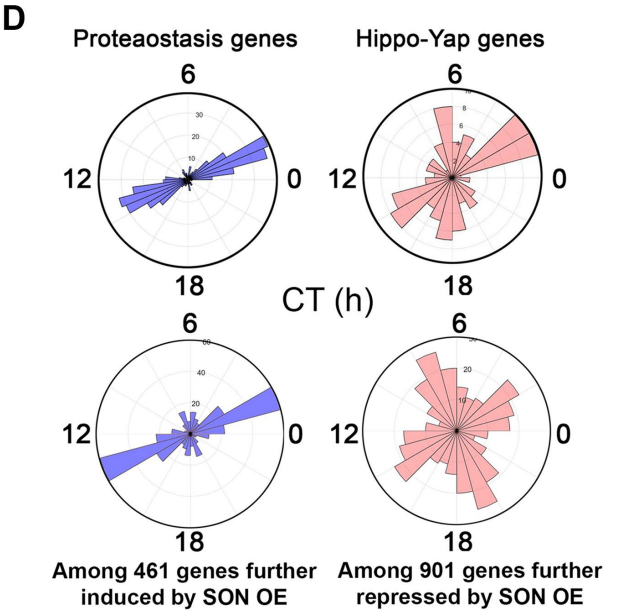

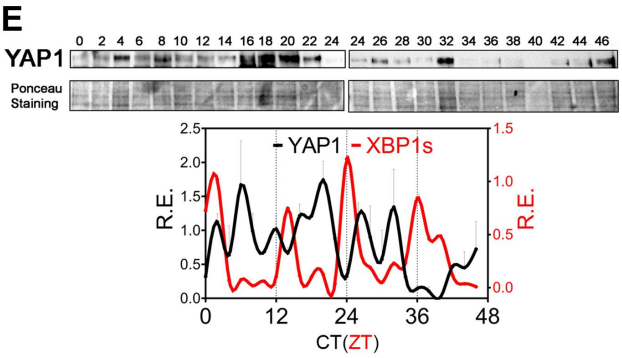

Extended Data Figure 8. ~12h ultradian rhythms of anti-phasic protein quality control and YAP1 output gene expression are prevalent in vivo. (**a**) KEGG pathway analysis of 12h transcriptome in mouse liver reported in [6]. (**b**) Heat map of 53 Hippo-YAP1 related gene expression and superimposed 12h rhythm (or lack thereof) in wild-type XBP1^{Flox} and XBP1^{LKO} mouse liver. Gray indicates the lack of a superimposed 12h rhythm. (**c**) RPKM values of representative genes involved in Hippo-YAP1 signaling in XBP1^{Flox} and XBP1^{LKO} mouse liver. q values of significantly exhibiting a 12h rhythm by RAIN analysis is also shown for each gene in XBP1^{Flox} (black) and XBP1^{LKO} (cyan) mice (n=2 per time point). (**d**) Polar histogram demonstrating the phase distributions of ~12h cycling proteostasis genes and Hippo-YAP1 signaling genes (top). Polar histogram demonstrating the phase distributions of ~12h genes further amplified by SON OE and genes further repressed by SON OE (bottom). (**e**) Western blot and quantification of nuclear level of YAP1 rhythm in mouse liver (n=2 at each time point), overlaid with that of XBP1s reported in [9]. All data mean ± S.E.M.

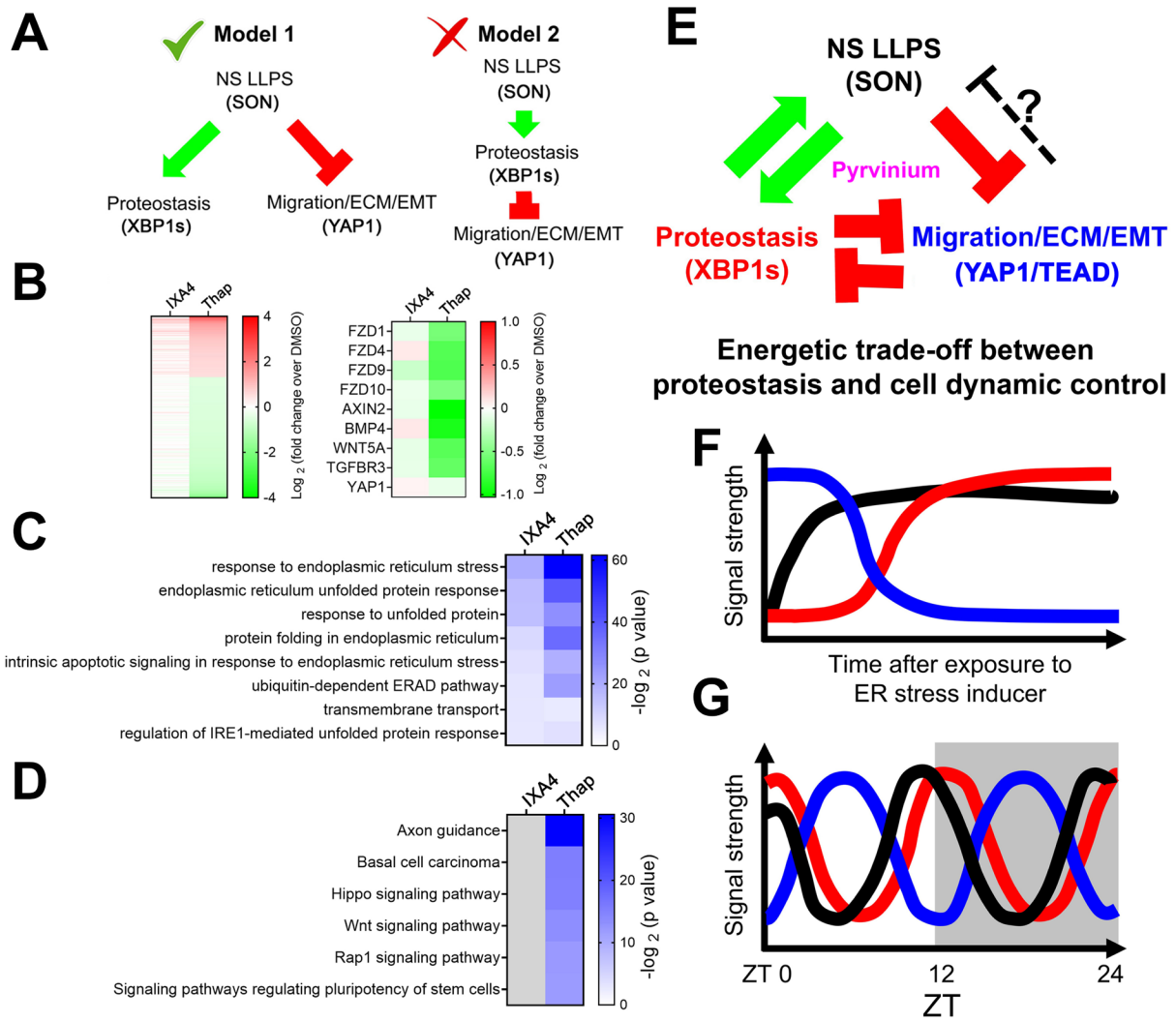

Extended Data Figure 9. NS LLPS dictates opposing proteostasis and YAP1 signaling. (**a**) Two models explaining the relationship among nuclear speckles LLPS dynamics, proteostasis and YAP1 transcriptional output. Our results support model 1. (**b**) Heatmap demonstrating relative fold change of gene expression relative to DMSO control in IXA4 or Thap treated HEK293T cells. All genes induced or repressed by at least 1.41-fold with p value smaller than 0.05 in Thap condition (left), and representative YAP1-related genes (right). (**c, d**) GO analysis of all upregulated (**c**) or downregulated (**d**) genes in either IXA4 or Thap treatment by at least 1.41-fold with a p-value smaller than 0.05. (**e**) An expanded model of how NS' LLPS can dictate proteostasis and YAP1 transcriptional output. Please see main text for details. (**f, g**) Diagram showing temporal changes of NS' LLPS (black), proteostasis (red) and YAP1 transcriptional output (blue) signal during ER stress (**f**) or in a given day (**g**) under physiological condition.

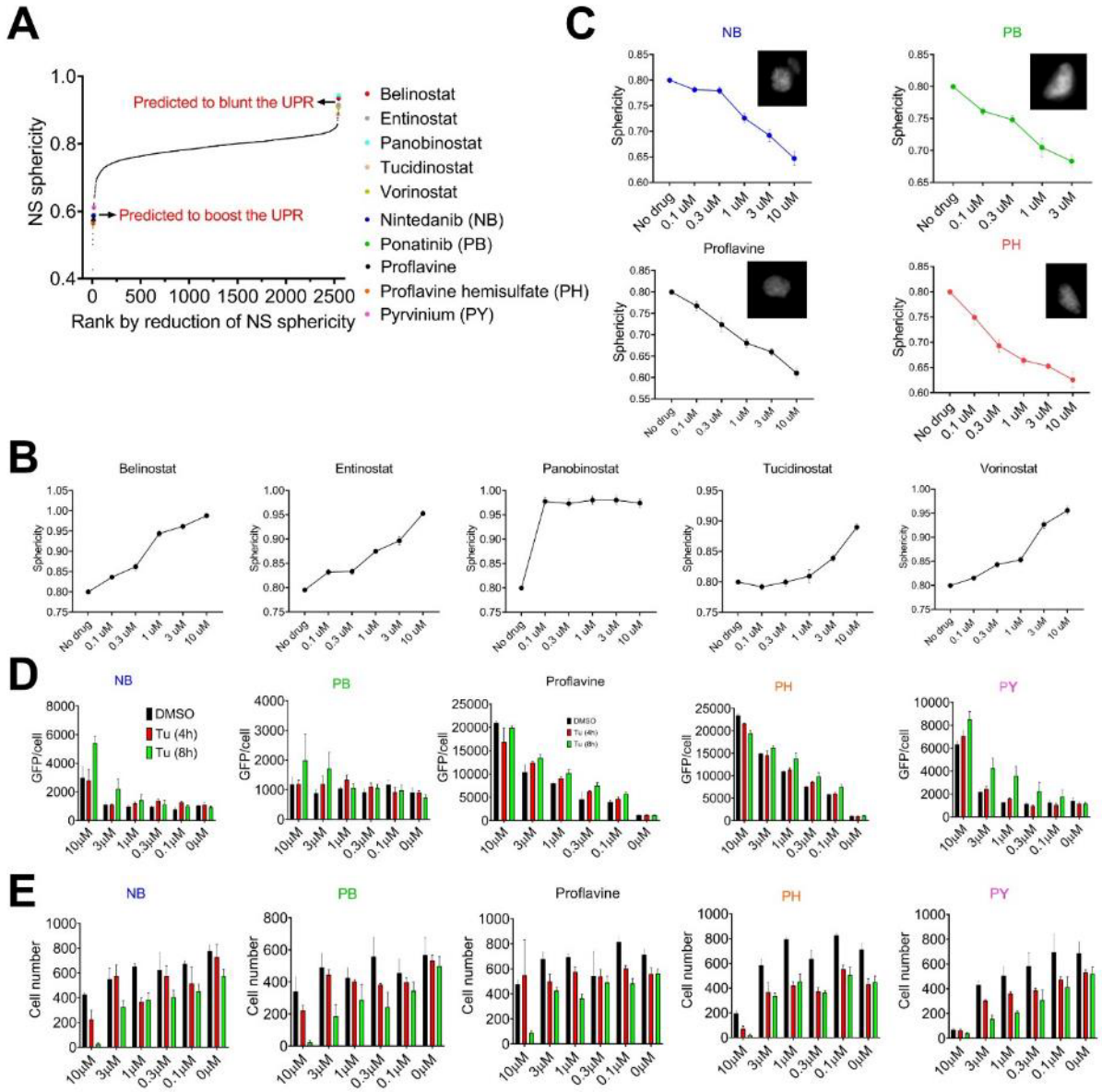

Extended Data Figure 10. HTS identifies compounds that alter nuclear speckle morphology and the UPR. (**a**) Compounds in the FDA-approved library ranked from lowest to highest on their ability to reduce NS sphericity. (**b**) Four drugs are shown to have a dose-dependent effect on NS morphology (n=16). (**c**) Dose-dependent effects of drugs on increasing NS sphericity (n=16). (**d, e**) GFP/cell (**d**) or cell number (**e**) measured in *Perk* promoter-driven dGFP reporter MEFs in the presence of Tu for four or eight hours after pre-treatment of different concentrations of drugs or DMSO for 24 hours (n=4).

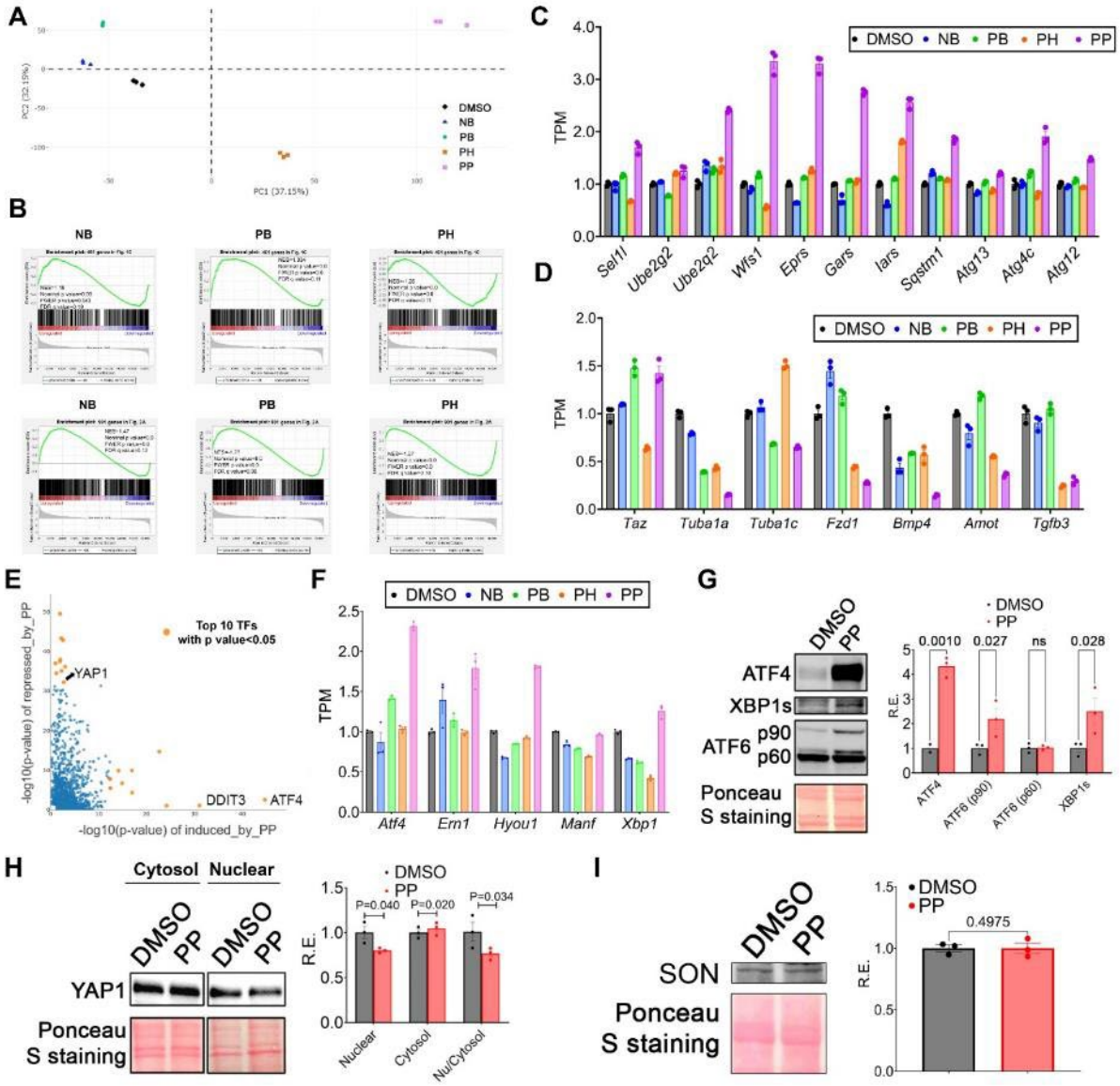

Extended Data Figure 11. PP is a bona fide nuclear speckle rejuvenator. (**a**) MEFs were treated with 3 μM NB, 1 μM PB, 3 μM PH, and 1 μM PP for 24 hours and RNA-seq was performed. PCA analysis of global transcriptional response to drug treatments. (**b**) For each of the GSEA analysis, genes further activated by SON OE or further repressed by SON OE are compared to the transcriptome signatures of MEFs under different drug treatments. (**c, d**) Gene expression of select protein quality control (**c**) and YAP1 target genes (**d**) genes determined through mRNA-Seq (n=3). (**e**) LISA analysis listing log transformed p values for top predicted transcription regulators for genes upregulated (x-axis) and downregulated (y-axis) by PP. (**f**) Gene expression of select UPR genes determined through mRNA-Seq under different drugs treatment (n=3). (**g-i**) Western blot and quantification of UPR TFs (**g**), YAP1 nuclear and cytosol (**h**) and SON (**i**) level in response to 1 μM PP for 24 hours (n=3).

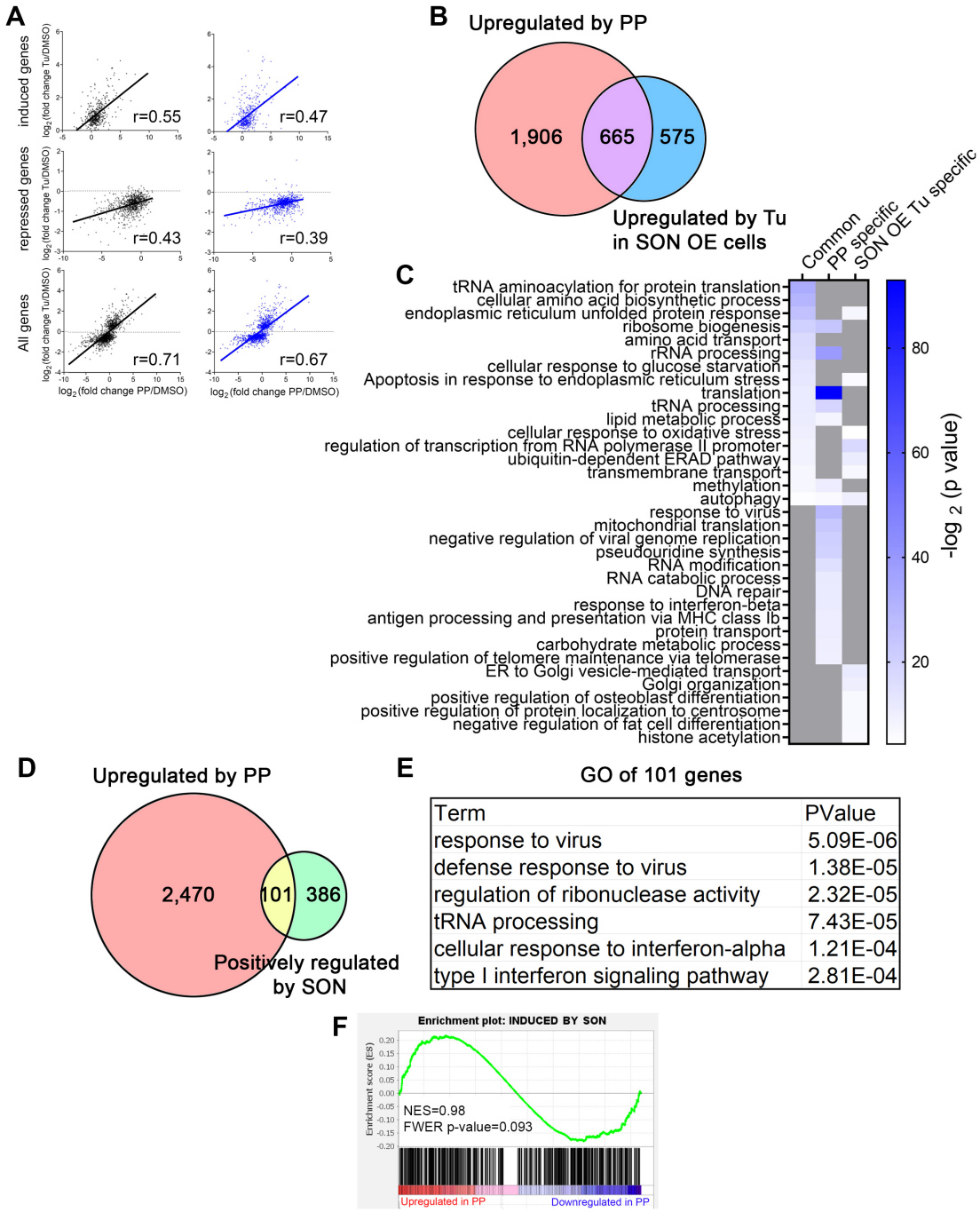

Extended Data Figure 12. Comparison of upregulated genes by PP and SON OE. (**a**) Scatter plot comparing the fold change of gene expression by PP (x-axis) and by Tu (y-axis) under SON OE or SON KD condition. Correlation coefficient and p value are shown for each plot. Chow test indicates statistically significant coefficients between the two linear regressions with p=0.00195. (**b, c**) Venn diagram showing (**b**) and GO analysis of (**c**) specific and commonly upregulated genes by PP and Tu in SON OE MEFs. (**d**) Venn diagram showing specific and common upregulated genes by PP and SON in MEFs. (**e**) GO analysis of common 101 genes. (**f**) GSEA analysis comparing genes upregulated by SON with those regulated by PP.

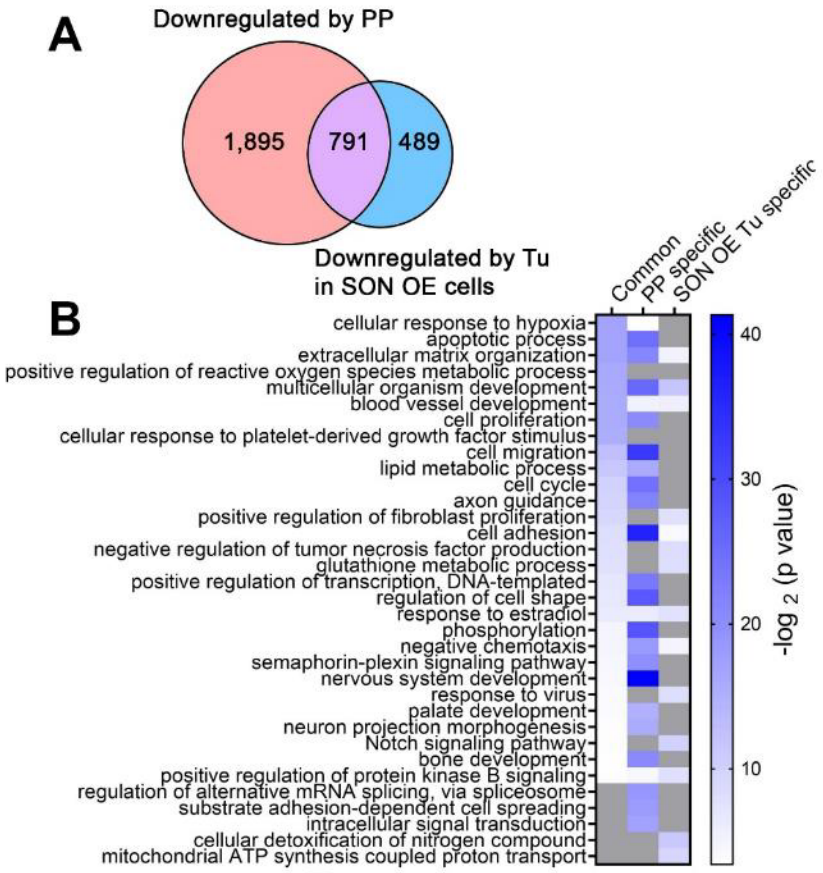

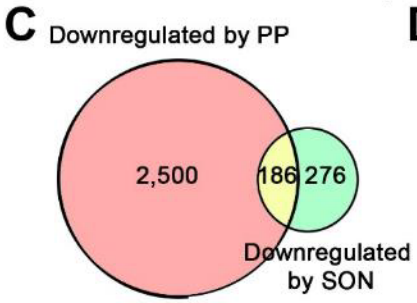

D

GO of 186 genes

Term	PValue
positive regulation of cell migration	1.07E-04
positive regulation of Notch signaling pathway	3.71E-04
ossification	4.45E-04
ureteric bud development	8.10E-04
bone development	0.001
neural crest cell migration	0.00101
extracellular matrix organization	0.00108
axon guidance	0.00127

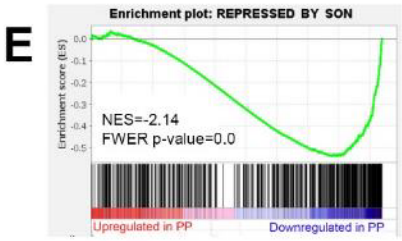

Extended Data Figure 13. Comparison of downregulated genes by PP and SON OE. (**a-b**) Venn diagram showing (**a**) and GO analysis of (**b**) specific and common downregulated genes by PP and Tu in SON OE MEFs. (**c**) Venn diagram showing specific and common downregulated genes by PP and SON in MEFs. (**d**) GO analysis of common 186 genes. (**e**) GSEA analysis comparing genes downregulated by SON with those regulated by PP.

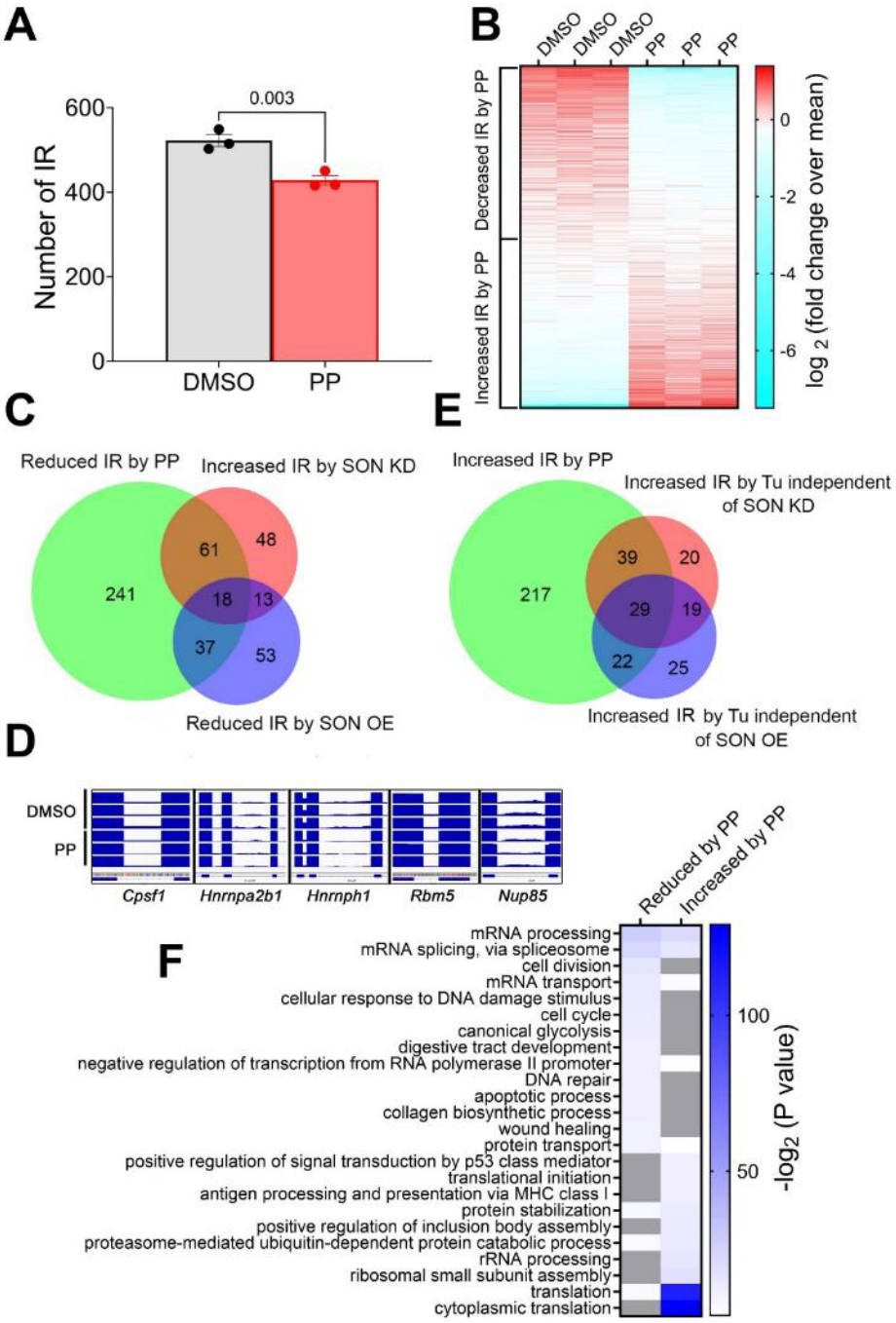

Extended Data Figure 14. Comparison of intron retention (IR) events among PP, SON OE and SON KD. (**a**) Quantification of IR under DMSO and PP condition (n=3). (**b**) Heatmap showing RPKM normalized level of retained introns in DMSO and PP condition. (**c, d**) Venn diagram comparing genes with specific or common IRs between different conditions. (**e**) Genome browser view of selective genes with reduced IR by PP. (**f**) GO analysis of genes with increased or reduced IR by PP.

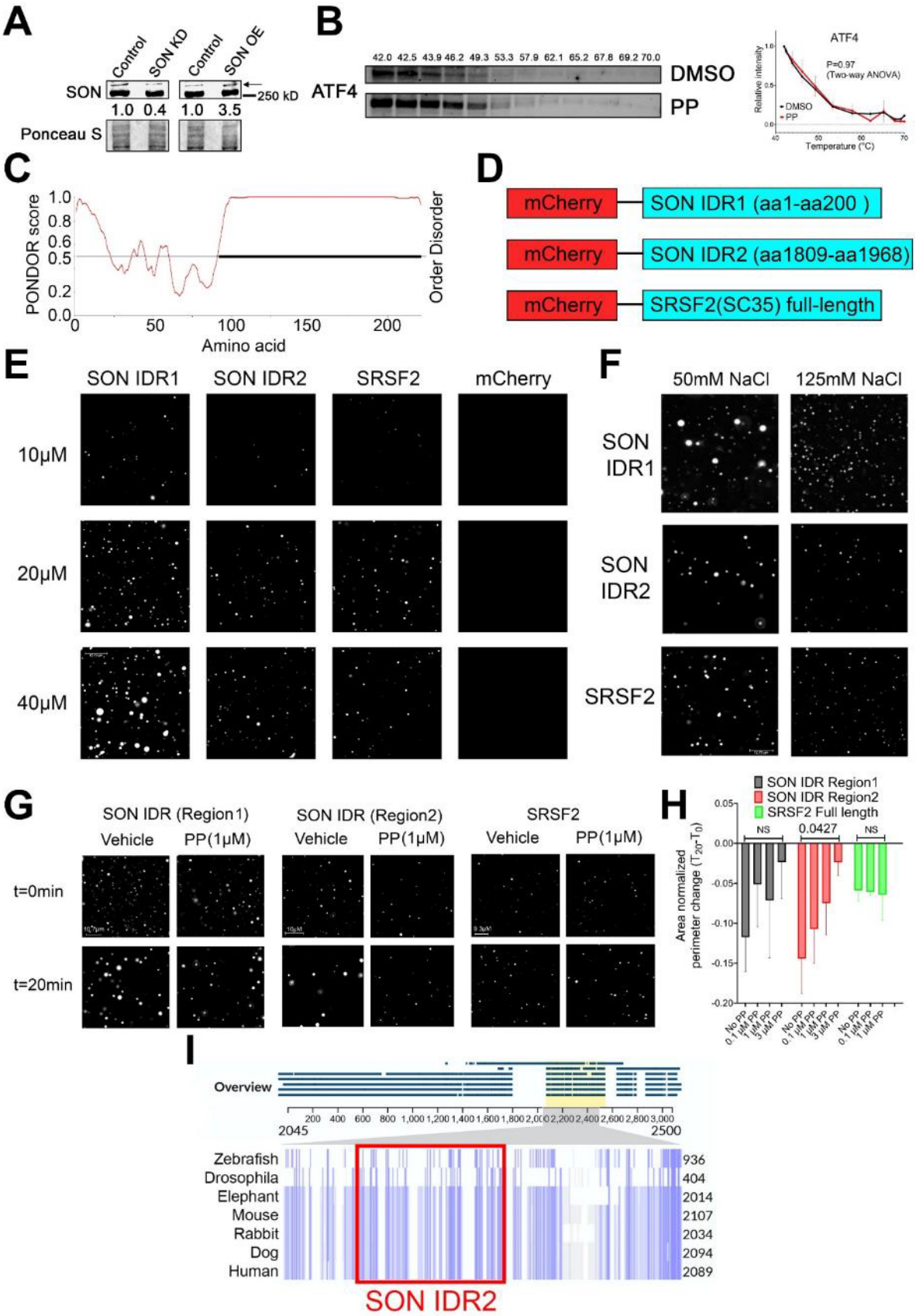
A
Control
SON kD
Control
SON OE
SON
250 kD
1.0 0.4 1.0 3.5
Ponceau S
B
42.0 42.5 43.9 46.2 49.3 53.3 57.9 62.1 65.2 67.8 69.2 70.0
ATF4
DMSO
PP
ATF4
P=0.97
(Two-way ANOVA)
Relative intensity
DMSO
PP
Temperature (°C)
C
PONDOR score
Order Disorder
Amino acid
D
mCherry
SON IDR1 (aa1-aa200)
mCherry
SON IDR2 (aa1809-aa1968)
mCherry
SRSF2(SC35) full-length
E
SON IDR1
SON IDR2
SRSF2
mCherry
10μM
20μM
40μM
F
50mM NaCl
125mM NaCl
SON IDR1
SON IDR2
SRSF2
G
SON IDR (Region1)
SON IDR (Region2)
SRSF2
Vehicle
PP(1μM)
t=0min
t=20min
H
SON IDR Region1
SON IDR Region2
SRSF2 Full length
NS
0.0427
NS
Area normalized perimeter change (T_{20}-T_0)
No PP
0.1 μM PP
1 μM PP
3 μM PP
I
Overview
2045
2500
Zebrafish 936
Drosophila 404
Elephant 2014
Mouse 2107
Rabbit 2034
Dog 2094
Human 2089
SON IDR2

1729

1730 **Extended Data Figure 15. PP directly targets SON to modulate nuclear speckle LLPS**
1731 **dynamics.** (**a**) Western blots of SON with siRNA-mediated knockdown and SON OE. (**b**) CETSA
1732 of ATF4 with 3μM PP. Both representative blot and quantification from independent replicates are
1733 shown (n=2 for DMSO and n=3 for PP). (**c**) Computational prediction of IDR in mouse SRSF2
1734 (SC35) protein. (**d**) Diagram illustrating the constructs for droplet formation assay (**e**)
1735 Representative images of droplet formation assay with different concentrations of recombinant
1736 protein at 125mM NaCl. (**f**) Representative images of droplet formation assay with different salt
1737 concentrations with 20μM recombinant proteins. (**g, h**) Representative images of droplet
1738 formation assay with different recombinant proteins (**g**) and quantification (**h**) of area-normalized
1739 perimeter changes in the time span of 20 minutes with 50mM NaCl (n=3). (**i**) Alignment of protein
1740 sequences of SON orthologs in seven different species. SON IDR2 is located within the most
1741 conserved region (highlighted by light yellow).

1742

1743

1744

1745

1746

1747

1748

1749

1750

1751

1752

1753

1754

1755

1756

1757

1758

1759

1760

1761

1762

1763

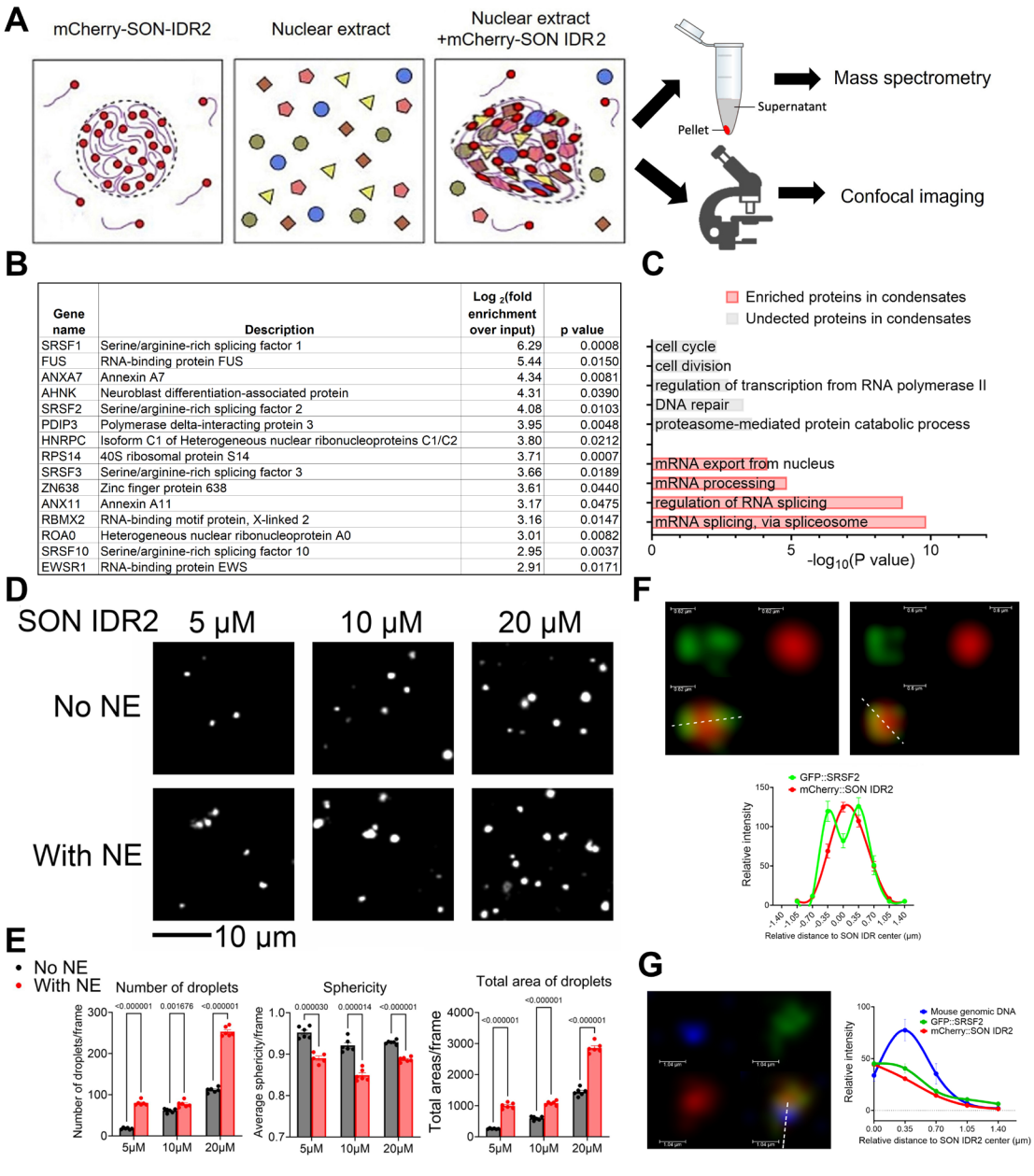

Gene name	Description	Log $_2$(fold enrichment over input)	p value
SRSF1	Serine/arginine-rich splicing factor 1	6.29	0.0008
FUS	RNA-binding protein FUS	5.44	0.0150
ANXA7	Annexin A7	4.34	0.0081
AHNK	Neuroblast differentiation-associated protein	4.31	0.0390
SRSF2	Serine/arginine-rich splicing factor 2	4.08	0.0103
PDIP3	Polymerase delta-interacting protein 3	3.95	0.0048
HNRPC	Isoform C1 of Heterogeneous nuclear ribonucleoproteins C1/C2	3.80	0.0212
RPS14	40S ribosomal protein S14	3.71	0.0007
SRSF3	Serine/arginine-rich splicing factor 3	3.66	0.0189
ZN638	Zinc finger protein 638	3.61	0.0440
ANX11	Annexin A11	3.17	0.0475
RBMX2	RNA-binding motif protein, X-linked 2	3.16	0.0147
ROA0	Heterogeneous nuclear ribonucleoprotein A0	3.01	0.0082
SRSF10	Serine/arginine-rich splicing factor 10	2.95	0.0037
EWSR1	RNA-binding protein EWS	2.91	0.0171

Extended Data Figure 16. PP modulates nuclear speckle LLPS dynamics in a cell-free system. (**a**) Diagram showing NE-supplemented SON IDR2 condensates are expected to compartmentalize splicing factors and exhibit less spherical morphology. (**b**) NE-supplemented SON IDR2 condensates are spun down and subject to mass spectrometry. Top 15 proteins enriched in SON IDR2-compartmentzlied condensates with p value<0.05. (**c**) GO of top enriched biological pathways of proteins depleted or enriched in SON IDR2-compartmentzlied condensates. (**d, e**) Representative images of droplet formation assay with increasing concentration of SON IDR2 with or without NE supplementation (**e**) and quantification (**e**) of the number, sphericity and total areas of droplets (n=6). (**f**) Representative images and quantification of spatial distribution of mCherry::SON IDR2 and GFP::SRSF2. (**g**) Representative images and quantification of spatial distribution of mCherry::SON IDR2, GFP::SRSF2 and mouse genomic DNA.

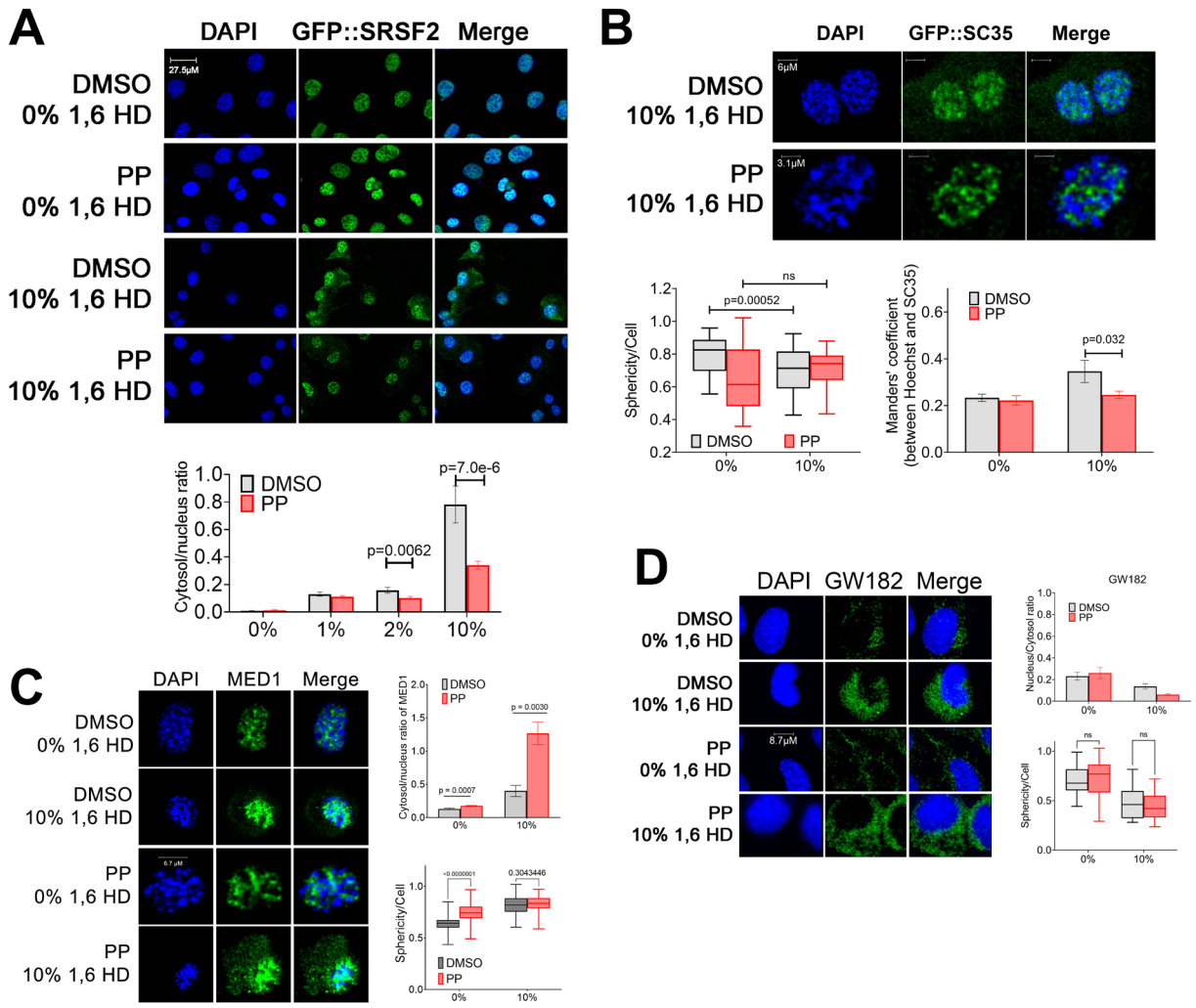

Extended Data Figure 17. PP alters the sensitivity of different condensates to 1,6 hexanediol. (**a**) 1,6 hexanediol sensitivity assay with representative images and quantification (n=20~95) of the ratio of cytosol over nuclear intensity of GFP::SRSF2 signal. (**b**) 1,6 hexanediol sensitivity assay with representative images and quantification of sphericity (n=24~50) of GFP::SRSF2 signal and Manders' coefficient (n=10~14) of signals of GFP and Hoechst. (**c**) 1,6 hexanediol sensitivity assay with representative images and quantification of ratio of cytosol to nuclear MED1 signal (n=19~29) and sphericity of MED1 signal (n=31~75). (**d**) 1,6 hexanediol sensitivity assay with representative images and quantification of ratio of cytosol to nuclear GW182 signal (n=16~54) and sphericity (n=19~97) of GW182 signal.

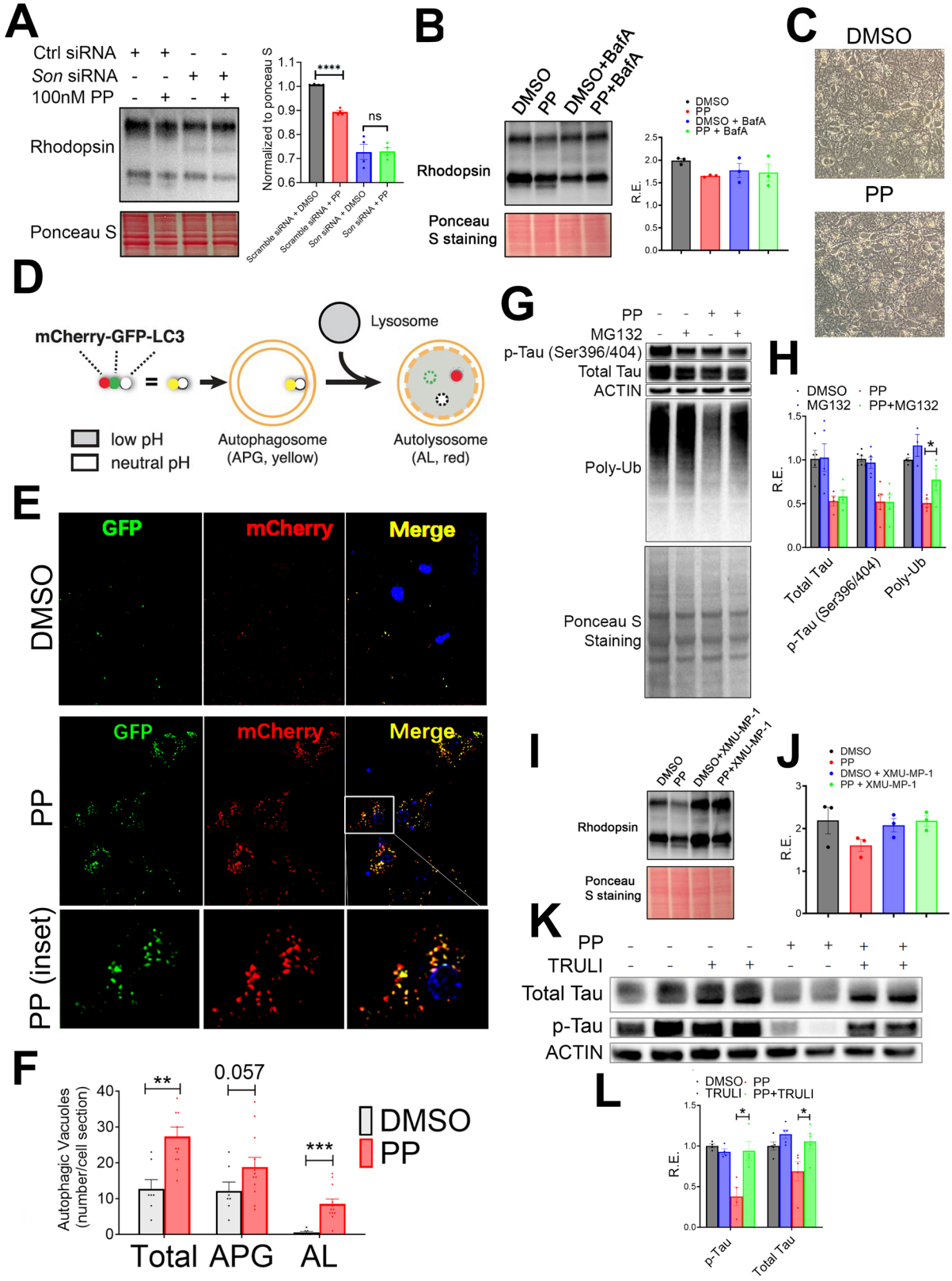
A
Ctrl siRNA + + - -
Son siRNA - - + +
100nM PP - + - +
Rhodopsin
Ponceau S
Normalized to ponceau S
****
ns
Scramble siRNA + DMSO
Scramble siRNA + PP
Son siRNA + DMSO
Son siRNA + PP
B
DMSO
PP
DMSO+BafA
PP+BafA
Rhodopsin
Ponceau S staining
DMSO
PP
DMSO + BafA
PP + BafA
R.E.
C
DMSO
PP
D
mCherry-GFP-LC3
Lysosome
low pH
neutral pH
Autophagosome (APG, yellow)
Autolysosome (AL, red)
E
GFP
mCherry
Merge
DMSO
PP
PP (inset)
F
Autophagic Vacuoles (number/cell section)
**
0.057
***
DMSO
PP
Total
APG
AL
G
PP
MG132
p-Tau (Ser396/404)
Total Tau
ACTIN
Poly-Ub
Ponceau S Staining
H
DMSO
PP
MG132
PP+MG132
R.E.
*
Total Tau
p-Tau (Ser396/404)
Poly-Ub
I
DMSO
PP
DMSO+XMU-MP-1
PP+XMU-MP-1
Rhodopsin
Ponceau S staining
J
DMSO
PP
DMSO + XMU-MP-1
PP + XMU-MP-1
R.E.
K
PP
TRULI
Total Tau
p-Tau
ACTIN
L
DMSO
PP
TRULI
PP+TRULI
R.E.
*
*
p-Tau
Total Tau

1792

1793 **Extended Data Figure 18. Pyrvinium pamoate reduces pathological Tau and Rhodopsin**
1794 **level by boosting autophagy and UPS activity.** (**a**) NIH3T3 RHO^{P23H} cells were transfected with
1795 scrambled or *Son* siRNA for 24 hours before treated with DMSO or 0.1μM PP for another 24
1796 hours. Western blot and quantification of RHO^{P23H} level (n=4) (**b**) NIH3T3 RHO^{P23H} cells were
1797 treated with 0.1μM PP and co-treated with or without BafA (100nM) for 24 hours. Western blot
1798 and quantification of RHO^{P23H} level (n=3). (**c**) Representative images of primary mouse neurons
1799 treated with DMSO or 0.5 μM PP for 24 hours. (**d-f**) Autophagic flux was measured via a
1800 mCherry::GFP::LC3 fusion protein reporter in mouse primary neurons. One key protein used to
1801 study autophagic flux is LC3B (microtubule-associated protein 1 light chain 3). This protein is
1802 recruited from the cytosol, maturated and bound to the isolation membrane. This localization
1803 serves as a marker for autophagic membranes. Chimeric proteins consisting of LC3B fused to
1804 both GFP and mCherry provide a way of monitoring the autophagic flux. Autophagosomes
1805 labelled by an mCherry::GFP::LC3 show both mCherry and GFP signals. After fusion with
1806 lysosomes, GFP signals are significantly reduced due to acidic conditions, while mCherry signals
1807 remain relatively stable (**d**). Thus, an increase in the number of mCherry positive puncta
1808 (autolysosomes) indicates an increase of autophagic flux. Representative images showing an
1809 increase of the number of mCherry positive puncta in primary neurons cultured in the presence
1810 of 0.1μM PP for 12 hours, with zoomed in images of regions marked with white rectangles (**e**).
1811 Quantification of the number of total vacuoles, autophagosome and autolysosomes (n=7~12) (**f**).
1812 (**g, h**) Tau P301S-expressing primary neurons were co-treated with vehicle or 0.1μM PP in the
1813 presence or absence of MG132 (10μM) for 12 hours and western blot (**g**) and quantification (**h**)
1814 of different proteins (n=3~5). (**i, j**) NIH3T3 RHO^{P23H} cells were treated with 0.1μM PP for 24 hours
1815 and co-treated with or without XMU-MP1. Western blot (**i**) and quantification (**j**) of RHO^{P23H} level
1816 (n=3). (**k, l**) Tau P301S-expressing primary neurons were co-treated with vehicle or 0.1μM PP in
1817 the presence or absence of YAP1 activator TRULI (10μM) for 12 hours and western blot (**k**) and
1818 quantification (**l**) of different proteins (n=4~5). All data mean ± S.E.M.

1819

1820

1821

1822

1823

1824

1825

1826

1827

1828

1829

1830

1831

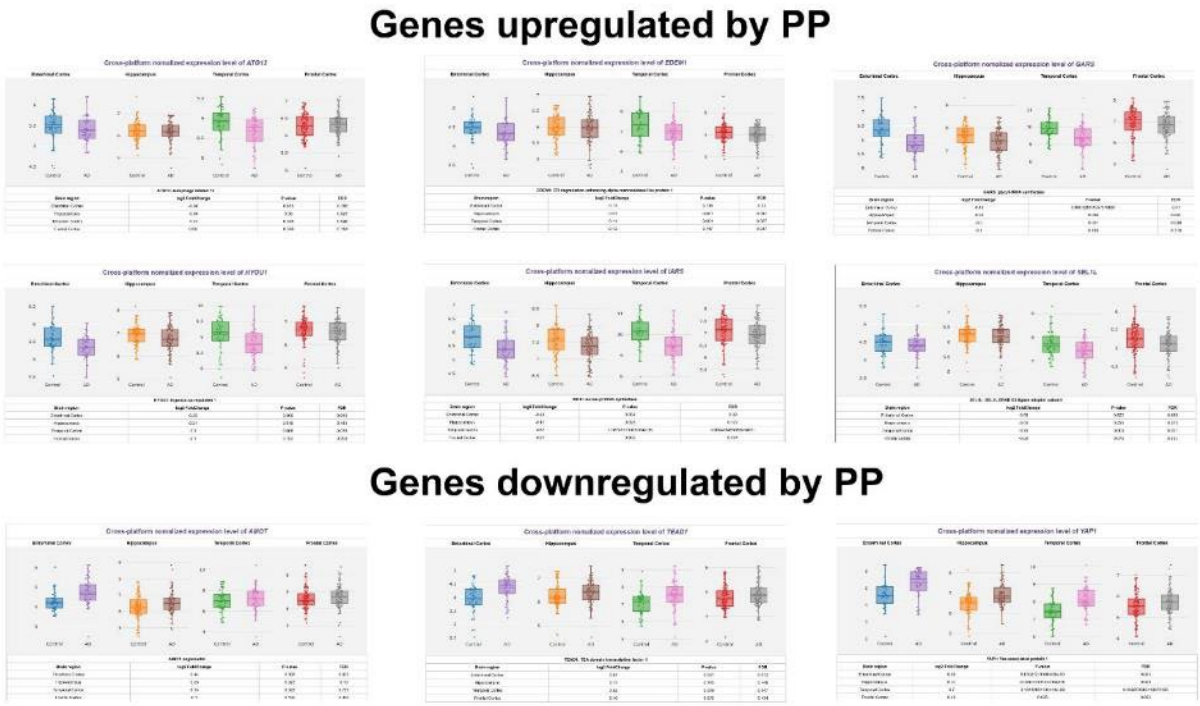

Extended Data Figure 19. Gene signatures in human AD subjects are opposite from those regulated by PP revealed by bulk RNA-Seq. Relative gene expressions in different brain regions of human AD subjects normalized to control subjects as reported in [84].

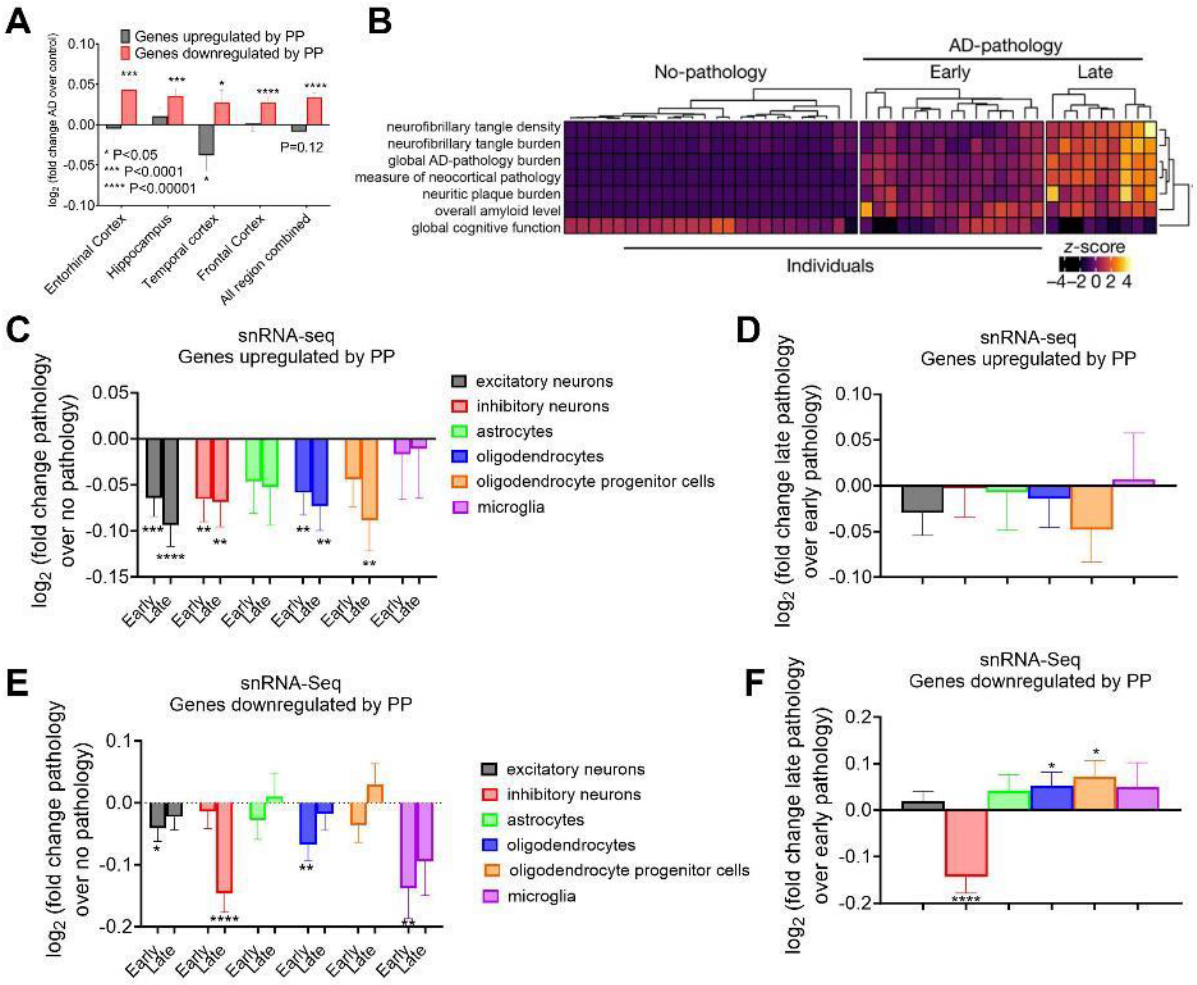

Extended Data Figure 20. Gene signatures in late-stage human AD subjects with severe tauopathy are opposite from those regulated by PP. (**a**) Log $_2$ transformed values of fold change of gene expression in different individual or combined brain regions of AD versus control human subjects for top genes that were either upregulated or downregulated by PP (with a $\log_2$ fold change > 1.5) in MEFs. (**b**) Phenotypic clustering of 48 individuals (columns) using seven clinicopathological variables as reported and adapted from [85]. (**c-f**) Log $_2$ transformed values of fold change of mean gene expression in different cell types of early or late AD versus no pathology human subjects for top genes that were either upregulated (**c**) or downregulated by PP in MEFs (**e**). Log 2 transformed values of fold change of mean gene expression in different cell types of late AD versus early AD human subjects for top genes that were either upregulated (**d**) or downregulated by PP in MEFs (**f**). p values calculated for one sample t-test (one-tailed). * p<0.05, ** p<0.01, *** p<0.001, **** p<0.0001.

1867 **Supplemental Movie legends:**

1868 **Movie S1.** Time lapse imaging of droplet formation with 20μm SON IDR1 in 125mM NaCl.

1869 **Movie S2.** Time lapse imaging of droplet formation with 20μm SON IDR2 in 125mM NaCl.

1870 **Movie S3.** Time lapse imaging of droplet formation with 20μm SRSF2 in 125mM NaCl.

1871 **Movie S4.** Time lapse imaging of droplet formation with 10μm SON IDR2 supplemented with
1872 0.6mg/ml GFP::SRSF2 MEF NE.

1873 **Supplemental Table legends:**

1874 **Table S1.** FPKM normalization of RNA-seq of SON OE and KD cells in the absence or presence
1875 of Tunicamycin in MEFs.

1876 **Table S2.** TPM normalization of RNA-seq of different chemical treatments in MEFs.

1877

1878

1879

1880